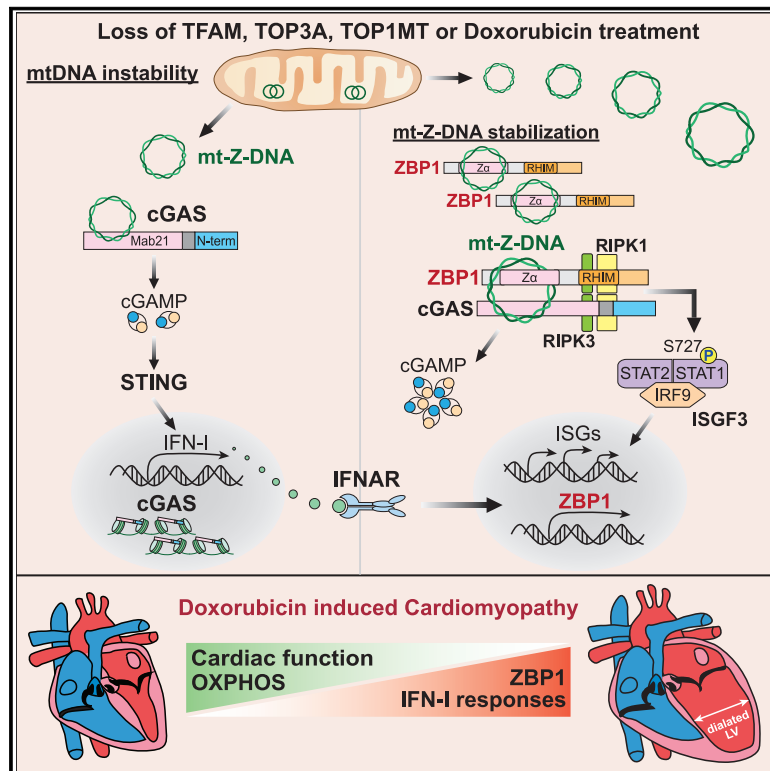


# Cooperative sensing of mitochondrial DNA by ZBP1 and cGAS promotes cardiotoxicity

## Graphical abstract



## Authors

Yuanjiu Lei, Jordyn J. VanPortfliet, Yi-Fan Chen, ..., Jason W. Upton, Pingwei Li, A. Phillip West

## Correspondence

awest@tamu.edu

## In brief

Coordinated interaction of the ZBP1 and cGAS pathways ties the sensing of mitochondrial Z-DNA to type I interferon signaling and cardiac damage.

## Highlights

- Mitochondrial genome instability promotes Z-DNA formation
- ZBP1 stabilizes Z-DNA released from mitochondria to sustain IFN-I signaling
- A ZBP1-cGAS complex recruits RIPK1 and RIPK3 to augment STAT1 phosphorylation
- ZBP1 contributes to cardiac IFN-I responses and chemotherapy-related heart failure



## Article

# Cooperative sensing of mitochondrial DNA by ZBP1 and cGAS promotes cardiotoxicity

Yuanjiu Lei,<sup>1</sup> Jordyn J. VanPortfliet,<sup>1,10</sup> Yi-Fan Chen,<sup>1,10</sup> Joshua D. Bryant,<sup>1</sup> Ying Li,<sup>2</sup> Danielle Fails,<sup>3</sup> Sylvia Torres-Odio,<sup>1</sup> Katherine B. Ragan,<sup>4</sup> Jingti Deng,<sup>5</sup> Armaan Mohan,<sup>5</sup> Bing Wang,<sup>2</sup> Olivia N. Brahms,<sup>6</sup> Shawn D. Yates,<sup>6</sup> Michael Spencer,<sup>3</sup> Carl W. Tong,<sup>7</sup> Marcus W. Bosenberg,<sup>8</sup> Laura Ciaccia West,<sup>1</sup> Gerald S. Shadel,<sup>9</sup> Timothy E. Shutt,<sup>5</sup> Jason W. Upton,<sup>6</sup> Pingwei Li,<sup>2</sup> and A. Phillip West<sup>1,11,12,\*</sup>

<sup>1</sup>Department of Microbial Pathogenesis and Immunology, School of Medicine, Texas A&M University, Bryan, TX 77807, USA

<sup>2</sup>Department of Biochemistry and Biophysics, Texas A&M University, College Station, TX 77843, USA

<sup>3</sup>Fortis Life Sciences, Montgomery, TX 77356, USA

<sup>4</sup>Department of Molecular Biosciences, University of Texas at Austin, Austin, TX 78712, USA

<sup>5</sup>Departments of Medical Genetics and Biochemistry & Molecular Biology, Cumming School of Medicine, University of Calgary, Calgary, AB T2N 1N4, Canada

<sup>6</sup>Department of Biological Sciences, Auburn University, Auburn, AL 36849, USA

<sup>7</sup>Department of Medical Physiology, School of Medicine, Texas A&M University, Bryan, TX 77807, USA

<sup>8</sup>Departments of Pathology, Dermatology, and Immunobiology, Yale School of Medicine, New Haven, CT 06520, USA

<sup>9</sup>Salk Institute for Biological Studies, La Jolla, CA 92037, USA

<sup>10</sup>These authors contributed equally

<sup>11</sup>Twitter: @WestLabMito

<sup>12</sup>Lead contact

\*Correspondence: [awest@tamu.edu](mailto:awest@tamu.edu)

<https://doi.org/10.1016/j.cell.2023.05.039>

## SUMMARY

Mitochondrial DNA (mtDNA) is a potent agonist of the innate immune system; however, the exact immunostimulatory features of mtDNA and the kinetics of detection by cytosolic nucleic acid sensors remain poorly defined. Here, we show that mitochondrial genome instability promotes Z-form DNA accumulation. Z-DNA binding protein 1 (ZBP1) stabilizes Z-form mtDNA and nucleates a cytosolic complex containing cGAS, RIPK1, and RIPK3 to sustain STAT1 phosphorylation and type I interferon (IFN-I) signaling. Elevated Z-form mtDNA, ZBP1 expression, and IFN-I signaling are observed in cardiomyocytes after exposure to Doxorubicin, a first-line chemotherapeutic agent that induces frequent cardiotoxicity in cancer patients. Strikingly, mice lacking ZBP1 or IFN-I signaling are protected from Doxorubicin-induced cardiotoxicity. Our findings reveal ZBP1 as a cooperative partner for cGAS that sustains IFN-I responses to mitochondrial genome instability and highlight ZBP1 as a potential target in heart failure and other disorders where mtDNA stress contributes to interferon-related pathology.

## INTRODUCTION

Under conditions of cellular stress and mitochondrial dysfunction, mitochondrial DNA (mtDNA) can be released into the cytoplasm or extracellular space to engage pattern recognition receptors (PRRs) including Toll-like receptor 9 (TLR9), NOD-like receptor family pyrin domain-containing 3 (NLRP3), cyclic GMP-AMP (cGAMP) synthase (cGAS), and Z-DNA binding protein 1 (ZBP1).<sup>1–6</sup> The detection of mtDNA can not only potentiate antimicrobial innate immunity during infection but may also drive detrimental inflammatory responses in disease and aging.<sup>7–9</sup> Despite growing evidence that mtDNA is an important innate immune agonist, many questions remain. Notably, the physiological and pathological contexts of mtDNA release and the molecular properties of mtDNA

that stabilize it in the cytosol and enhance detection by cGAS or other innate immune sensors have not been fully elucidated.

As a covalently closed circular genome, mtDNA lacks free DNA ends that can rotate to relieve the torsional strain induced during replication and transcription.<sup>10</sup> Consequently, the activity of mitochondrial replication and transcription machineries can generate overwound (positively supercoiled) and underwound (negatively supercoiled) regions of mtDNA, which may promote the formation of other immunostimulatory mtDNA structures if not properly resolved. Z-DNA is one such non-canonical structure that differs from canonical Watson-Crick B-DNA.<sup>11,12</sup> Sequences with alternating purine-pyrimidine regions have the highest propensity to form Z-DNA, although negative supercoiling of other sequences can promote B to Z



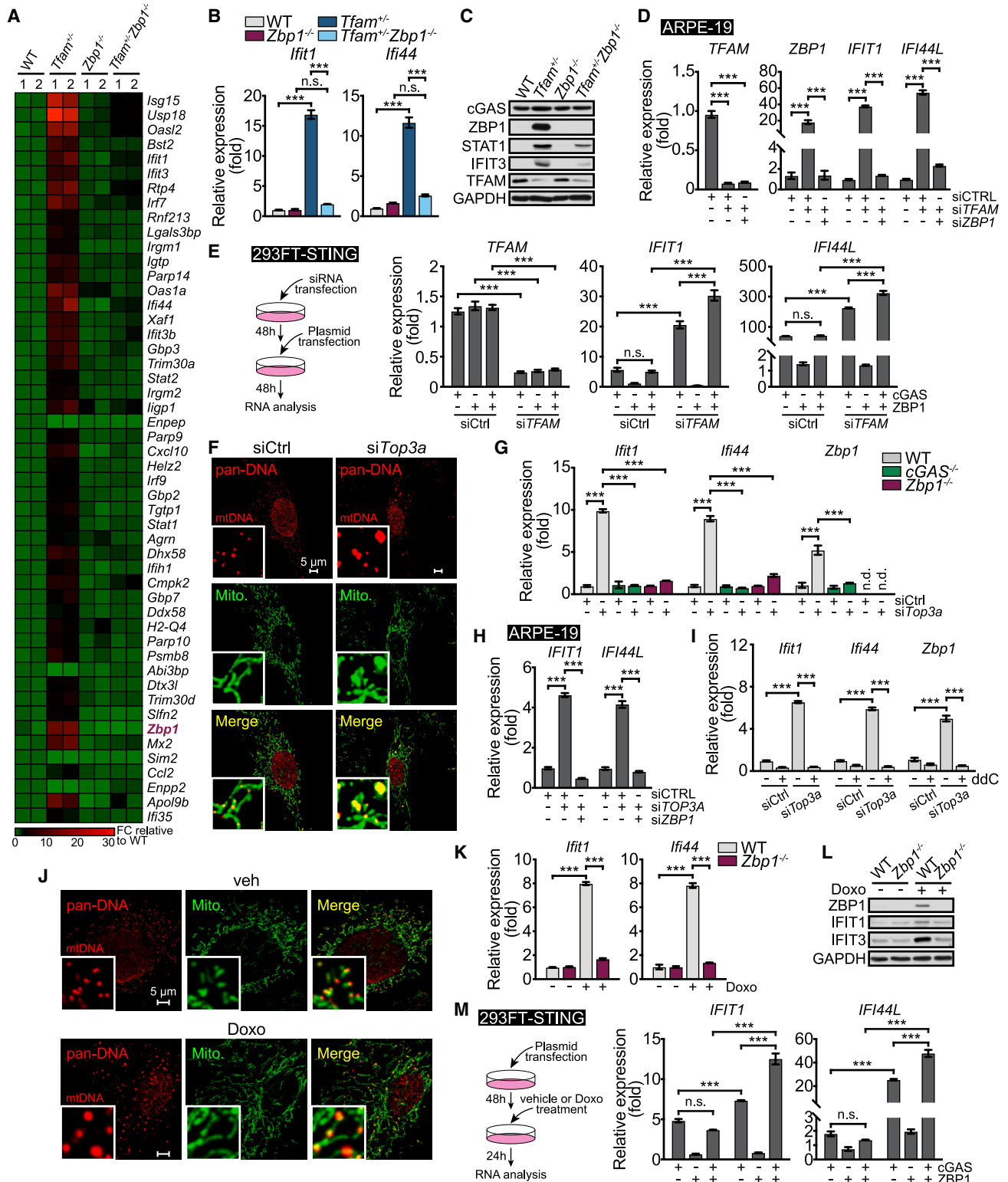


**Figure 1. ZBP1 sustains IFN-I responses to mitochondrial genome instability**

(A) RNA-seq heatmaps of top 50 genes with the lowest p values between WT and *Tfam*<sup>-/-</sup> genotypes. Fold changes (FCs) are normalized to the average of WT MEFs.

(legend continued on next page)

transition.<sup>13,14</sup> In mitochondria, the activities of DNA topoisomerase I mitochondrial (TOP1MT) and DNA topoisomerase III alpha (TOP3A) are required to relieve torsional mtDNA stress and relax negative supercoiling.<sup>10,12</sup> However, the degree to which torsional stress promotes B- to Z-DNA transition in mtDNA is unknown, and whether the acquisition of this unique DNA conformation enhances or sustains the immunostimulatory potential of mtDNA is presently unclear. Emerging evidence suggests that ZBP1 is a critical innate immune receptor for both nuclear Z-DNA and double-stranded Z-RNA<sup>15–24</sup>; however, a role for ZBP1 in sensing Z-form mtDNA has not been explored.

DNA damage is a main mechanism by which Doxorubicin (Doxo) and other anthracycline chemotherapeutics induce cancer cell death.<sup>25</sup> Unfortunately, Doxo has many adverse effects on the cardiovascular system and can cause acute cardiotoxicity, cardiomyopathy, and heart failure in cancer patients and survivors.<sup>26–30</sup> Mitochondrial dysfunction and mtDNA instability are strongly linked to Doxo-induced cardiotoxicity (DIC).<sup>25,31–35</sup> Notably, mice lacking TOP1MT are more susceptible to Doxo-induced mtDNA damage and cardiac dysfunction.<sup>36</sup> Doxo also induces mtDNA supercoiling,<sup>37</sup> suggesting that increased torsional strain or accumulation of non-canonical structures might underlie cardiac mtDNA instability in DIC. Finally, Doxo can trigger the release of mtDNA into the cytoplasm to activate cell-autonomous innate immune signaling through cGAS.<sup>38</sup> The cGAS-stimulator of interferon genes (STING) axis is increasingly implicated in cardiovascular diseases and heart failure,<sup>8,39–43</sup> raising the intriguing possibility that Doxo-induced mtDNA stress contributes to DIC via the activation of cGAS or other nucleic-acid-sensing PRRs such as ZBP1.

In this study, we report that ZBP1 is a key innate immune sensor of torsional mtDNA stress and mitochondrial Z-DNA release. We find that ZBP1 stabilizes Z-form mtDNA and nucleates the assembly of a cytosolic complex containing cGAS, receptor-interacting protein 1 (RIPK1), and RIPK3 to engage robust IFN-I signaling. Ablation of ZBP1 or IFN-I signaling limits cardiotoxicity and improves heart function after *in vivo* Doxo administration, shedding new light on the immune mechanisms of DIC and revealing a potential therapeutic avenue for cancer therapy-associated heart failure.

## RESULTS

### ZBP1 is required for maximal IFN-I induction downstream of mtDNA stress

Our prior work revealed persistent mitochondrial genome instability, cytosolic mtDNA release (Figure S1A), cGAS-STING signaling, and IFN-I responses in transcription factor A, mitochondrial (TFAM) heterozygous knockout cells (*Tfam*<sup>+/-</sup>).<sup>44</sup> Analysis of RNA-seq data from *Tfam*<sup>+/-</sup> mouse embryonic fibroblasts (MEFs) revealed elevated expression of multiple IFN-I-induced nucleic acid sensors including ZBP1, IFI200 family members, and mitochondrial antiviral signaling (MAVS)-dependent RNA helicases (Figures 1A and S1B). In contrast to *Sting*<sup>-/-</sup> cells, *Mavs*<sup>-/-</sup> MEFs maintained high levels of interferon-stimulated genes (ISGs) after TFAM silencing (Figure S1C), indicating that mitochondrial RNA release and sensing is not a major driver of IFN-I signaling in TFAM-deficient cells (Figure S1C). However, silencing of ZBP1 markedly attenuated ISG expression in *Tfam*<sup>+/-</sup> cells (Figure S1D). Additional analyses confirmed that loss of ZBP1 largely abrogated ISG expression in both TFAM-deficient MEFs (Figures 1A–1C) and human cells (Figure 1D). Experiments in STING-reconstituted 293FT cells (293FT-STING) revealed that co-expression of cGAS and ZBP1 potentiated TFAM depletion-induced ISG expression (Figure 1E). Collectively, these results indicate that ZBP1 is an essential sensor of mtDNA instability that synergizes with cGAS to sustain IFN-I signaling.

Reduced TFAM expression can alter mtDNA topology, promoting the transition from predominantly relaxed monomeric circles to catenated<sup>45</sup> or supercoiled mtDNA species (Figure S1E). The mitochondrial isoform of TOP3A functions to resolve mtDNA catenation and relax negative supercoiling induced during mtDNA replication and transcription.<sup>10,12,46,47</sup> As loss of TOP3A causes mtDNA torsional strain leading to mitochondrial nucleoid aggregation and instability similar to TFAM depletion (Figure 1F),<sup>46</sup> we next investigated whether silencing of TOP3A promotes mtDNA-dependent IFN-I signaling. Interestingly, siRNA knockdown of TOP3A in both mouse and human cells (Figures S1F and S1G) triggered robust ISG expression in a cGAS- and ZBP1-dependent fashion (Figures 1G and 1H). Selective depletion of mtDNA with the chain-terminating nucleoside 2',3'-dideoxycytosine (ddC) during TOP3A knockdown

(B and C) Quantitative reverse-transcriptase PCR (qRT-PCR) analysis (B) and western blots (C) of ISGs in WT, *Tfam*<sup>+/-</sup>, *Zbp1*<sup>-/-</sup>, and *Tfam*<sup>+/-</sup>*Zbp1*<sup>-/-</sup> MEFs. (D) qRT-PCR analysis in ARPE-19 transfected with indicated siRNAs for 72 h. (E) Schematic illustration of siRNA and plasmid transfection in 293FT-STING (left). qRT-PCR analysis in 293FT-STING transfected with indicated siRNAs and plasmids (0.25 μg/mL cGAS or ZBP1) (right). (F) Representative microscopy images of WT MEFs transfected with siCtrl or *siTop3a* and stained with anti-pan-DNA and -HSP60 (Mito.) antibodies. Inset panels are magnified 4×. (G) qRT-PCR analysis in WT, *cGAS*<sup>-/-</sup>, and *Zbp1*<sup>-/-</sup> MEFs transfected with siCtrl or *siTop3a* for 96 h. (H) qRT-PCR analysis in ARPE-19 transfected with indicated siRNAs for 72 h. (I) qRT-PCR analysis in WT MEFs transfected with siCtrl or *siTop3a* with or without 2',3'-dideoxycytidine (ddC, 100 μM) for 72 h. (J) Representative confocal microscopy images of WT MEFs treated with vehicle (veh) or Doxorubicin (Doxo, 500 nM, 24 h) and stained with anti-pan-DNA and -HSP60 (Mito.) antibodies. Inset panels are magnified 4×. (K and L) qRT-PCR analysis (K) and western blots (L) of ISGs in WT and *Zbp1*<sup>-/-</sup> MEFs treated with or without Doxo (50 nM, 48 h). (M) Schematic illustration of plasmid transfection and Doxo treatment in 293FT-STING (left). qRT-PCR analysis in 293FT-STING transfected with indicated plasmids (0.4 μg/mL cGAS or 0.8 μg/mL ZBP1) and with or without Doxo (200 nM) treatment (right). Statistical significance was determined using analysis of variance (ANOVA) and Tukey post hoc test (A, D, E, G, H, I, L, and M). \*p < 0.05, \*\*p < 0.01, and \*\*\*p < 0.001. Error bars represent SEM. See also Figure S1 and Table S1.



revealed that mtDNA, but not nuclear DNA, is the endogenous ligand driving IFN-I responses (Figures 11 and S1H). Mammalian mitochondria also house the type IB topoisomerase TOP1MT, which facilitates mtDNA decatenation by TOP3A and resolves positive and negative mtDNA supercoiling.<sup>12,47–49</sup> Similar to results with TOP3A, knockdown of TOP1MT triggered ISG expression in a cGAS-, ZBP1-, and mtDNA-dependent fashion (Figures S1I–S1L). Collectively, these data indicate that loss of several mitochondrial factors governing mtDNA packaging and topology promotes ISG expression via cGAS and ZBP1.

Doxo is a widely used anthracycline chemotherapeutic drug that induces mtDNA damage and mitochondrial dysfunction, in addition to nuclear DNA damage.<sup>25,31</sup> A recent study revealed that Doxo promotes mtDNA supercoiling and catenation,<sup>37</sup> and we observed that Doxo induced mtDNA nucleoid aggregation, similar to cells lacking TFAM or TOP3A (Figure 1J). Doxo treatment also promoted cytosolic mtDNA release, as well as upregulation of ZBP1 and other ISGs (Figures S1M–S1O). Moreover, Doxo-induced ISG expression was independent of MAVS but required mtDNA and signaling via the type I interferon receptor (IFNAR) (Figures S1P–S1R). Doxo-induced ISG expression was also markedly impaired in *Zbp1*<sup>-/-</sup> cells (Figures 1K and 1L). Pretreatment of *Zbp1*<sup>-/-</sup> MEFs with interferon beta (IFN $\beta$ ) before Doxo challenge failed to increase ISGs to the same level as Doxo-treated WT cells, indicating that another IFN-I-induced DNA sensor cannot compensate for the loss of ZBP1 (Figure S1S). Finally, experiments in 293FT-STING cells revealed that cGAS and ZBP1 synergize to enhance ISG expression in response to Doxo (Figure 1M). Despite these crucial roles for ZBP1 in promoting IFN-I responses downstream of mtDNA instability, we noted no requirement for ZBP1 in sensing linear B-form immunostimulatory DNA, consistent with reports from other groups<sup>15,17,50,51</sup> (Figure S1T). Moreover, ZBP1 was not required for cGAS-dependent ISGs triggered by inner mitochondrial membrane (IMM) herniation and caspase inhibition<sup>52–54</sup> (Figure S1U). In sum, these results suggest that ZBP1 is an innate immune sensor of mitochondrial genome instability that augments cGAS-STING-dependent IFN-I signaling in human and mouse cells.

### ZBP1 stabilizes Z-DNA generated during mtDNA stress

Bidirectional replication and transcription of circular mtDNA generates supercoiling that must be resolved by TOP1MT and TOP3A. This raises the possibility that increased mtDNA

supercoiling in TOP3A- or TOP1MT-deficient cells, and perhaps *Tfam*<sup>+/-</sup> and Doxo-treated cells, promotes the formation of Z-DNA for detection by ZBP1. To explore this hypothesis, we utilized the Z22 antibody that selectively binds Z-DNA *in vitro* and *in cellulo*.<sup>55–57</sup> Gel shift and slot blotting assays confirmed that the Z22 antibody strongly binds plasmid Z-DNA, but not a plasmid with the identical sequence in B-DNA confirmation (Figures 2A, 2B, S2A, and S2B). Moreover, the Z22 antibody efficiently labeled Z-DNA in the cell cytoplasm after transfection, but did not immunostain B-DNA, highlighting the utility of this reagent for fluorescent microscopy analysis of Z-DNA (Figure S2C).

Utilizing the Z22 antibody and quantitative immunofluorescence microscopy, we next screened for the presence of Z-DNA in cells experiencing mtDNA stress. Strikingly, we observed increased cytosolic and mitochondrial Z-DNA accumulation in TFAM, TOP3A, and TOP1MT knockdown cells (Figures 2C and 2D). Doxo also enriched Z-DNA in the cytosol and mitochondria as revealed by microscopy and slot blotting (Figures 2E, 2F, and S2D), further supporting the notion that perturbations enhancing mtDNA supercoiling promote the accumulation of Z-DNA. Depletion of mtDNA with ddC after silencing of TOP3A or TOP1MT, or Doxo treatment, reduced both mtDNA abundance and aggregation (Figure S2E) while also significantly decreasing overall Z-DNA intensity (Figure S2F), strongly indicating that mtDNA was the source of Z-DNA we observed. However, IMM herniation and caspase inhibition were insufficient in inducing cytosolic or mitochondrial Z-DNA accumulation (Figure S2G). Additional experiments in human cells confirmed increased Z-DNA abundance after TFAM silencing (Figures 2G and 2H). ZBP1 can stabilize Z-form DNA via its Z-DNA binding domains.<sup>58–61</sup> Interestingly, we observed less cytosolic Z-DNA after TFAM, TOP3A, or TOP1MT silencing in *Zbp1*<sup>-/-</sup> MEFs relative to WT MEFs, with similar trends seen after dual silencing of TFAM and ZBP1 in human cells (Figures 2D, 2G, and 2H). Exposure of *Tfam*<sup>+/-</sup> MEFs to the Z-DNA stabilizer hydralazine<sup>62,63</sup> dramatically increased overall Z-DNA staining and ISG expression in a ZBP1-dependent fashion (Figures S2H and S2I), suggesting that ZBP1 is required for robust Z-DNA accumulation in cells experiencing mtDNA stress.

We next sought to determine whether Z-DNA is intrinsically more immunostimulatory to the cGAS-IFN-I axis. Transient transfection of Z-DNA or B-DNA into WT cells elicited comparable ISG expression at early time points. However, Z-DNA was significantly more stimulatory at 12–24 h post-transfection

### Figure 2. Mitochondrial genome instability promotes Z-form DNA accumulation that is stabilized by ZBP1

(A) Schematic illustration of circular Z-form and B-form DNA synthesis.

(B) Electrophoretic mobility shift assay (EMSA) measurement of binding of Z-DNA-specific antibody Z22 to B-DNA and Z-DNA.

(C) Representative images of WT MEFs transfected with indicated siRNAs for 72 h and stained with anti-Z-DNA and -TOMM20 (Mito.) antibodies. Inset panels are magnified 4 $\times$ .

(D) Mean fluorescent intensity (MFI) quantification of cytosolic (Cyto.) and mitochondrial (Mito.) Z-DNA in WT and *Zbp1*<sup>-/-</sup> MEFs transfected with indicated siRNAs for 72 h. MFI percentiles are normalized to WT or *Zbp1*<sup>-/-</sup> MEFs transfected with siCtrl.

(E and F) Representative images of WT MEFs treated with veh or Doxo and stained with anti-Z-DNA and -TOMM20 (Mito.) antibodies (E). MFI of Cyto. and Mito. Z-DNA is quantified in (F). MFI percentiles are normalized to veh-treated WT MEFs.

(G and H) Representative images of ARPE-19 transfected with indicated siRNAs for 72 h and stained with anti-Z-DNA and -TOMM20 (Mito.) antibodies (G). Inset panels are magnified 4 $\times$ . MFI of Cyto. and Mito. Z-DNA is quantified in (H). MFI percentiles are normalized to ARPE-19 transfected with siCTRL.

(I) qRT-PCR analysis of ISGs in WT and *Zbp1*<sup>-/-</sup> MEFs transfected with B-DNA or Z-DNA (125 ng/mL) for indicated time. Statistical significance was determined using ANOVA (D and I) and Tukey post hoc test (D), or unpaired t test (F). \*p < 0.05, \*\*p < 0.01, and \*\*\*p < 0.001. Error bars represent SEM.

See also Figure S2.

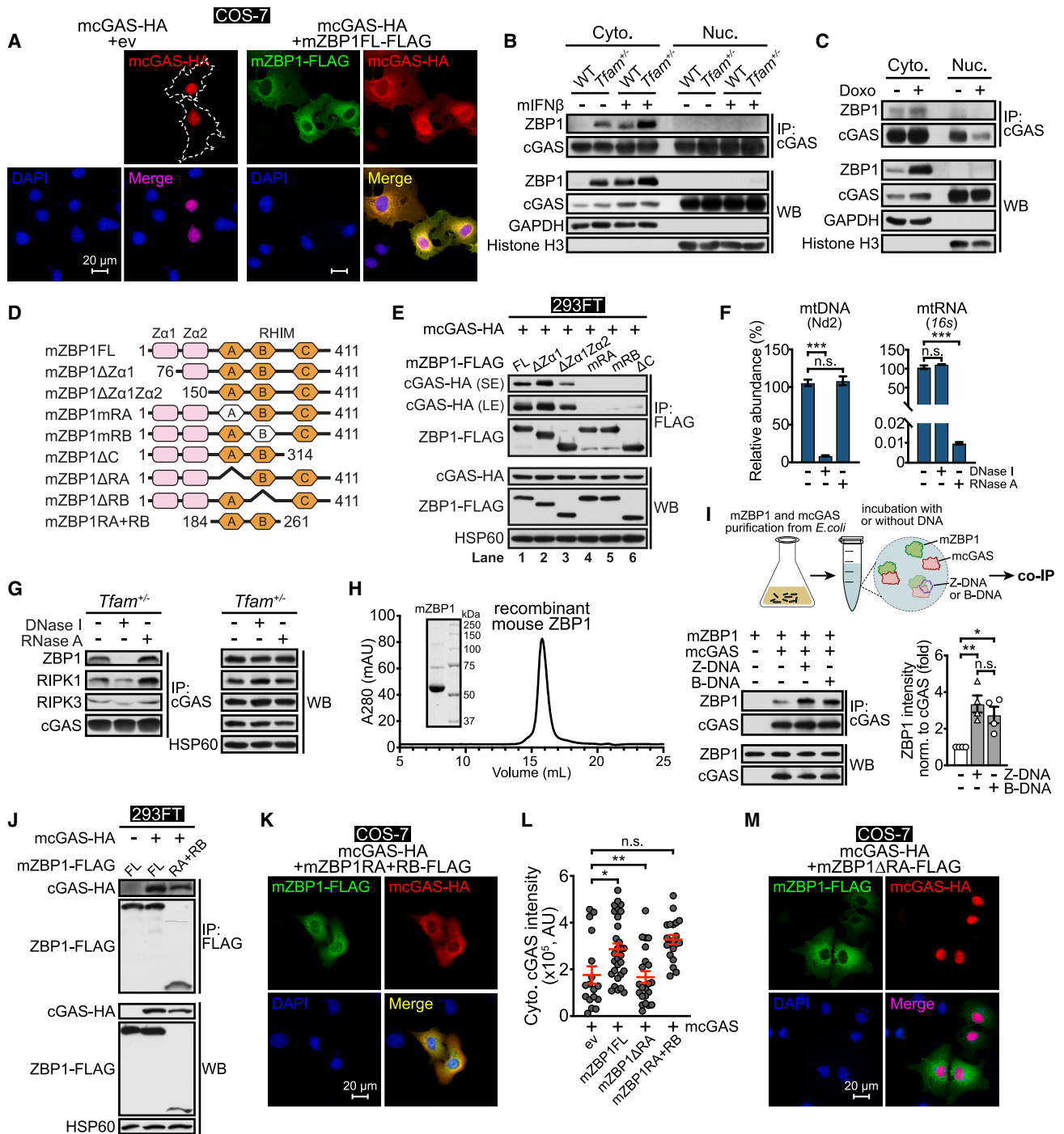


**Figure 3. ZBP1 binds to cGAS in a DNA- and RHIM-dependent manner**

(A) Representative images of COS-7 expressing indicated proteins and stained with anti-HA and -FLAG antibodies and 4',6-diamidino-2-phenylindole (DAPI) (ev, empty vector).

(B) Endogenous cytosolic and nuclear co-immunoprecipitations (coIP) in WT and *Tfam*<sup>-/-</sup> MEFs with or without mouse IFN $\beta$  (mIFN $\beta$ ) treatment (10 ng/mL, 6 h).

(C) Cytosolic and nuclear co-immunoprecipitation in WT MEFs treated with or without Doxo (50 nM, 48 h).

(D) Schematic representation of mouse ZBP1 full-length (mZBP1 FL), truncations and mutants in 293FT. SE, short exposure; LE, long exposure.

(E) CoIP showing interactions between mouse cGAS (mcGAS) and mZBP1 FL, truncations or mutants in 293FT. SE, short exposure; LE, long exposure.

(F) qPCR analysis of mt-DNA (left) or qRT-PCR analysis of mt-16s (right) in cell lysates from (G).

(G) Endogenous coIP in *Tfam*<sup>-/-</sup> MEFs with or without DNase I or RNase A treatment.

(H) Gel-filtration chromatography and SDS-PAGE analyses of recombinant mZBP1 protein.

(legend continued on next page)

(Figure 2I). Z-DNA and B-DNA elicited similar levels of ISGs in *Zbp1*<sup>-/-</sup> cells, suggesting that the Z-DNA stabilizing and/or signaling functions of ZBP1 are necessary to augment IFN-I signaling. Additional studies in spontaneously arising retinal pigment epithelial (ARPE)-19 cells confirmed findings in MEFs, revealing that Z-DNA is more stimulatory than B-DNA in human cells (Figure S2J). Finally, using an *in vitro* cGAS activity assay,<sup>64</sup> we observed no differences in cGAMP production in the presence of either DNA conformation, indicating that cGAS enzymatic activity is comparably induced by both B- and Z-DNA (Figure S2K). Collectively, these data show that Z-DNA is a potent IFN-I inducer and reveal that torsional mtDNA stress promotes the formation of Z-DNA that is stabilized by ZBP1.

### ZBP1 and cGAS form a DNA- and RHIM-dependent complex in the cytoplasm

Although Z-DNA did not stimulate more cGAMP production *in vitro*, we observed increased cGAMP levels in *Tfam*<sup>+/-</sup> and Doxo-exposed cells, which were dependent on ZBP1 (Figures S3A and S3B). We reasoned that increased cGAS activity downstream of mtDNA stress could result from ZBP1-dependent stabilization of Z-DNA ligands for detection by cGAS and/or the redistribution of cGAS to the cytosol. cGAS is predominately a nuclear protein<sup>64,65</sup>; however, we observed a significant increase in the proportion of cytosolic cGAS in ARPE-19 cells after TFAM knockdown (Figures S3C and S3D) that was dependent on ZBP1 (Figures S3C and S3D). Doxo treatment also resulted in elevated cGAS expression in cytosolic fractions (Figures S3E and S3F). To next explore whether ZBP1 could impact the distribution of cGAS independently of mtDNA stress, we transfected plasmids encoding human or mouse cGAS and ZBP1 into CV-1 in origin with SV40 genes (COS)-7 cells. Consistent with the endogenous expression pattern in most cells,<sup>65</sup> both human and mouse cGAS localized primarily to the nucleus upon transfection (Figures 3A and S3G). In contrast, cells co-expressing cGAS and full-length ZBP1 (ZBP1FL) exhibited higher cytosolic intensity of cGAS, which co-localized with ZBP1 (Figures 3A, 3L, S3G, and S3H). Consistent with these microscopy data, we observed a robust interaction between cGAS and ZBP1 in cytosolic immunoprecipitates (Figures 3E and S3I). Fractionation experiments revealed that ZBP1 localized to the cytosol in *Tfam*<sup>+/-</sup> as well as IFN-I- and Doxo-treated cells (Figures 3B, 3C, and S3E). Moreover, co-immunoprecipitation (coIP) assays in *Tfam*<sup>+/-</sup> and Doxo-treated cells demonstrated strong interactions between cGAS and ZBP1 in cytosolic, but not nuclear, extracts (Figures 3B and 3C).

Additional coIP experiments to identify the domains of cGAS mediating binding to ZBP1 revealed that ZBP1 interacted with both the N-terminal 147 aa of cGAS (cGAS N-term), as well as a construct lacking the first 147 amino acids ( $\Delta$ N-term) (Fig-

ure S3J), suggesting that at least two interaction sites bridge cGAS and ZBP1. To define the domains of ZBP1 necessary for interaction with cGAS, we first generated ZBP1 constructs lacking the first ( $\Delta$ Z $\alpha$ 1) or both Z-nucleic acid binding domains ( $\Delta$ Z $\alpha$ 1Z $\alpha$ 2) (Figure 3D). Upon transient expression of ZBP1 and cGAS constructs, we noted that the ZBP1 $\Delta$ Z $\alpha$ 1Z $\alpha$ 2 mutant was attenuated in binding cytosolic cGAS compared with ZBP1FL (Figure 3E, lanes 1 and 3). Using benzonase to degrade cytosolic nucleic acids before coIP (Figures S3K and S3L), we observed that ZBP1 was less efficient at pulling down cGAS after treatment (Figure S3M), mirroring the weaker interactions observed between the ZBP1 $\Delta$ Z $\alpha$ 1Z $\alpha$ 2 mutant and cGAS (Figure 2E). As cGAS and ZBP1 have been reported to bind various endogenous and exogenous nucleic acids,<sup>66-70</sup> we next sought to determine whether ZBP1-cGAS complexes forming in response to mtDNA instability requires DNA or RNA. DNase I or RNase A treatment was sufficient to degrade mtDNA or mtRNA in *Tfam*<sup>+/-</sup> cells, respectively (Figure 3F). However, only DNase I treatment diminished ZBP1-cGAS binding in *Tfam*<sup>+/-</sup> cells displaying mtDNA instability (Figure 3G). Finally, we developed a cell-free, *in vitro* binding assay to examine whether ZBP1 and cGAS interact directly and explore whether the interaction is potentiated by DNA. After expressing full-length mouse cGAS and ZBP1 in *E. coli* and purification by gel-filtration chromatography (Figure 3H), we performed *in vitro* IPs with or without Z- or B-DNA (Figure 3I). Strikingly, these experiments revealed that ZBP1 and cGAS bind directly and that the ZBP1-cGAS complex is stabilized by DNA. Despite increased ZBP1-cGAS interactions in the presence of DNA, ZBP1 did not augment the enzymatic activity of cGAS (Figure S3N). Overall, these data demonstrate that Z-DNA-binding domains of ZBP1 nucleate DNA-dependent interactions with cGAS.

As our *in vitro* IP experiments revealed that ZBP1 and cGAS can bind directly in the absence of DNA, we reasoned that other domains of ZBP1 might contribute to binding. In agreement, we noted that ZBP1 constructs possessing mutated RHIM domains (mRA, mRB) (Figure 3E, lanes 4-5), lacking RHIM A or RHIM B ( $\Delta$ RA,  $\Delta$ RB) (Figure S3O) or lacking a 97 aa C-terminal region containing the third RHIM domain ( $\Delta$ C) (Figure 3E, lane 6) weakly interacted with cGAS upon transient expression in 293FT cells. Moreover, a ZBP1 construct of roughly 100 amino acids containing only the RA and RB domains (RA + RB) was able to bind cGAS (Figure 3J). Cells expressing cGAS and ZBP1RA + RB exhibited increased cytosolic cGAS and protein co-localization like those expressing ZBP1FL (Figures 3K and 3L). However, cGAS staining was significantly more nuclear when co-expressed with the ZBP1 $\Delta$ RA mutant (Figures 3L and 3M), further supporting the notion that the cGAS and ZBP1 complex forms in the cytosol and is mediated, at least in part, by the ZBP1 RHIM domains.

(I) Schematic illustration of coIP between recombinant mcGAS and mZBP1 with or without DNA (top). CoIP showing interactions between mcGAS and mZBP1 with or without Z-DNA or B-DNA (bottom). Densitometry of ZBP1 in cGAS immunoprecipitates is shown in graph (n = 4).

(J) CoIP showing interactions between mcGAS and mZBP1 FL and RHIMA + RHIMB fragment (RA + RB) in 293FT.

(K-M) Representative images of COS-7 expressing indicated proteins and stained with anti-HA and -FLAG antibodies and DAPI (K and M). Cytosolic cGAS-HA intensity is quantified in (L). a.u., arbitrary unit. Statistical significance was determined using ANOVA and Tukey post hoc test (F and L). \*p < 0.05, \*\*p < 0.01, and \*\*\*p < 0.001. Error bars represent SEM.

See also Figure S3.

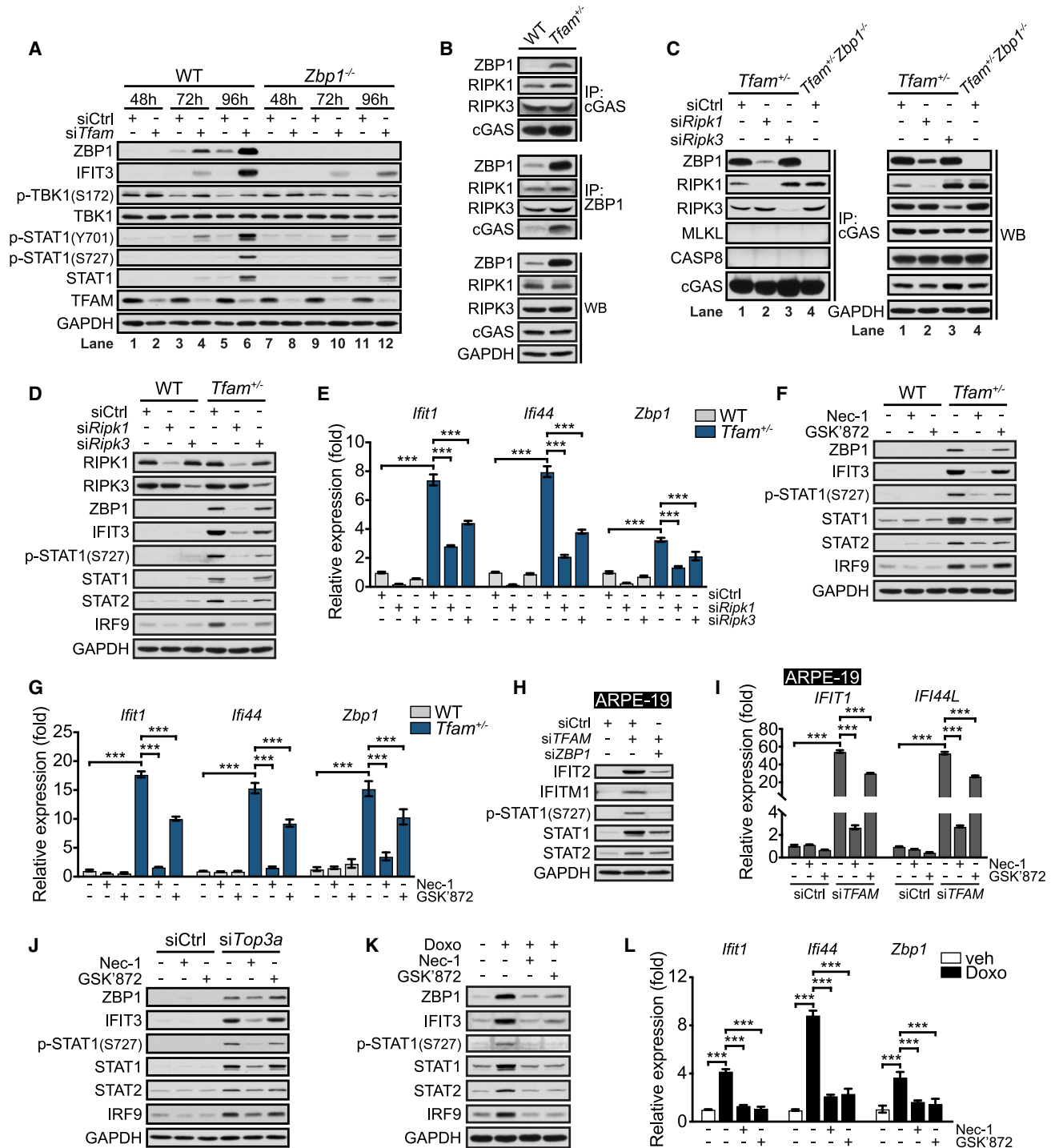


**Figure 4. RIPK1 and RIPK3 localize to the ZBP1-cGAS complex and sustain IFN-I signaling to mitochondrial genome instability**

(A) Western blots of WT and *Zbp1*<sup>-/-</sup> MEFs transfected with siCtrl or si*Tfam* for indicated time.

(B) Endogenous colP in WT and *Tfam*<sup>+/-</sup> MEFs.

(C) Endogenous colP in *Tfam*<sup>+/-</sup> and *Tfam*<sup>+/-</sup>*Zbp1*<sup>-/-</sup> MEFs transfected with indicated siRNAs for 48 h.

(D and E) Western blots (D) and qRT-PCR analysis (E) of WT and *Tfam*<sup>+/-</sup> MEFs transfected with indicated siRNAs for 72 h.

(F and G) Western blots (F) and qRT-PCR analysis (G) of WT and *Tfam*<sup>+/-</sup> MEFs treated with Necrostatin-1 (Nec-1, 10 μM) or GSK'872 (2.5 μM) for 48 h.

(H) Western blots of ARPE-19 transfected with indicated siRNAs for 72 h.

(I) qRT-PCR analysis in ARPE-19 transfected with siCTRL or si*TFAM* for 24 h and then treated with Nec-1 (100 μM) or GSK'872 (5 μM) for an additional 48 h.

(legend continued on next page)

### RIPK1 and RIPK3 localize to the ZBP1-cGAS complex and sustain IFN-I signaling to mitochondrial genome instability

We next sought to clarify the mechanisms by which ZBP1 amplifies IFN-I signaling downstream of mitochondrial genome instability and Z-DNA liberation. Similar to our previous transfection results (Figure 2I), we noted that expression of ISGs early after TFAM silencing (72 h) was similar between WT and *Zbp1*<sup>-/-</sup> cells (Figure 4A, lanes 4 and 10). We also observed similar levels of TBK1<sup>S172</sup> and STAT1<sup>Y701</sup> phosphorylation between WT and *Zbp1*<sup>-/-</sup> cells at the 72-h time point, suggesting that initial detection of cytosolic mtDNA by cGAS, activation of STING/TBK1, and the early production of IFN $\beta$  are independent of ZBP1. However, *Zbp1*<sup>-/-</sup> cells displayed markedly reduced IFIT3 and STAT1 expression 96 h post-TFAM silencing (Figure 4A, lanes 6 and 12), revealing that ZBP1 is required to sustain IFN-I signaling downstream of mtDNA instability. We also observed that ZBP1 is necessary for phosphorylation of STAT1 on serine 727 at late time points after TFAM silencing, noting a near ablation of phospho-STAT1<sup>S727</sup> in *Zbp1*<sup>-/-</sup> cells 96 h after TFAM knockdown.

Our prior data revealed that both RIPK1 and RIPK3 localize to the DNase-sensitive ZBP1-cGAS complex in *Tfam*<sup>+/-</sup> cells (Figure 3G), and therefore, we reasoned that RIPK recruitment/activation in the ZBP1-cGAS complex might sustain ISG expression. Interestingly, endogenous IP studies using a cGAS antibody showed that RIPK1 and RIPK3 form a complex with cGAS in WT cells and interact with ZBP1 upon its induction in *Tfam*<sup>+/-</sup> MEFs (Figure 4B, top). IPs using a ZBP1 antibody revealed that the small amount of ZBP1 in resting WT cells can also form a complex with RIPK1 and RIPK3 that minimally includes cGAS; however, we noted that the ZBP1-cGAS-RIPK1-RIPK3 complex was significantly enriched in *Tfam*<sup>+/-</sup> MEFs (Figure 4B, middle). Moreover, we observed that knockdown of RIPK1 in *Tfam*<sup>+/-</sup> cells was sufficient to reduce the total ZBP1 levels and, therefore, the amount of ZBP1 immunoprecipitating with cGAS, whereas silencing of RIPK3 had no effect on total ZBP1 or abundance of the ZBP1-cGAS complex (Figure 4C, lanes 2 and 3). cGAS also robustly immunoprecipitated both RIPK1 and RIPK3 in *Tfam*<sup>+/-</sup>*Zbp1*<sup>-/-</sup> MEFs (Figure 4C, lane 4). Finally, transfection of Z-DNA resulted in ZBP1 recruitment to the cGAS complex and augmented the level of RIPK1 co-immunoprecipitating with both proteins (Figure S4A). Collectively, these data suggest a model in which RIPK1 and RIPK3 form basal complexes with both DNA sensors, followed by the assembly of larger ZBP1-cGAS-RIPK1-RIPK3 complexes in the presence of Z-DNA ligands.

Phosphorylation of serine 727 in the transactivation domain of STAT1 is required to fully activate its transcriptional activity and is induced by multiple kinases including p38 MAPK, CDK8, and RIPK1.<sup>71-74</sup> Consistent with a role for RIPK1, we found that RIPK1 silencing dramatically reduced p-STAT1<sup>S727</sup> levels and

ISG expression in *Tfam*<sup>+/-</sup> fibroblasts, whereas RIPK3 silencing had more modest effects (Figures 4D and 4E). RIPK1 and RIPK3 inhibitor studies using Necrostatin-1 (Nec-1) and GSK'872 substantiated siRNA studies, revealing that the kinase activities of RIPK1 and RIPK3, to a lesser extent, govern p-STAT1<sup>S727</sup> levels and sustain ISG expression in MEFs exhibiting mtDNA instability (Figures 4F and 4G). Additional experiments confirmed that ZBP1 and RIPK1 kinase activity were essential for STAT1<sup>S727</sup> phosphorylation and ISG expression in human cells after TFAM silencing, whereas RIPK3 kinase activity was not as crucial (Figures 4H and 4I). RIPK1 and RIPK3 kinase activities were also required to sustain p-STAT1<sup>S727</sup> levels and ISG expression after silencing of TOP3A (Figures 4J and S4B) or TOP1MT (Figure S4C), as well as following exposure to Doxo (Figures 4K and 4L). Moreover, we observed that Z-DNA more potently induced IFIT3 in WT cells, likely due to increased STAT1 phosphorylation at serine 727. However, consistent with our ISG expression data (Figure 2I), both Z- and B-DNA induced comparable p-STAT1<sup>S727</sup> and similar ISG expression in *Zbp1*<sup>-/-</sup> cells (Figure S4D). Importantly, the kinase activities of RIPK1 and RIPK3 are not required for IFN-I responses triggered by canonical cGAS-STING signaling (Figure S4E), RIG-I-like receptor (RLR)-MAVS signaling (Figure S4F), or cGAS-STING signaling induced by IMM herniation and release of B-form mtDNA (Figure S4G). Taken together, these data show that following induction of mitochondrial genome stress and Z-DNA liberation, the ZBP1-cGAS complex promotes activation of RIPK1 and RIPK3, which augment STAT1<sup>S727</sup> phosphorylation, increase expression and transcriptional activity of the ISG factor 3 (ISGF3) complex, and sustain ISG expression.

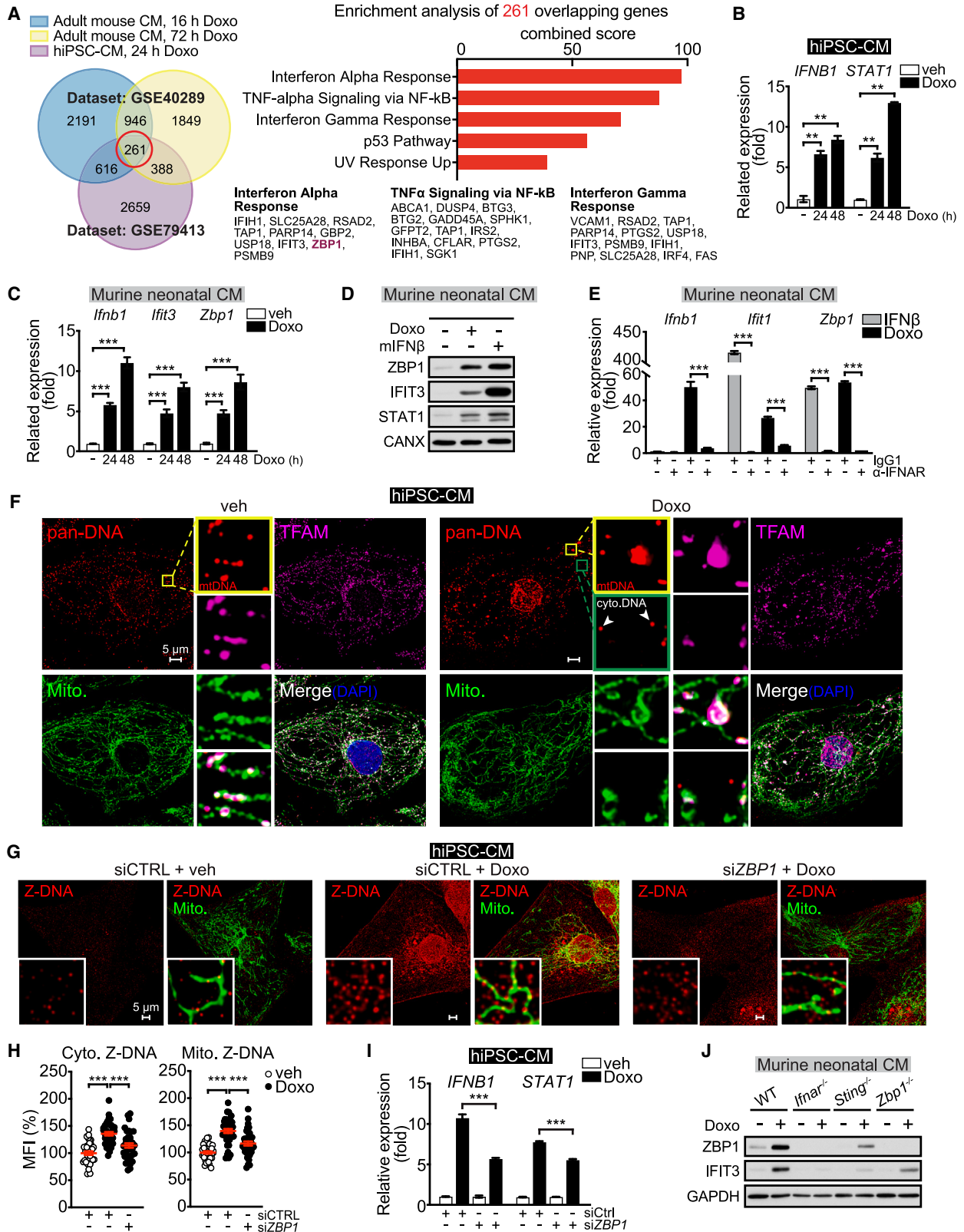
ZBP1 is a well-appreciated driver of RIPK3 and mixed lineage kinase domain-like pseudokinase (MLKL)-dependent necroptosis, an inflammatory form of cell death that can be induced by interferon and can feed forward to potentiate IFN-I and pro-inflammatory responses.<sup>16,75-79</sup> To examine the possibility that MLKL promotes mtDNA instability and release in *Tfam*<sup>+/-</sup> cells, we silenced MLKL by siRNA. Notably, *Tfam*<sup>+/-</sup> MEFs depleted of MLKL continued to show mitochondrial nucleoid aggregation and elevated ISG expression (Figures S4H-S4J). Moreover, WT and *Tfam*<sup>+/-</sup> MEFs were similarly susceptible to necroptosis triggered by tumor necrosis factor  $\alpha$  (TNF- $\alpha$ ) + z-VAD-FMK (zVAD) + cycloheximide (CHX) treatment (Figure S4K). Cell death triggered by Doxo was also equivalent between WT and *Zbp1*<sup>-/-</sup> MEFs (Figure S4L). In sum, these results suggest that the ZBP1-cGAS complex senses mtDNA genome instability and engages RIPK1 and RIPK3 to sustain IFN-I signaling independently of MLKL and a feedforward loop of cell death.

### Doxo induces a ZBP1-dependent IFN-I response in CMs

*Top1mt*<sup>-/-</sup> mice exhibit increased mtDNA instability, mitochondrial dysfunction, and cardiac injury after Doxo.<sup>36</sup> Consistent with our findings in fibroblasts, we also noted increased ISG

(J) Western blots of WT MEFs transfected with siCtrl or siTop3a for 48 h and then treated with Nec-1 (10  $\mu$ M) or GSK'872 (2.5  $\mu$ M) for an additional 48 h. (K and L) Western blots (K) and qRT-PCR analysis (L) of WT MEFs treated with veh or Doxo (50 nM) for 24 h and then treated with Nec-1 (10  $\mu$ M) or GSK'872 (2.5  $\mu$ M) for an additional 24 h. Statistical significance was determined using ANOVA and Šidák (E, G, I, and L). \*p < 0.05, \*\*p < 0.01, and \*\*\*p < 0.001. Error bars represent SEM.

See also Figure S4.



(legend on next page)

expression in neonatal cardiomyocytes (CMs) after TOP1MT knockdown, which was entirely dependent on ZBP1 (Figure S5A). Early work in rodents reported the preferential accumulation of cardiac mtDNA damage after Doxo that lingered for weeks after administration.<sup>35</sup> Given the high mtDNA content in CMs, we hypothesized that Doxo might trigger mtDNA genome instability and cytosolic release in CMs, leading to elevated ZBP1-cGAS signaling and IFN-I responses. We first mined two publicly available microarray datasets of CMs challenged with Doxo.<sup>80,81</sup> Gene set enrichment analysis showed that Doxo treatment increased expression of innate immune and inflammatory genes, including those associated with IFN-I, TNF- $\alpha$ , and DNA damage signaling (Figures 5A and S5B). Furthermore, analysis of differentially expressed genes across all datasets indicated that IFN-I signaling (interferon alpha response) was the most heavily enriched network (Figure 5A). In line with these bioinformatic analyses, Doxo strongly upregulated type I interferons, ZBP1, and other ISGs in human-induced pluripotent stem cell-derived CMs (hiPSC-CMs) and murine neonatal CMs in a time-dependent fashion (Figures 5B and 5C). Treatment of CMs with IFNAR blocking antibody further confirmed that IFN-I, but not IFN $\gamma$  or NF- $\kappa$ B signaling, was responsible for Doxo-induced ISG expression (Figures 5D and 5E). Suggestive of a role for Doxo in promoting mitochondrial stress, exposure of hiPSC-CMs to Doxo caused pronounced mtDNA nucleoid aggregation, mitochondrial network hyperfusion, and the accumulation of cytosolic DNA (Figure 5F). Moreover, Doxo treatment increased the intensity of Z-DNA in CMs, which was significantly reduced in cells depleted of ZBP1 (Figures 5G, 5H, and S5C). ZBP1 silencing also attenuated expression of Doxo-induced ISGs in hiPSC-CMs (Figure 5I), and Doxo failed to induce robust ISG expression in *Ifnar*<sup>-/-</sup>, *Sting*<sup>-/-</sup>, and *Zbp1*<sup>-/-</sup> neonatal CMs (Figure 5J). Collectively, these results indicate that Doxo promotes mtDNA genome instability in CMs, leading to Z-DNA accumulation that triggers the ZBP1-cGAS-IFN-I signaling axis.

Clinical case reports have linked IFN $\alpha$  immunotherapy to cardiomyopathy and other serious cardiac complications<sup>82-87</sup>; however, the direct effects of IFN-I on CM function have not been characterized. Interestingly, we observed that hiPSC-CMs are highly responsive to IFN-I (Figure S5D). Furthermore, IFN-I treatment increased expression of markers of CM injury

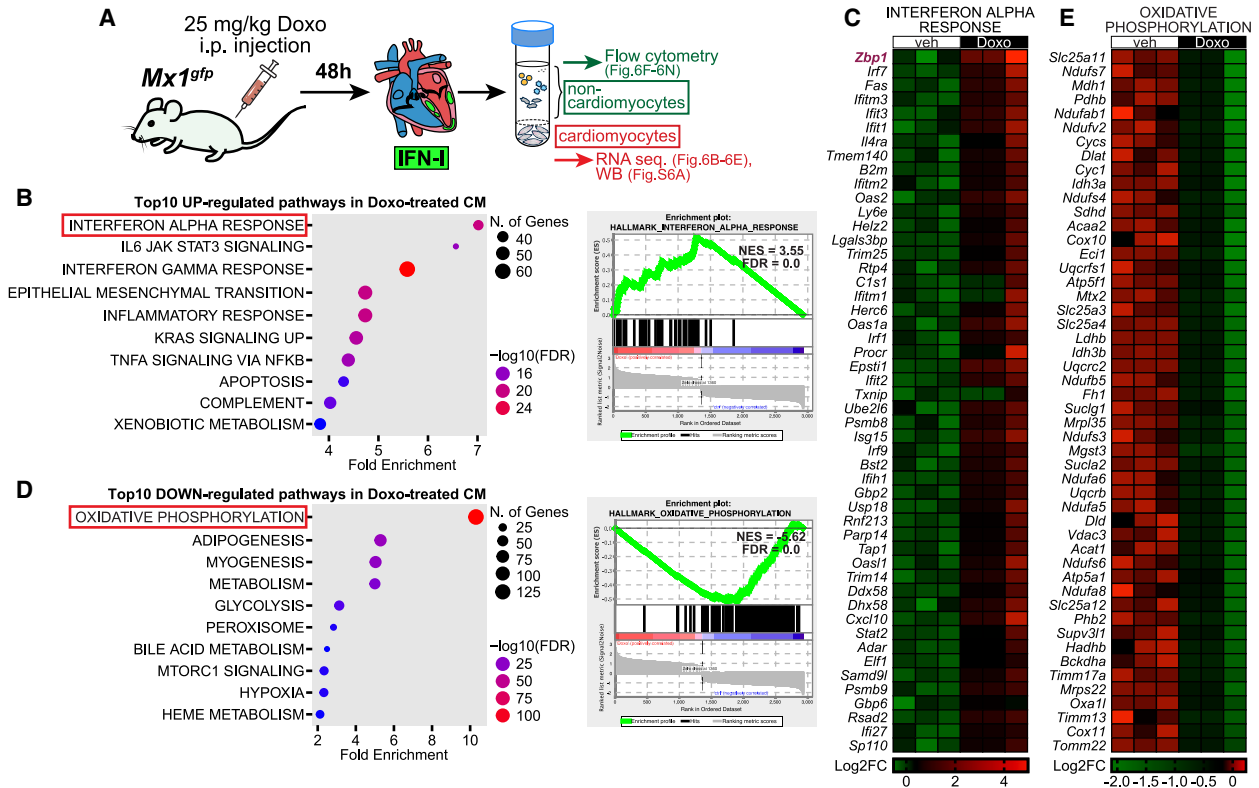
(Figure S5E) and reduced expression of mtDNA-encoded oxidative phosphorylation (OXPHOS) genes (Figure S5F). Reduced mtDNA-encoded OXPHOS gene expression was also observed in murine neonatal CMs exposed to IFN $\beta$  or Doxo (Figure S5G). Using a real-time imaging assay to measure hiPSC-CM beat rate and morphological appearance, we observed that both IFN-I and Doxo treatment altered CM beat periodicity and induced significant vacuolization after prolonged exposure (Figure S5H). Together, these results indicate that Doxo-induced mtDNA instability triggers a ZBP1-dependent IFN-I response that potentiates CM dysfunction.

### Doxo induces IFN-I responses in CMs and cardiac myeloid cells *in vivo*

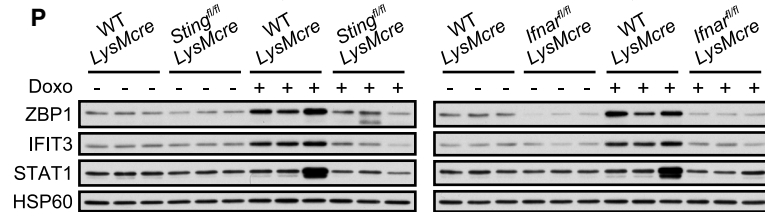
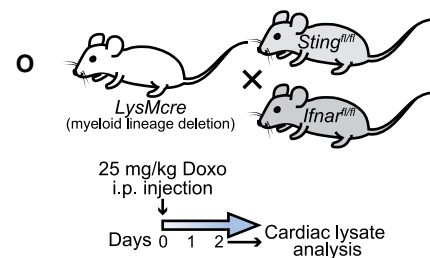
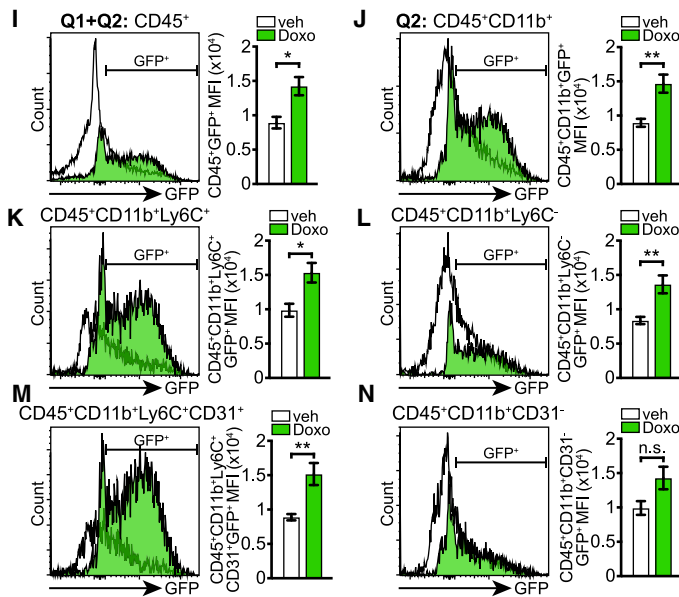
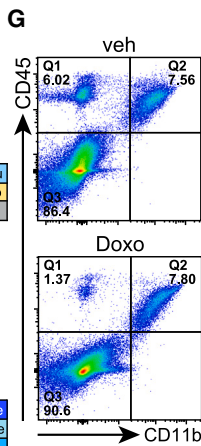
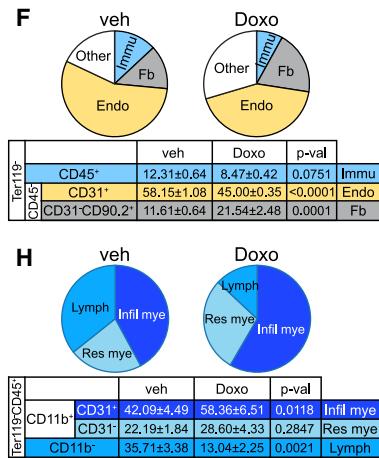
To next determine the cellular sources and immediate kinetics of cardiac IFN-I after *in vivo* Doxo challenge, we employed a high-dose, acute-exposure protocol and assessed gene expression in CMs by RNA-seq and IFN-I activation in non-CM populations by flow cytometry (Figure 6A). Expression profiling of highly enriched CMs extracted from Doxo-exposed hearts<sup>88,89</sup> uncovered a striking upregulation of innate immune signatures mirroring our *in vitro* studies. Pathway analysis revealed “interferon alpha response” as the most significantly upregulated node in CMs post-Doxo challenge (Figure 6B), with *Zbp1* representing the most highly expressed ISG (Figure 6C; Table S2). Analysis of the top downregulated pathways revealed strong inhibition of metabolic and myogenesis-related genes, with “oxidative phosphorylation” representing the most inhibited node in CMs from Doxo-challenged hearts (Figure 6D). Numerous genes functioning in mitochondrial oxidative metabolism were downregulated in CMs (Figure 6E; Table S2), which is consistent with the well-appreciated mitochondrial toxicity of Doxo. Western blotting of purified CMs confirmed our RNA-seq results and showed elevated ZBP1 and IFIT3 along with reduced OXPHOS subunits ATP5A1, SDHB, and NDUF8 from Doxo-exposed hearts relative to vehicle controls (Figure S6A). Utilizing a tamoxifen (TAM)-inducible, CM-specific Cre recombinase expressing strain ( $\alpha$ MHC-MerCreMer) crossed onto *Sting*<sup>fl/fl</sup> and *Ifnar*<sup>fl/fl</sup> mice (Figure S6B), we observed that ablation of the cGAS-STING pathway or IFN-I signaling reduced ZBP1 expression in cardiac lysates, and other ISGs to a lesser extent (Figure S6C). This

### Figure 5. Doxorubicin induces mtDNA instability, mitochondrial Z-DNA accumulation, and IFN-I responses in cardiomyocytes

- (A) Venn diagram of differentially expressed genes overlapping across datasets GSE40289 and GSE79413 (left). The top 5 pathways identified from the 261 commonly expressed genes from all three datasets (right). Shared gene lists from the top 3 pathways are shown (bottom).  
 (B and C) qRT-PCR analysis in veh or Doxo (250 nM) treated human-induced pluripotent stem cell-derived cardiomyocytes (hiPSC-CMs) (B) and murine neonatal CM (C).  
 (D) Western blots in Doxo (500 nM, 24 h) or mouse IFN $\beta$  (mIFN $\beta$ , 1 ng/mL, 4 h) treated murine neonatal CMs.  
 (E) qRT-PCR analysis in anti-IgG1 or -interferon receptor 1 ( $\alpha$ -IFNAR) antibody-blocked murine neonatal CMs exposed to mIFN $\beta$  (1 ng/mL, 4 h) or Doxo (500 nM, 24 h) treatment. CMs were pre-treated with anti-IgG1 or -IFNAR antibody at 15  $\mu$ g/mL for 5 h before subjecting to mIFN $\beta$  (1 ng/mL, 4 h) or Doxo (500 nM, 24 h) treatment.  
 (F) Representative images of hiPSC-CMs treated with veh or Doxo and stained with anti-DNA, -TFAM, and -PDH (Mito.) antibodies and DAPI. Inset panels are magnified 7 $\times$ .  
 (G and H) Representative images of hiPSC-CMs transfected with siCTRL or siZBP1 for 48 h, treated with veh or Doxo (500 nM) for an additional 24 h and stained with anti-Z-DNA and -PDH (Mito.) antibodies (G). Inset panels are magnified 12 $\times$ . MFI quantification of Cyto. and Mito. Z-DNA is quantified in (H). MFI percentiles are normalized to veh-treated hiPSC-CMs.  
 (I) qRT-PCR analysis in hiPSC-CMs transfected with siCTRL or siZBP1 for 24 h and then treated with veh or Doxo (250 nM) for an additional 48 h.  
 (J) Western blots in Doxo (500 nM, 24 h) treated WT, *Ifnar*<sup>-/-</sup>, *Sting*<sup>-/-</sup>, and *Zbp1*<sup>-/-</sup> murine neonatal CMs. Statistical significance was determined using unpaired t test (B, C, and E) or ANOVA and Tukey post hoc test (H and I). \*p < 0.05, \*\*p < 0.01, and \*\*\*p < 0.001. Error bars represent SEM.  
 See also Figure S5.



non-cardiomyocytes, from Fig.6A



(legend on next page)

indicates that CMs *in vivo* are capable of directly sensing Doxo-induced DNA damage via STING and responding to IFN-I, but it also reveals that other cardiac cell types contribute to IFN-I responses in the Doxo-exposed heart.

To complement our enriched CM RNA-seq data and identify non-myocyte populations contributing to IFN-I responses in the heart after Doxo challenge, we utilized a *Mx1<sup>gfp</sup>* ISRE reporter mouse that expresses GFP under control of the IFN-I-regulated, endogenous *Mx1* locus.<sup>90</sup> We focused on abundant non-CM populations including Ter119<sup>-</sup>CD45<sup>+</sup> immune cells, Ter119<sup>-</sup>CD45<sup>-</sup>CD31<sup>+</sup> endothelial cells, and Ter119<sup>-</sup>CD45<sup>-</sup>CD31<sup>-</sup>CD90.2<sup>+</sup> fibroblasts.<sup>91</sup> Using these multiplex panels, we observed that Doxo promoted remodeling in all non-myocyte cardiac cell populations, with a notable decrease in endothelial cells and an increase in fibroblasts (Figure 6F). Although CD45<sup>+</sup>CD11b<sup>-</sup> cardiac lymphoid populations decreased after Doxo, the percentage of CD45<sup>+</sup>CD11b<sup>+</sup> myeloid immune cells remained constant (Figure 6G). However, CD45<sup>+</sup>CD11b<sup>+</sup> cells expressing platelet/endothelial cell adhesion molecule 1 (PECAM-1; CD31), which governs leukocyte transmigration through vascular endothelial cells and recruitment into inflamed tissues, were increased in Doxo-exposed hearts (Figure 6H).<sup>92,93</sup> Despite significant changes in cardiac CD45<sup>-</sup> cell numbers and CD45<sup>+</sup>CD11b<sup>-</sup> lymphocyte abundance, *Mx1<sup>gfp</sup>* intensity was not altered in either population after Doxo treatment (Figures S6D and S6E). However, *Mx1<sup>gfp</sup>* expression was markedly increased in CD45<sup>+</sup>CD11b<sup>+</sup> cardiac myeloid cells (Figures 6I and 6J) composed of Ly6C<sup>+</sup> monocytes (Figure 6K) and Ly6C<sup>-</sup> macrophages and dendritic cells (Figure 6L).<sup>94</sup> Most Ly6C<sup>+</sup> monocytes exhibiting high *Mx1<sup>gfp</sup>* also expressed CD31 in Doxo-exposed hearts relative to vehicle controls (Figure 6M). In contrast, CD11b<sup>+</sup>CD31<sup>-</sup> cells did not exhibit significant increases in *Mx1<sup>gfp</sup>* (Figure 6N), indicating that recruited myeloid cells are largely responsible for non-CM IFN-I signaling post-Doxo. Consistent with a role for myeloid immune cells in the cardiac IFN-I program induced by Doxo, conditional ablation of STING (*Sting<sup>fl/fl</sup>LysMcre*) or IFNAR (*Ifnar<sup>fl/fl</sup>LysMcre*) in myeloid cells (Figure 6O) markedly reduced ZBP1 and other ISGs in cardiac lysates (Figure 6P). Finally, we observed that ZBP1 is upregulated in cardiac extracts and interacts strongly with cGAS after *in vivo* Doxo challenge (Figure S6F). Collectively, these data suggest

that Doxo induces significant cardiac remodeling, robust ZBP1-cGAS complex assembly, and IFN-I responses *in vivo*.

### Adjuvant IFN $\alpha$ synergizes with Doxo to enhance cardiac and mitochondrial dysfunction in tumor-bearing mice

In order to advance the mechanistic understanding of IFN-I-mediated cardiotoxicity, we merged an autochthonous melanoma model<sup>95,96</sup> with an extended Doxo protocol that more closely resembles clinical timelines in late DIC (Figure S6G). Doxo chemotherapy significantly restricted melanoma growth, with adjuvant IFN $\alpha$  providing a modest synergistic effect (Figure S6H). Transthoracic echocardiographic analyses 4 weeks after cessation of Doxo chemotherapy revealed reduced left ventricular ejection fraction (EF), fractional shortening (FS), and left ventricle (LV) mass in tumor-bearing mice (Figure S6I). This was accompanied by significant LV dilation, wall thinning, and cardiac fibrosis (Figures S6J–S6L). Consistent with our acute Doxo challenge model, we noted that ZBP1 and other ISGs were elevated in Doxo-exposed hearts relative to mice receiving vehicle only (Figure S6M). Strikingly, adjuvant IFN $\alpha$  treatment further exacerbated LV dysfunction, fibrosis, and cardiac ISG expression compared with the Doxo-only group (Figures S6I–S6M). Finally, melanoma-bearing mice receiving Doxo and IFN $\alpha$  showed reduced OXPHOS protein expression and cardiac mtDNA abundance (Figures S6N and S6O). These results suggest that IFN-I signaling synergizes with Doxo to promote mitochondrial dysfunction and heart injury in tumor-bearing mice.

### ZBP1 regulates cardiac IFN-I responses that contribute to Doxo-induced cardiomyopathy

As our data indicate that multiple cardiac populations contribute to IFN-I responses that potentiate Doxo-induced cardiac dysfunction, we next employed a chronic Doxo dosing regimen on ZBP1, STING, and IFNAR constitutive knockouts (Figure 7A). Echocardiography of WT mice revealed marked impairments in cardiac functional measures after Doxo (Figure 7B). In contrast, mice lacking ZBP1, STING, or IFNAR exhibited higher EF and FS compared with WT throughout the longitudinal study (Figure 7B). In-depth analysis of longitudinal echocardiographic measurements showed that *Zbp1<sup>-/-</sup>*, *Sting<sup>-/-</sup>*, and *Ifnar<sup>-/-</sup>* mice

### Figure 6. Doxorubicin induces ZBP1 and IFN-I responses in cardiomyocytes and cardiac myeloid cells *in vivo*

(A) Doxo i.p. challenge regimen, cardiac cell isolation, and applications diagram.

(B and D) Pathway analysis of RNA-seq data from cardiomyocytes isolated from adult mouse hearts post Doxo challenge compared to veh controls. Dot plots (left) and enrichment plots (right) were generated from ShinyGo and gene set enrichment analysis (GSEA) software, respectively. NES, normalized enrichment score; FDR, false discovery rate.

(C and E) Heatmaps of RNA-seq data displaying the top 50 upregulated genes in interferon alpha response pathway (C) and top 50 downregulated genes in oxidative phosphorylation pathway (E). Log<sub>2</sub> fold changes (log<sub>2</sub>FC) are normalized to the average of veh-challenged CMs.

(F) Pie charts of major non-cardiomyocyte (non-CM) populations: immune cells (Immu), endothelial cells (Endo), and fibroblasts (Fb), compositions in veh- and Doxo-challenged mouse hearts (n = 3 per treatment).

(G) Flow cytometric analysis of CD45 and CD11b on non-CM isolated from veh and Doxo-challenged mouse hearts.

(H) Pie charts of major immune cell populations: infiltrating myeloid cells (Infil mye), resident myeloid cells (Res mye) and lymphocytes (Lymph), in veh and Doxo challenge mouse hearts (n = 4 per treatment).

(I–N) Flow cytometric analysis of *Mx1<sup>gfp</sup>* cells in indicated cardiac immune subpopulations. Histograms are representative of 4 independent experiments. MFI quantifications are shown on the right.

(O) Generation of myeloid-specific STING and IFNAR knockout mouse strains (top) and Doxo administration regimen (bottom).

(P) Western blots in cardiac lysates from WT *LysMcre*, *Sting<sup>fl/fl</sup>LysMcre*, and *Ifnar<sup>fl/fl</sup>LysMcre* mice post veh or Doxo challenge (n = 3 per genotype per challenge).

Statistical significance was determined using unpaired t test (I–N). \*p < 0.05, \*\*p < 0.01, and \*\*\*p < 0.001. Error bars represent SEM.

See also Figure S6 and Table S2.

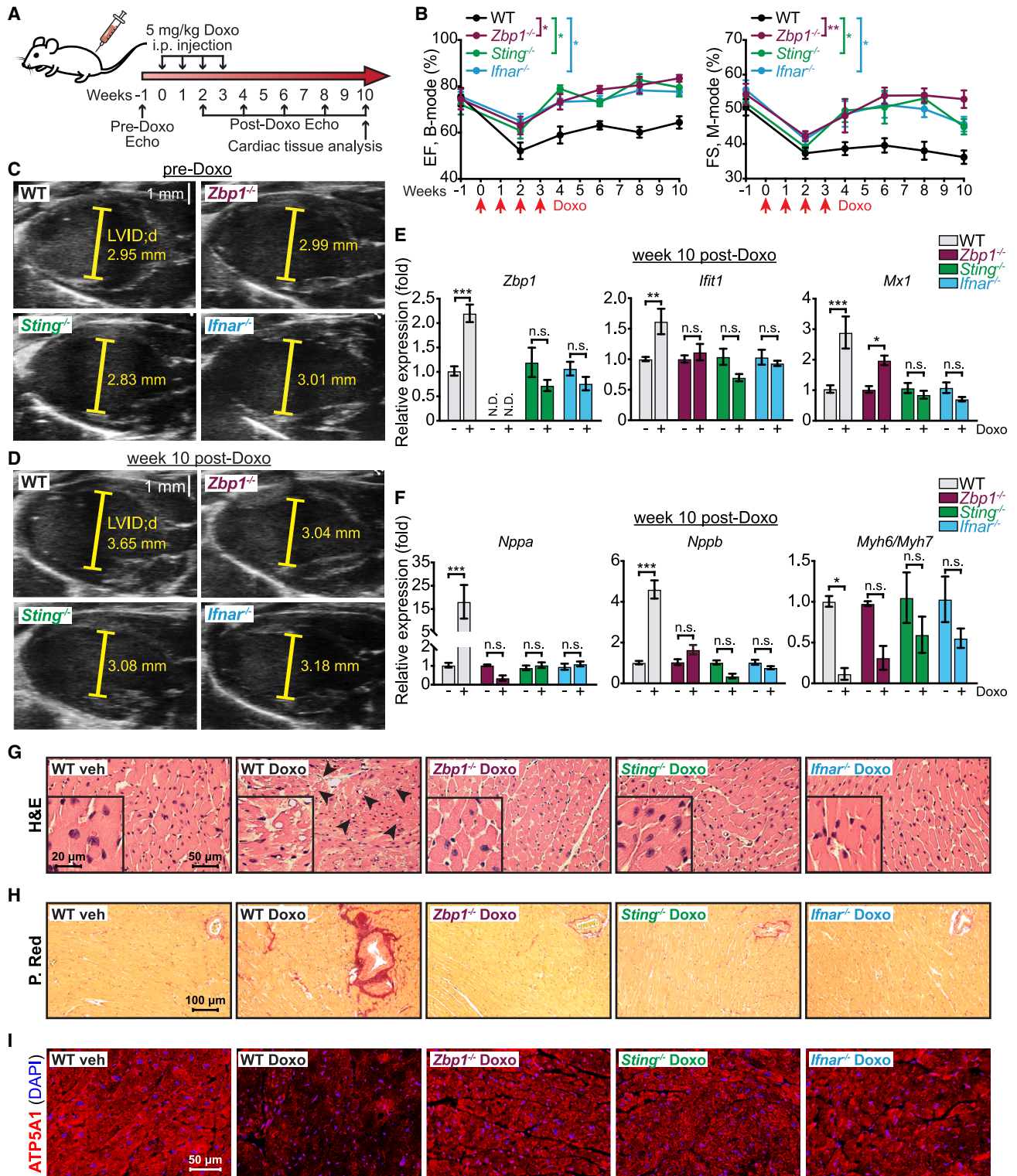


**Figure 7. The ZBP1-IFN-I axis contributes to Doxorubicin-induced cardiac injury and cardiomyopathy**

(A) Doxo i.p. challenge regimen, longitudinal cardiac monitoring, and cardiac harvest time point diagram.

(B) Left ventricular ejection fraction (EF) and fractional shortening (FS) calculated from B-mode or M-mode images ( $n = 6$  per genotype).

(C and D) Representative parasternal long axis images from each genotype pre-Doxo (C) and at week 10 post Doxo challenge (D).

(legend continued on next page)

displayed less Doxo-induced wall thinning, LV dilation, and weight loss compared with WT controls (Figures 7C, 7D, and S7A–S7C). To link cardiac dysfunction with sustained IFN-I signaling, we examined transcript and protein abundance of ISGs 7 weeks after the cessation of Doxo injection. WT mice exhibited sustained expression of ISGs assayed at week 10 post-Doxo. In contrast, ZBP1 and other ISGs were significantly lower or not induced in Doxo-exposed *Zbp1*<sup>-/-</sup>, *Sting*<sup>-/-</sup>, and *Ifnar*<sup>-/-</sup> mice (Figures 7E and S7D). Moreover, all knockout strains exhibited reduced cardiac expression of gene signatures associated with heart failure (Figure 7F). Histologic analyses of Doxo-challenged *Zbp1*<sup>-/-</sup>, *Sting*<sup>-/-</sup>, and *Ifnar*<sup>-/-</sup> mice revealed less CM vacuolization (Figures 7G and S7E) and reduced cardiac fibrosis (Figures 7H and S7F) at week 10 compared with WT controls. Finally, Doxo-induced OXPHOS subunit loss as measured by ATP5A1 immunofluorescence staining was significantly lessened in *Zbp1*<sup>-/-</sup>, *Sting*<sup>-/-</sup>, and *Ifnar*<sup>-/-</sup> mice (Figures 7I and S7G). Additional analysis of *Sting*<sup>-/-</sup> and *Ifnar*<sup>-/-</sup> cardiac lysates revealed higher levels of mtDNA and OXPHOS subunit expression after Doxo relative to WT controls (Figures S7H and S7I). In summary, our data reveal that the ZBP1-cGAS-STING axis governs cardiotoxic IFN-I signaling, which contributes significantly to the pathobiology of chemotherapy-related heart failure.

## DISCUSSION

ZBP1 has emerged as a central innate immune sensor of double-stranded nucleic acids in the left-handed Z-conformation,<sup>15–24,66</sup> and our study adds Z-form mtDNA to the growing list of ZBP1 ligands. Moreover, our work reveals that both genetic and pharmacologic triggers of mitochondrial genome instability can induce Z-form mtDNA *in cellulo*. Our data show that increased negative mtDNA supercoiling in cells lacking TFAM, TOP3A, and TOP1MT favors B to Z transition, leading to the accumulation of mitochondrial Z-DNA for detection by ZBP1. In contrast, we noted that ZBP1 is not required for sensing cytosolic B-form mtDNA liberated by IMM herniation. Therefore, the cytosolic DNA sensing machinery can discriminate between different mtDNA species, with the ZBP1-cGAS complex functioning as a specialized PRR for Z-form mtDNA.

Since overall Z-DNA intensity is lower in *Zbp1*<sup>-/-</sup> cells, it is likely that the Z $\alpha$  domains of ZBP1 stabilize Z-DNA and sustain detection by cGAS to augment IFN-I signaling. Moreover, the RHIM domains of ZBP1 are required for maximal cytosolic interactions with cGAS. ZBP1 forms homotypic interactions with the RHIM domain-containing proteins RIPK1 and RIPK3 to mediate NF- $\kappa$ B activation and innate immune signaling, as well as promote RIPK3-MLKL-dependent necroptosis.<sup>16,97–100</sup> However, MLKL-mediated cell death does not impact IFN-I responses in

cells experiencing mitochondrial genome instability. Consistent with immune signaling roles for RIPK1 and RIPK3, we found that both kinases are present in the ZBP1-cGAS complex. Moreover, the kinase activities of RIPK1 and RIPK3 promote STAT1<sup>S727</sup> phosphorylation in response to mitochondrial Z-DNA accumulation and are required to sustain the ZBP1-dependent IFN-I program. These findings are in line with a recent study showing that ZBP1 interacts with cGAS, RIPK1, and RIPK3 in *Casp8*<sup>-/-</sup>/*Mkl1*<sup>-/-</sup> MEFs and sustains STAT1 phosphorylation to Z-RNA.<sup>101</sup> Future studies should determine whether CASP8, FADD, and/or MLKL activities are inhibited in cells experiencing mitochondrial genome instability, which might favor ZBP1-cGAS-RIPK signaling to STAT1 while repressing ZBP1-dependent cell death signaling.

Doxo and other anthracycline chemotherapeutics are among the most effective and widely used antineoplastic drugs; however, their clinical application is limited by adverse cardiac side effects that occur in many patients.<sup>102</sup> Importantly, we have uncovered that Doxo induces mtDNA instability and Z-DNA accumulation in CMs and triggers a robust cardiac IFN-I signature that is dependent on ZBP1, STING, and IFNAR. Our data also reveal that CMs and infiltrating myeloid cells respond to Doxo by activating ZBP1-dependent IFN-I responses. Using a Doxo dosing protocol that closely resembles clinical timelines in late DIC, we observed that ZBP1 and other ISGs remain elevated in the heart for weeks after the last Doxo dose, suggestive of a self-propagating IFN-I cycle. Although cGAS and IFN-I signaling have recently been implicated in heart failure,<sup>40,43,103–105</sup> a role for ZBP1 has not been explored. Our findings indicate the presence of a ZBP1-dependent IFN-I signaling program in cardiac cells exposed to Doxo and highlight that ZBP1 is a key innate immune regulator of DIC and cardiomyopathy. Therefore, ZBP1 is a promising therapeutic target in chemotherapy-related cardiac dysfunction and perhaps other cardiovascular diseases where mtDNA instability promotes detrimental IFN-I and inflammatory responses.

## Limitations of the study

Although we observed increased Z-DNA staining in mitochondria and the cytoplasm after the induction of mitochondrial genome instability, we did not identify the precise Z-DNA sequences that are stabilized by ZBP1. Mitochondrial dysfunction and mtDNA replication defects can feed forward to cause nuclear genome instability,<sup>106,107</sup> and therefore, it is possible that Z-DNA derived from both mtDNA and nuclear DNA accumulate in our models. Second, although we find that mitochondrial genome instability upregulates ZBP1 and promotes ZBP1-cGAS interactions, both DNA sensors form basal complexes with RIPK1 and RIPK3. Our study neither elucidates the

(E and F) qRT-PCR analysis of ISGs (E) or natriuretic peptides *Nppa*, *Nppb*, and the *Myh6/7* expression ratio (F) in veh- and Doxo-treated WT, *Zbp1*<sup>-/-</sup>, *Sting*<sup>-/-</sup>, and *Ifnar*<sup>-/-</sup> cardiac lysates (n = 3 per genotype per treatment).

(G–I) Representative images of H&E staining (G), picrosirius red (P. Red) staining (H), and ATP5A1 and DAPI immunofluorescent staining (I) of the heart sections from veh-treated WT mice and 10-week post Doxo-treated WT, *Zbp1*<sup>-/-</sup>, *Sting*<sup>-/-</sup>, and *Ifnar*<sup>-/-</sup> mice. Arrows in (G) indicate significant cardiomyocyte vacuolization in Doxo-treated WT heart section. Statistical significance was determined using ANOVA and Dunnett (B) or Šídák (E and F) post hoc test. \*p < 0.05, \*\*p < 0.01, and \*\*\*p < 0.001. Error bars represent SEM.

See also Figure S7.

stoichiometry of these complexes nor identifies the molecular changes that license RIPK-dependent phosphorylation of STAT1 as opposed to MLKL. Finally, although mtDNA instability predominantly drives ZBP1-cGAS-RIPK-dependent IFN- $\lambda$  signaling *in vitro*, we cannot exclude a role for ZBP1-driven cell death in DIC *in vivo*.

## STAR★METHODS

Detailed methods are provided in the online version of this paper and include the following:

- **KEY RESOURCES TABLE**
- **RESOURCE AVAILABILITY**
  - Lead contact
  - Materials availability
  - Data and code availability
- **EXPERIMENTAL MODEL AND SUBJECT DETAILS**
  - Mouse husbandry and strains
  - Doxorubicin administration
  - Mouse melanoma induction, Doxorubicin, and adjuvant IFN $\alpha$  therapy
  - Cardiac cell isolation
  - Cell culture
- **METHOD DETAILS**
  - siRNA and DNA transfection
  - Southwestern blot
  - Cloning and retroviral transduction
  - Topologically constrained Z-DNA synthesis
  - Electrophoretic mobility shift assay (EMSA)
  - Protein expression and purification
  - cGAS activity assay
  - Co-immunoprecipitation
  - Subcellular fractionation, DNA isolation, and slot blotting
  - Quantitative PCR
  - Immunoblotting
  - Immunofluorescence microscopy
  - Flow cytometry
  - Echocardiography
  - Histology
  - Immunofluorescence staining in cardiac sections
  - RNA sequencing and bioinformatic analyses
- **QUANTIFICATION AND STATISTICAL ANALYSIS**

## SUPPLEMENTAL INFORMATION

Supplemental information can be found online at <https://doi.org/10.1016/j.cell.2023.05.039>.

## ACKNOWLEDGMENTS

We thank Dr. Ken Ishii and Dr. Bill Kaiser for providing *Zbp1*<sup>-/-</sup> mice and Ms. Robbie Moore for assistance with flow cytometry. This work was supported by NIH grants to A.P.W. (R01HL148153, R01AI155621, and R01CA193522), C.W.T. (R01HL145534), P.L. (R01AI145287), G.S.S. (R01AR069876 and R01CA216101), and J.W.U. (R21AI135709). Additional support was provided by NIH grant P30ES029067 and a Natural Sciences and Engineering Research Council of Canada grant to T.E.S. (NSERC—RGPIN-2016-04083). G.S.S. is the Audrey Geisel Chair in Biomedical Science.

Y. Lei was supported by an American Heart Association Predoctoral Fellowship (grant 825908). S.T.-O. was supported by a Ruth L. Kirschstein National Research Service Award (F31HL160141).

## AUTHOR CONTRIBUTIONS

Conceptualization, Y. Lei and A.P.W.; investigation, Y. Lei, J.J.V., Y.C., J.D.B., Y. Li, D.F., S.T.-O., K.B.R., J.D., A.M., B.W., O.N.B., S.D.Y., L.C.W., and A.P.W.; methodology, Y. Lei, J.J.V., Y.-F.C., J.D.B., M.S., C.W.T., M.W.B., L.C.W., G.S.S., T.E.S., J.W.U., P.L., and A.P.W.; writing, Y. Lei and A.P.W.; visualization, Y. Lei and A.P.W.; funding acquisition, Y. Lei, S.T.-O., C.W.T., L.C.W., G.S.S., T.E.S., J.W.U., P.L., and A.P.W. All authors read and approved the manuscript.

## DECLARATION OF INTERESTS

The authors declare no competing interests.

## INCLUSION AND DIVERSITY

We support inclusive, diverse, and equitable conduct of research.

Received: May 31, 2022

Revised: February 3, 2023

Accepted: May 26, 2023

Published: June 22, 2023

## REFERENCES

1. West, A.P., and Shadel, G.S. (2017). Mitochondrial DNA in innate immune responses and inflammatory pathology. *Nat. Rev. Immunol.* *17*, 363–375. <https://doi.org/10.1038/nri.2017.21>.
2. Riley, J.S., and Tait, S.W. (2020). Mitochondrial DNA in inflammation and immunity. *EMBO Rep.* *21*, e49799. <https://doi.org/10.15252/embr.201949799>.
3. Marchi, S., Guilbaud, E., Tait, S.W.G., Yamazaki, T., and Galluzzi, L. (2022). Mitochondrial control of inflammation. *Nat. Rev. Immunol.* *23*, 159–173. <https://doi.org/10.1038/s41577-022-00760-x>.
4. Chen, D., Tong, J., Yang, L., Wei, L., Stolz, D.B., Yu, J., Zhang, J., and Zhang, L. (2018). PUMA amplifies necroptosis signaling by activating cytosolic DNA sensors. *Proc. Natl. Acad. Sci. USA* *115*, 3930–3935. <https://doi.org/10.1073/pnas.1717190115>.
5. Szczesny, B., Marcatti, M., Ahmad, A., Montalbano, M., Brunyánszki, A., Bibli, S.I., Papapetropoulos, A., and Szabo, C. (2018). Mitochondrial DNA damage and subsequent activation of Z-DNA binding protein 1 links oxidative stress to inflammation in epithelial cells. *Sci. Rep.* *8*, 914. <https://doi.org/10.1038/s41598-018-19216-1>.
6. Saada, J., McAuley, R.J., Marcatti, M., Tang, T.Z., Motamedi, M., and Szczesny, B. (2022). Oxidative stress induces Z-DNA-binding protein 1-dependent activation of microglia via mtDNA released from retinal pigment epithelial cells. *J. Biol. Chem.* *298*, 101523. <https://doi.org/10.1016/j.jbc.2021.101523>.
7. Zhong, F., Liang, S., and Zhong, Z. (2019). Emerging role of mitochondrial DNA as a major driver of inflammation and disease progression. *Trends Immunol.* *40*, 1120–1133. <https://doi.org/10.1016/j.it.2019.10.008>.
8. Lei, Y., Guerra Martinez, C.G., Torres-Odio, S., Bell, S.L., Birdwell, C.E., Bryant, J.D., Tong, C.W., Watson, R.O., West, L.C., and West, A.P. (2021). Elevated type I interferon responses potentiate metabolic dysfunction, inflammation, and accelerated aging in mtDNA mutator mice. *Sci. Adv.* *7*, eabe7548. <https://doi.org/10.1126/sciadv.abe7548>.
9. Newman, L.E., and Shadel, G.S. (2023). Mitochondrial DNA Release in Innate Immune Signaling. *Annu. Rev. Biochem.* <https://doi.org/10.1146/annurev-biochem-032620-104401>.

10. Menger, K.E., Rodríguez-Luis, A., Chapman, J., and Nicholls, T.J. (2021). Controlling the topology of mammalian mitochondrial DNA. *Open Biol.* *11*, 210168. <https://doi.org/10.1098/rsob.210168>.
11. Carvalho, G., Repolês, B.M., Mendes, I., and Wanrooij, P.H. (2022). Mitochondrial DNA instability in mammalian cells. *Antioxid. Redox Signal.* *36*, 885–905. <https://doi.org/10.1089/ars.2021.0091>.
12. Pommier, Y., Nussenzweig, A., Takeda, S., and Austin, C. (2022). Human topoisomerases and their roles in genome stability and organization. *Nat. Rev. Mol. Cell Biol.* *23*, 407–427. <https://doi.org/10.1038/s41580-022-00452-3>.
13. Herbert, A. (2019). Z-DNA and Z-RNA in human disease. *Commun. Biol.* *2*, 7. <https://doi.org/10.1038/s42003-018-0237-x>.
14. Ravichandran, S., Subramani, V.K., and Kim, K.K. (2019). Z-DNA in the genome: from structure to disease. *Biophys. Rev.* *11*, 383–387. <https://doi.org/10.1007/s12551-019-00534-1>.
15. Maelfait, J., Liverpool, L., Bridgeman, A., Ragan, K.B., Upton, J.W., and Rehwinkel, J. (2017). Sensing of viral and endogenous RNA by ZBP1/DAI induces necroptosis. *EMBO J.* *36*, 2529–2543. <https://doi.org/10.15252/emboj.201796476>.
16. Jiao, H., Wachsmuth, L., Kumari, S., Schwarzer, R., Lin, J., Eren, R.O., Fisher, A., Lane, R., Young, G.R., Kassiotis, G., et al. (2020). Z-nucleic acid sensing triggers ZBP1-dependent necroptosis and inflammation. *Nature* *580*, 391–395. <https://doi.org/10.1038/s41586-020-2129-8>.
17. Jiao, H., Wachsmuth, L., Wolf, S., Lohmann, J., Nagata, M., Kaya, G.G., Oikonomou, N., Kondylis, V., Rogg, M., Diebold, M., et al. (2022). ADAR1 averts fatal type I interferon induction by ZBP1. *Nature* *607*, 776–783. <https://doi.org/10.1038/s41586-022-04878-9>.
18. Guo, H., Gilley, R.P., Fisher, A., Lane, R., Landsteiner, V.J., Ragan, K.B., Dovey, C.M., Carette, J.E., Upton, J.W., Mocarski, E.S., et al. (2018). Species-independent contribution of ZBP1/DAI/DLM-1-triggered necroptosis in host defense against HSV1. *Cell Death Dis.* *9*, 816. <https://doi.org/10.1038/s41419-018-0868-3>.
19. Kuriakose, T., Zheng, M., Neale, G., and Kanneganti, T.D. (2018). IRF1 is a transcriptional regulator of ZBP1 promoting NLRP3 inflammasome activation and cell death during influenza virus infection. *J. Immunol.* *200*, 1489–1495. <https://doi.org/10.4049/jimmunol.1701538>.
20. Upton, J.W., Kaiser, W.J., and Mocarski, E.S. (2012). DAI/ZBP1/DLM-1 complexes with RIP3 to mediate virus-induced programmed necrosis that is targeted by murine cytomegalovirus vIRA. *Cell Host Microbe* *11*, 290–297. <https://doi.org/10.1016/j.chom.2012.01.016>.
21. Zhang, T., Yin, C., Boyd, D.F., Quarato, G., Ingram, J.P., Shubina, M., Ragan, K.B., Ishizuka, T., Crawford, J.C., Tummers, B., et al. (2020). Influenza virus Z-RNAs induce ZBP1-mediated necroptosis. *Cell* *180*, 1115–1129.e13. <https://doi.org/10.1016/j.cell.2020.02.050>.
22. Hubbard, N.W., Ames, J.M., Maurano, M., Chu, L.H., Somfleth, K.Y., Gokhale, N.S., Werner, M., Snyder, J.M., Lichauco, K., Savan, R., et al. (2022). ADAR1 mutation causes ZBP1-dependent immunopathology. *Nature* *607*, 769–775. <https://doi.org/10.1038/s41586-022-04896-7>.
23. de Reuver, R., Verdonck, S., Dierick, E., Nemegeer, J., Hessmann, E., Ahmad, S., Jans, M., Blancke, G., Van Nieuwerburgh, F., Botzki, A., et al. (2022). ADAR1 prevents autoinflammation by suppressing spontaneous ZBP1 activation. *Nature* *607*, 784–789. <https://doi.org/10.1038/s41586-022-04974-w>.
24. Nassour, J., Aguiar, L.G., Correia, A., Schmidt, T.T., Mainz, L., Przetocka, S., Haggblom, C., Tadeppalle, N., Williams, A., Shokhirev, M.N., et al. (2023). Telomere-to-mitochondria signalling by ZBP1 mediates replicative crisis. *Nature* *614*, 767–773. <https://doi.org/10.1038/s41586-023-05710-8>.
25. Wallace, K.B., Sardão, V.A., and Oliveira, P.J. (2020). Mitochondrial determinants of doxorubicin-induced cardiomyopathy. *Circ. Res.* *126*, 926–941. <https://doi.org/10.1161/CIRCRESAHA.119.314681>.
26. Bloom, M.W., Hamo, C.E., Cardinale, D., Ky, B., Nohria, A., Baer, L., Skopicki, H., Lenihan, D.J., Gheorghiadu, M., Lyon, A.R., et al. (2016). Cancer therapy-related cardiac dysfunction and heart failure: Part 1: Definitions, Pathophysiology, Risk Factors, and Imaging. *Circ. Heart Fail.* *9*, e002661. <https://doi.org/10.1161/CIRCHEARTFAILURE.115.002661>.
27. Lipshultz, S.E., Cochran, T.R., Franco, V.I., and Miller, T.L. (2013). Treatment-related cardiotoxicity in survivors of childhood cancer. *Nat. Rev. Clin. Oncol.* *10*, 697–710. <https://doi.org/10.1038/nrclinonc.2013.195>.
28. Mehta, L.S., Watson, K.E., Barac, A., Beckie, T.M., Bittner, V., Cruz-Flores, S., Dent, S., Kondapalli, L., Ky, B., Okwuosa, T., et al. (2018). Cardiovascular disease and breast cancer: where these entities intersect: A scientific statement from the American Heart Association. *Circulation* *137*, e30–e66. <https://doi.org/10.1161/CIR.0000000000000556>.
29. Vejpongsa, P., and Yeh, E.T.H. (2014). Prevention of anthracycline-induced cardiotoxicity: challenges and opportunities. *J. Am. Coll. Cardiol.* *64*, 938–945. <https://doi.org/10.1016/j.jacc.2014.06.1167>.
30. Volkova, M., and Russell, R. (2011). Anthracycline cardiotoxicity: prevalence, pathogenesis and treatment. *Curr. Cardiol. Rev.* *7*, 214–220. <https://doi.org/10.2174/157340311799960645>.
31. Berthiaume, J.M., and Wallace, K.B. (2007). Adriamycin-induced oxidative mitochondrial cardiotoxicity. *Cell Biol. Toxicol.* *23*, 15–25. <https://doi.org/10.1007/s10565-006-0140-y>.
32. Zhou, S., Palmeira, C.M., and Wallace, K.B. (2001). Doxorubicin-induced persistent oxidative stress to cardiac myocytes. *Toxicol. Lett.* *121*, 151–157. [https://doi.org/10.1016/s0378-4274\(01\)00329-0](https://doi.org/10.1016/s0378-4274(01)00329-0).
33. Yen, H.C., Oberley, T.D., Gairola, C.G., Szveda, L.I., and St Clair, D.K. (1999). Manganese superoxide dismutase protects mitochondrial complex I against adriamycin-induced cardiomyopathy in transgenic mice. *Arch. Biochem. Biophys.* *362*, 59–66. <https://doi.org/10.1006/abbi.1998.1011>.
34. Carvalho, F.S., Burgeiro, A., Garcia, R., Moreno, A.J., Carvalho, R.A., and Oliveira, P.J. (2014). Doxorubicin-induced cardiotoxicity: from bioenergetic failure and cell death to cardiomyopathy. *Med. Res. Rev.* *34*, 106–135. <https://doi.org/10.1002/med.21280>.
35. Serrano, J., Palmeira, C.M., Kuehl, D.W., and Wallace, K.B. (1999). Cardiospecific and cumulative oxidation of mitochondrial DNA following subchronic doxorubicin administration. *Biochim. Biophys. Acta* *1411*, 201–205. [https://doi.org/10.1016/s0005-2728\(99\)00011-0](https://doi.org/10.1016/s0005-2728(99)00011-0).
36. Khiati, S., Dalla Rosa, I., Sourbier, C., Ma, X., Rao, V.A., Neckers, L.M., Zhang, H., and Pommier, Y. (2014). Mitochondrial topoisomerase I (Top1mt) is a novel limiting factor of doxorubicin cardiotoxicity. *Clin. Cancer Res.* *20*, 4873–4881. <https://doi.org/10.1158/1078-0432.CCR-13-3373>.
37. Hangas, A., Aasumets, K., Kekäläinen, N.J., Paloheinä, M., Pohjoismäki, J.L., Gerhold, J.M., and Goffart, S. (2018). Ciprofloxacin impairs mitochondrial DNA replication initiation through inhibition of topoisomerase 2. *Nucleic Acids Res.* *46*, 9625–9636. <https://doi.org/10.1093/nar/gky793>.
38. Wu, Z., Oeck, S., West, A.P., Mangalaha, K.C., Sainz, A.G., Newman, L.E., Zhang, X.O., Wu, L., Yan, Q., Bosenberg, M., et al. (2019). Mitochondrial DNA stress signalling protects the nuclear genome. *Nat. Metab.* *1*, 1209–1218. <https://doi.org/10.1038/s42255-019-0150-8>.
39. Zhang, Z., Meng, P., Han, Y., Shen, C., Li, B., Hakim, M.A., Zhang, X., Lu, Q., Rong, M., and Lai, R. (2015). Mitochondrial DNA-LL-37 complex promotes atherosclerosis by escaping from autophagic recognition. *Immunity* *43*, 1137–1147. <https://doi.org/10.1016/j.immuni.2015.10.018>.
40. Oka, T., Hikoso, S., Yamaguchi, O., Taneike, M., Takeda, T., Tamai, T., Oyabu, J., Murakawa, T., Nakayama, H., Nishida, K., et al. (2012). Mitochondrial DNA that escapes from autophagy causes inflammation and heart failure. *Nature* *485*, 251–255. <https://doi.org/10.1038/nature10992>.
41. Nakayama, H., and Otsu, K. (2018). Mitochondrial DNA as an inflammatory mediator in cardiovascular diseases. *Biochem. J.* *475*, 839–852. <https://doi.org/10.1042/BCJ20170714>.
42. Cao, D.J., Schiattarella, G.G., Villalobos, E., Jiang, N., May, H.I., Li, T., Chen, Z.J., Gillette, T.G., and Hill, J.A. (2018). Cytosolic DNA sensing

- promotes macrophage transformation and governs myocardial ischemic injury. *Circulation* 137, 2613–2634. <https://doi.org/10.1161/CIRCULATIONAHA.117.031046>.
43. King, K.R., Aguirre, A.D., Ye, Y.-X., Sun, Y., Roh, J.D., Ng, R.P., Kohler, R.H., Arlauckas, S.P., Iwamoto, Y., Savol, A., et al. (2017). IRF3 and type I interferons fuel a fatal response to myocardial infarction. *Nat. Med.* 23, 1481–1487. <https://doi.org/10.1038/nm.4428>.
  44. West, A.P., Khoury-Hanold, W., Staron, M., Tal, M.C., Pineda, C.M., Lang, S.M., Bestwick, M., Duguay, B.A., Raimundo, N., MacDuff, D.A., et al. (2015). Mitochondrial DNA stress primes the antiviral innate immune response. *Nature* 520, 553–557. <https://doi.org/10.1038/nature14156>.
  45. Pohjoismäki, J.L.O., Wanrooij, S., Hyvärinen, A.K., Goffart, S., Holt, I.J., Spelbrink, J.N., and Jacobs, H.T. (2006). Alterations to the expression level of mitochondrial transcription factor A, TFAM, modify the mode of mitochondrial DNA replication in cultured human cells. *Nucleic Acids Res.* 34, 5815–5828. <https://doi.org/10.1093/nar/gkl703>.
  46. Nicholls, T.J., Nadalutti, C.A., Motori, E., Sommerville, E.W., Gorman, G.S., Basu, S., Hoberg, E., Turnbull, D.M., Chinnery, P.F., Larsson, N.-G., et al. (2018). Topoisomerase 3 $\alpha$  Is Required for decatenation and Segregation of Human mtDNA. *Mol. Cell* 69, 9–23.e6. <https://doi.org/10.1016/j.molcel.2017.11.033>.
  47. Menger, K.E., Chapman, J., Díaz-Maldonado, H., Khazeeem, M.M., Deen, D., Erdinc, D., Casement, J.W., Di Leo, V., Pyle, A., Rodríguez-Luis, A., et al. (2022). Two type I topoisomerases maintain DNA topology in human mitochondria. *Nucleic Acids Res.* 50, 11154–11174. <https://doi.org/10.1093/nar/gkac857>.
  48. Zhang, H., Zhang, Y.-W., Yasukawa, T., Dalla Rosa, I., Khiati, S., and Pommier, Y. (2014). Increased negative supercoiling of mtDNA in TOP1mt knockout mice and presence of topoisomerases II $\alpha$  and II $\beta$  in vertebrate mitochondria. *Nucleic Acids Res.* 42, 7259–7267. <https://doi.org/10.1093/nar/gku384>.
  49. Al Khatib, I.A., Deng, J., Symes, A., Kerr, M., Zhang, H., Huang, S.N., Pommier, Y., Khan, A., and Shutt, T.E. (2022). Functional characterization of two variants of mitochondrial topoisomerase TOP1MT that impact regulation of the mitochondrial genome. *J. Biol. Chem.* 298, 102420. <https://doi.org/10.1016/j.jbc.2022.102420>.
  50. Ishii, K.J., Kawagoe, T., Koyama, S., Matsui, K., Kumar, H., Kawai, T., Uematsu, S., Takeuchi, O., Takeshita, F., Coban, C., et al. (2008). TANK-binding kinase-1 delineates innate and adaptive immune responses to DNA vaccines. *Nature* 451, 725–729. <https://doi.org/10.1038/nature06537>.
  51. Wang, Z., Choi, M.K., Ban, T., Yanai, H., Negishi, H., Lu, Y., Tamura, T., Takaoka, A., Nishikura, K., and Taniguchi, T. (2008). Regulation of innate immune responses by DAI (DLM-1/ZBP1) and other DNA-sensing molecules. *Proc. Natl. Acad. Sci. USA* 105, 5477–5482. <https://doi.org/10.1073/pnas.0801295105>.
  52. Rongvaux, A., Jackson, R., Harman, C.C.D., Li, T., West, A.P., de Zoete, M.R., Wu, Y., Yordy, B., Lakhani, S.A., Kuan, C.-Y., et al. (2014). Apoptotic caspases prevent the induction of type I interferons by mitochondrial DNA. *Cell* 159, 1563–1577. <https://doi.org/10.1016/j.cell.2014.11.037>.
  53. Riley, J.S., Quarato, G., Cloix, C., Lopez, J., O'Prey, J., Pearson, M., Chapman, J., Sesaki, H., Carlin, L.M., Passos, J.F., et al. (2018). Mitochondrial inner membrane permeabilisation enables mtDNA release during apoptosis. *EMBO J.* 37, e99238. <https://doi.org/10.15252/embj.201899238>.
  54. McArthur, K., Whitehead, L.W., Heddleston, J.M., Li, L., Padman, B.S., Oorschot, V., Geoghegan, N.D., Chappaz, S., Davidson, S., San Chin, H.S., et al. (2018). BAK/BAX macropores facilitate mitochondrial herniation and mtDNA efflux during apoptosis. *Science* 359, eaao6047. <https://doi.org/10.1126/science.aao6047>.
  55. Zhang, Y., Cui, Y., An, R., Liang, X., Li, Q., Wang, H., Wang, H., Fan, Y., Dong, P., Li, J., et al. (2019). Topologically constrained formation of stable Z-DNA from normal sequence under physiological conditions. *J. Am. Chem. Soc.* 141, 7758–7764. <https://doi.org/10.1021/jacs.8b13855>.
  56. Möller, A., Gabriels, J.E., Lafer, E.M., Nordheim, A., Rich, A., and Stollar, B.D. (1982). Monoclonal antibodies recognize different parts of Z-DNA. *J. Biol. Chem.* 257, 12081–12085.
  57. Buzzo, J.R., Devaraj, A., Gloag, E.S., Jurcisek, J.A., Robledo-Avila, F., Kesler, T., Wilbanks, K., Mashburn-Warren, L., Balu, S., Wickham, J., et al. (2021). Z-form extracellular DNA is a structural component of the bacterial biofilm matrix. *Cell* 184, 5740–5758.e17. <https://doi.org/10.1016/j.cell.2021.10.010>.
  58. Schwartz, T., Behlke, J., Lowenhaupt, K., Heinemann, U., and Rich, A. (2001). Structure of the DLM-1–Z-DNA complex reveals a conserved family of Z-DNA-binding proteins. *Nat. Struct. Biol.* 8, 761–765. <https://doi.org/10.1038/nsb0901-761>.
  59. Deigendesch, N., Koch-Nolte, F., and Rothenburg, S. (2006). ZBP1 subcellular localization and association with stress granules is controlled by its Z-DNA binding domains. *Nucleic Acids Res.* 34, 5007–5020. <https://doi.org/10.1093/nar/gkl575>.
  60. Ha, S.C., Van Quyen, D., Hwang, H.-Y., Oh, D.-B., Brown, B.A., Lee, S.M., Park, H.-J., Ahn, J.-H., Kim, K.K., and Kim, Y.-G. (2006). Biochemical characterization and preliminary X-ray crystallographic study of the domains of human ZBP1 bound to left-handed Z-DNA. *Biochim. Biophys. Acta* 1764, 320–323. <https://doi.org/10.1016/j.bbapap.2005.12.012>.
  61. Ha, S.C., Kim, D., Hwang, H.-Y., Rich, A., Kim, Y.-G., and Kim, K.K. (2008). The crystal structure of the second Z-DNA binding domain of human DAI (ZBP1) in complex with Z-DNA reveals an unusual binding mode to Z-DNA. *Proc. Natl. Acad. Sci. USA* 105, 20671–20676. <https://doi.org/10.1073/pnas.0810463106>.
  62. Thomas, T.J., Seibold, J.R., Adams, L.E., and Hess, E.V. (1993). Hydralazine induces Z-DNA conformation in a polynucleotide and elicits anti(Z-DNA) antibodies in treated patients. *Biochem. J.* 294, 419–425.
  63. Timlin, H., Wu, M., Crespo-Bosque, M., Geetha, D., Ingolia, A., Haque, U., Towns, M.C., and Grader-Beck, T. (2019). Clinical characteristics of hydralazine-induced lupus. *Cureus* 11, e4996. <https://doi.org/10.7759/cureus.4996>.
  64. Zhao, B., Xu, P., Rowlett, C.M., Jing, T., Shinde, O., Lei, Y., West, A.P., Liu, W.R., and Li, P. (2020). The molecular basis of tight nuclear tethering and inactivation of cGAS. *Nature* 587, 673–677. <https://doi.org/10.1038/s41586-020-2749-z>.
  65. Volkman, H.E., Cambier, S., Gray, E.E., and Stetson, D.B. (2019). Tight nuclear tethering of cGAS is essential for preventing autoreactivity. *eLife* 8, e47491. <https://doi.org/10.7554/eLife.47491>.
  66. Zhang, T., Yin, C., Fedorov, A., Qiao, L., Bao, H., Beknazarov, N., Wang, S., Gautam, A., Williams, R.M., Crawford, J.C., et al. (2022). ADAR1 masks the cancer immunotherapeutic promise of ZBP1-driven necroptosis. *Nature* 606, 594–602. <https://doi.org/10.1038/s41586-022-04753-7>.
  67. Ma, Y., Wang, X., Luo, W., Xiao, J., Song, X., Wang, Y., Shuai, H., Ren, Z., and Wang, Y. (2021). Roles of emerging RNA-binding activity of cGAS in innate antiviral response. *Front. Immunol.* 12, 741599. <https://doi.org/10.3389/fimmu.2021.741599>.
  68. Wang, D., Zhao, H., Shen, Y., and Chen, Q. (2022). A variety of nucleic acid species are sensed by cGAS, implications for its diverse functions. *Front. Immunol.* 13, 826880. <https://doi.org/10.3389/fimmu.2022.826880>.
  69. Slavik, K.M., Morehouse, B.R., Ragucci, A.E., Zhou, W., Ai, X., Chen, Y., Li, L., Wei, Z., Bähre, H., König, M., et al. (2021). cGAS-like receptors sense RNA and control 3'2'-cGAMP signalling in Drosophila. *Nature* 597, 109–113. <https://doi.org/10.1038/s41586-021-03743-5>.
  70. Kesavardhana, S., and Kanneganti, T.-D. (2020). ZBP1: a STARGATE to decode the biology of Z-nucleic acids in disease. *J. Exp. Med.* 217, e20200885. <https://doi.org/10.1084/jem.20200885>.
  71. Varinou, L., Ramsauer, K., Karaghissoff, M., Kolbe, T., Pfeffer, K., Müller, M., and Decker, T. (2003). Phosphorylation of the Stat1 transactivation

- domain is required for full-fledged IFN- $\gamma$ -dependent innate immunity. *Immunity* 19, 793–802. [https://doi.org/10.1016/S1074-7613\(03\)00322-4](https://doi.org/10.1016/S1074-7613(03)00322-4).
72. Kovarik, P., Stoiber, D., Eyers, P.A., Menghini, R., Neininger, A., Gaestel, M., Cohen, P., and Decker, T. (1999). Stress-induced phosphorylation of STAT1 at Ser727 requires p38 mitogen-activated protein kinase whereas IFN- $\gamma$  uses a different signaling pathway. *Proc. Natl. Acad. Sci. USA* 96, 13956–13961. <https://doi.org/10.1073/pnas.96.24.13956>.
  73. Staab, J., Herrmann-Lingen, C., and Meyer, T. (2013). CDK8 as the STAT1 serine 727 kinase? *JAK-STAT* 2, e24275. <https://doi.org/10.4161/jkst.24275>.
  74. Shutinoski, B., Alturki, N.A., Rijal, D., Bertin, J., Gough, P.J., Schlossmacher, M.G., and Sad, S. (2016). K45A mutation of RIPK1 results in poor necroptosis and cytokine signaling in macrophages, which impacts inflammatory responses in vivo. *Cell Death Differ.* 23, 1628–1637. <https://doi.org/10.1038/cdd.2016.51>.
  75. Sridharan, H., Ragan, K.B., Guo, H., Gilley, R.P., Landsteiner, V.J., Kaiser, W.J., and Upton, J.W. (2017). Murine cytomegalovirus IE3-dependent transcription is required for DAI/ZBP1-mediated necroptosis. *EMBO Rep.* 18, 1429–1441. <https://doi.org/10.15252/embr.201743947>.
  76. Ingram, J.P., Thapa, R.J., Fisher, A., Tummers, B., Zhang, T., Yin, C., Rodriguez, D.A., Guo, H., Lane, R., Williams, R., et al. (2019). ZBP1/DAI drives RIPK3-mediated cell death induced by IFNs in the absence of RIPK1. *J. Immunol.* 203, 1348–1355. <https://doi.org/10.4049/jimmunol.1900216>.
  77. Devos, M., Tanghe, G., Gilbert, B., Dierick, E., Verheirstraeten, M., Nemegeer, J., de Reuver, R., Lefebvre, S., De Munck, J., Rehwinkel, J., et al. (2020). Sensing of endogenous nucleic acids by ZBP1 induces keratinocyte necroptosis and skin inflammation. *J. Exp. Med.* 217, e20191913. <https://doi.org/10.1084/jem.20191913>.
  78. Baik, J.Y., Liu, Z., Jiao, D., Kwon, H.-J., Yan, J., Kadigamuwa, C., Choe, M., Lake, R., Kruhlak, M., Tandon, M., et al. (2021). ZBP1 not RIPK1 mediates tumor necroptosis in breast cancer. *Nat. Commun.* 12, 2666. <https://doi.org/10.1038/s41467-021-23004-3>.
  79. Yang, Y., Wu, M., Cao, D., Yang, C., Jin, J., Wu, L., Hong, X., Li, W., Lu, L., Li, J., et al. (2021). ZBP1-MLKL necroptotic signaling potentiates radiation-induced antitumor immunity via intratumoral STING pathway activation. *Sci. Adv.* 7, eabf6290. <https://doi.org/10.1126/sciadv.abf6290>.
  80. Zhang, S., Liu, X., Bawa-Khalife, T., Lu, L.-S., Lyu, Y.L., Liu, L.F., and Yeh, E.T.H. (2012). Identification of the molecular basis of doxorubicin-induced cardiotoxicity. *Nat. Med.* 18, 1639–1642. <https://doi.org/10.1038/nm.2919>.
  81. Burrige, P.W., Li, Y.F., Matsa, E., Wu, H., Ong, S.-G., Sharma, A., Holmström, A., Chang, A.C., Coronado, M.J., Ebert, A.D., et al. (2016). Human induced pluripotent stem cell-derived cardiomyocytes recapitulate the predilection of breast cancer patients to doxorubicin-induced cardiotoxicity. *Nat. Med.* 22, 547–556. <https://doi.org/10.1038/nm.4087>.
  82. Kuwata, A., Ohashi, M., Sugiyama, M., Ueda, R., and Dohi, Y. (2002). A case of reversible dilated cardiomyopathy after alpha-interferon therapy in a patient with renal cell carcinoma. *Am. J. Med. Sci.* 324, 331–334. <https://doi.org/10.1097/00000441-200212000-00008>.
  83. Zimmerman, S., Adkins, D., Graham, M., Petruska, P., Bowers, C., Vrahnos, D., and Spitzer, G. (1994). Irreversible, severe congestive cardiomyopathy occurring in association with interferon alpha therapy. *Cancer Biother.* 9, 291–299. <https://doi.org/10.1089/cbr.1994.9.291>.
  84. Angulo, M.P., Navajas, A., Galdeano, J.M., Astigarraga, I., and Fernández-Teijeiro, A. (1999). Reversible cardiomyopathy secondary to alpha-interferon in an infant. *Pediatr. Cardiol.* 20, 293–294. <https://doi.org/10.1007/s002469900467>.
  85. Khakoo, A.Y., Halushka, M.K., Rame, J.E., Rodriguez, E.R., Kasper, E.K., and Judge, D.P. (2005). Reversible cardiomyopathy caused by administration of interferon alpha. *Nat. Clin. Pract. Cardiovasc. Med.* 2, 53–57. <https://doi.org/10.1038/npcardio0069>.
  86. Benjamini, O., Kimhi, O., and Lishner, M. (2007). Severe pleuropericarditis and cardiomyopathy induced by high dose interferon alpha-2b. *Isr. Med. Assoc. J.* 9, 486–487.
  87. Zhao, W., Ji, F., Yu, S., Li, Z., and Deng, H. (2014). Dilated cardiomyopathy and hypothyroidism associated with pegylated interferon and ribavirin treatment for chronic hepatitis C: case report and literature review. *Braz. J. Infect. Dis.* 18, 110–113. <https://doi.org/10.1016/j.bjid.2013.05.014>.
  88. Ackers-Johnson, M., Li, P.Y., Holmes, A.P., O'Brien, S.-M., Pavlovic, D., and Foo, R.S. (2016). A simplified, Langendorff-free method for concomitant isolation of viable cardiac myocytes and nonmyocytes from the adult mouse heart. *Circ. Res.* 119, 909–920. <https://doi.org/10.1161/CIRCRESAHA.116.309202>.
  89. Feng, J., Li, Y., and Nie, Y. (2022). Methods of mouse cardiomyocyte isolation from postnatal heart. *J. Mol. Cell. Cardiol.* 168, 35–43. <https://doi.org/10.1016/j.yjmcc.2022.04.007>.
  90. Uccellini, M.B., and García-Sastre, A. (2018). ISRE-reporter mouse reveals high basal and induced Type I IFN responses in inflammatory monocytes. *Cell Rep.* 25, 2784–2796.e3. <https://doi.org/10.1016/j.celrep.2018.11.030>.
  91. Pinto, A.R., Illykh, A., Ivey, M.J., Kuwabara, J.T., D'antoni, M.L., Debuque, R., Chandran, A., Wang, L., Arora, K., Rosenthal, N.A., et al. (2016). Revisiting cardiac cellular composition. *Circ. Res.* 118, 400–409. <https://doi.org/10.1161/CIRCRESAHA.115.307778>.
  92. Muller, W.A. (2013). Getting leukocytes to the site of inflammation. *Vet. Pathol.* 50, 7–22. <https://doi.org/10.1177/0300985812469883>.
  93. Woodfin, A., Voisin, M.-B., and Nourshargh, S. (2007). PECAM-1: A multifunctional molecule in inflammation and vascular biology. *Arterioscler. Thromb. Vasc. Biol.* 27, 2514–2523. <https://doi.org/10.1161/ATVBAHA.107.151456>.
  94. Lafuse, W.P., Wozniak, D.J., and Rajaram, M.V.S. (2020). Role of cardiac macrophages on cardiac inflammation, fibrosis and tissue repair. *Cells* 10, 51. <https://doi.org/10.3390/cells10010051>.
  95. Dankort, D., Curley, D.P., Cartlidge, R.A., Nelson, B., Karnezis, A.N., Damsky, W.E., You, M.J., DePinho, R.A., McMahon, M., and Bosenberg, M. (2009). BRAFV600E cooperates with Pten silencing to elicit metastatic melanoma. *Nat. Genet.* 41, 544–552. <https://doi.org/10.1038/ng.356>.
  96. Damsky, W.E., Curley, D.P., Santhanakrishnan, M., Rosenbaum, L.E., Platt, J.T., Gould Rothberg, B.E., Taketo, M.M., Dankort, D., Rimm, D.L., McMahon, M., et al. (2011).  $\beta$ -catenin signaling controls metastasis in Braf-activated Pten-deficient melanomas. *Cancer Cell* 20, 741–754. <https://doi.org/10.1016/j.ccr.2011.10.030>.
  97. Kaiser, W.J., Upton, J.W., and Mocarski, E.S. (2008). Receptor-interacting protein homotypic interaction motif-dependent control of NF- $\kappa$ B activation via the DNA-dependent activator of IFN regulatory factors 1. *J. Immunol.* 181, 6427–6434. <https://doi.org/10.4049/jimmunol.181.9.6427>.
  98. Kuriakose, T., and Kanneganti, T.D. (2018). ZBP1: innate sensor regulating cell death and inflammation. *Trends Immunol.* 39, 123–134. <https://doi.org/10.1016/j.it.2017.11.002>.
  99. Daniels, B.P., Kofman, S.B., Smith, J.R., Norris, G.T., Snyder, A.G., Kolb, J.P., Gao, X., Locasale, J.W., Martinez, J., Gale, M., et al. (2019). The nucleotide sensor ZBP1 and kinase RIPK3 induce the enzyme IRG1 to promote an antiviral metabolic state in neurons. *Immunity* 50, 64–76.e4. <https://doi.org/10.1016/j.immuni.2018.11.017>.
  100. Peng, R., Wang, C.K., Wang-Kan, X., Idorn, M., Kjaer, M., Zhou, F.Y., Füll, B.K., Timmermann, F., Orozco, S.L., McCarthy, J., et al. (2022). Human ZBP1 induces cell death-independent inflammatory signaling via RIPK3 and RIPK1. *EMBO Rep.* 23, e55839. <https://doi.org/10.15252/embr.202255839>.
  101. Rodriguez, D.A., Quarato, G., Liedmann, S., Tummers, B., Zhang, T., Guy, C., Crawford, J.C., Palacios, G., Pelletier, S., Kalkavan, H., et al. (2022). Caspase-8 and FADD prevent spontaneous ZBP1 expression

- and necroptosis. *Proc. Natl. Acad. Sci. USA* 119, e2207240119. <https://doi.org/10.1073/pnas.2207240119>.
102. Henriksen, P.A. (2018). Anthracycline cardiotoxicity: an update on mechanisms, monitoring and prevention. *Heart* 104, 971–977. <https://doi.org/10.1136/heartjnl-2017-312103>.
  103. Chen, H.-J., Tas, S.W., and de Winther, M.P.J. (2020). Type-I interferons in atherosclerosis. *J. Exp. Med.* 217, e20190459. <https://doi.org/10.1084/jem.20190459>.
  104. Shamseddine, A., Patel, S.H., Chavez, V., Moore, Z.R., Adnan, M., Di Bona, M., Li, J., Dang, C.T., Ramanathan, L.V., Oeffinger, K.C., et al. (2023). Innate immune signaling drives late cardiac toxicity following DNA-damaging cancer therapies. *J. Exp. Med.* 220, e20220809. <https://doi.org/10.1084/jem.20220809>.
  105. Xiao, Z., Yu, Z., Chen, C., Chen, R., and Su, Y. (2023). GAS-STING signaling plays an essential pathogenetic role in doxorubicin-induced cardiotoxicity. *BMC Pharmacol. Toxicol.* 24, 19. <https://doi.org/10.1186/s40360-022-00631-0>.
  106. Veatch, J.R., McMurray, M.A., Nelson, Z.W., and Gottschling, D.E. (2009). Mitochondrial dysfunction leads to nuclear genome instability: A link through iron-sulfur clusters. *Cell* 137, 1247–1258. <https://doi.org/10.1016/j.cell.2009.04.014>.
  107. Hämäläinen, R.H., Landoni, J.C., Ahlqvist, K.J., Goffart, S., Ryytty, S., Rahman, M.O., Brilhante, V., Icaý, K., Hautaniemi, S., Wang, L., et al. (2019). Defects in mtDNA replication challenge nuclear genome stability through nucleotide depletion and provide a unifying mechanism for mouse progerias. *Nat. Metab.* 1, 958–965. <https://doi.org/10.1038/s42255-019-0120-1>.
  108. Terenzi, F., White, C., Pal, S., Williams, B.R.G., and Sen, G.C. (2007). Tissue-specific and inducer-specific differential induction of ISG56 and ISG54 in mice. *J. Virol.* 81, 8656–8665. <https://doi.org/10.1128/JVI.00322-07>.
  109. Fensterl, V., White, C.L., Yamashita, M., and Sen, G.C. (2008). Novel characteristics of the function and induction of murine p56 family proteins. *J. Virol.* 82, 11045–11053. <https://doi.org/10.1128/JVI.01593-08>.
  110. Subramanian, A., Tamayo, P., Mootha, V.K., Mukherjee, S., Ebert, B.L., Gillette, M.A., Paulovich, A., Pomeroy, S.L., Golub, T.R., Lander, E.S., et al. (2005). Gene set enrichment analysis: A knowledge-based approach for interpreting genome-wide expression profiles. *Proc. Natl. Acad. Sci. USA* 102, 15545–15550. <https://doi.org/10.1073/pnas.0506580102>.
  111. Mootha, V.K., Lindgren, C.M., Eriksson, K.-F., Subramanian, A., Sihag, S., Lehar, J., Puigserver, P., Carlsson, E., Ridderstråle, M., Laurila, E., et al. (2003). PGC-1 $\alpha$ -responsive genes involved in oxidative phosphorylation are coordinately downregulated in human diabetes. *Nat. Genet.* 34, 267–273. <https://doi.org/10.1038/ng1180>.
  112. Southern, E. (2006). Southern blotting. *Nat. Protoc.* 1, 518–525. <https://doi.org/10.1038/nprot.2006.73>.
  113. Bryant, J.D., Lei, Y., VanPortfliet, J.J., Winters, A.D., and West, A.P. (2022). Assessing mitochondrial DNA release into the cytosol and subsequent activation of innate immune-related pathways in mammalian cells. *Curr. Protoc.* 2, e372. <https://doi.org/10.1002/cpz1.372>.
  114. Bankhead, P., Loughrey, M.B., Fernández, J.A., Dombrowski, Y., McArt, D.G., Dunne, P.D., McQuaid, S., Gray, R.T., Murray, L.J., Coleman, H.G., et al. (2017). QuPath: open source software for digital pathology image analysis. *Sci. Rep.* 7, 16878. <https://doi.org/10.1038/s41598-017-17204-5>.
  115. Clarke, D.J.B., Jeon, M., Stein, D.J., Moiseyev, N., Kropiwnicki, E., Dai, C., Xie, Z., Wojciechowicz, M.L., Litz, S., Hom, J., et al. (2021). Apytters: turning jupyter Notebooks into data-driven web apps. *Patterns* 2, 100213. <https://doi.org/10.1016/j.patter.2021.100213>.
  116. Chen, E.Y., Tan, C.M., Kou, Y., Duan, Q., Wang, Z., Meirelles, G.V., Clark, N.R., and Ma'ayan, A. (2013). Enrichr: interactive and collaborative HTML5 gene list enrichment analysis tool. *BMC Bioinformatics* 14, 128. <https://doi.org/10.1186/1471-2105-14-128>.
  117. Kuleshov, M.V., Jones, M.R., Rouillard, A.D., Fernandez, N.F., Duan, Q., Wang, Z., Koplev, S., Jenkins, S.L., Jagodnik, K.M., Lachmann, A., et al. (2016). Enrichr: a comprehensive gene set enrichment analysis web server 2016 update. *Nucleic Acids Res.* 44, W90–W97. <https://doi.org/10.1093/nar/gkw377>.
  118. Xie, Z., Bailey, A., Kuleshov, M.V., Clarke, D.J.B., Evangelista, J.E., Jenkins, S.L., Lachmann, A., Wojciechowicz, M.L., Kropiwnicki, E., Jagodnik, K.M., et al. (2021). Gene set knowledge discovery with Enrichr. *Curr. Protoc.* 1, e90. <https://doi.org/10.1002/cpz1.90>.
  119. Ge, S.X., Jung, D., and Yao, R. (2020). ShinyGO: a graphical gene-set enrichment tool for animals and plants. *Bioinformatics* 36, 2628–2629. <https://doi.org/10.1093/bioinformatics/btz931>.

STAR★METHODS

KEY RESOURCES TABLE

REAGENT or RESOURCE	SOURCE	IDENTIFIER
<b>Antibodies</b>		
IFIT1	Ganes Sen, Cleveland Clinic <sup>108</sup>	N/A
IFIT3	Ganes Sen, Cleveland Clinic <sup>109</sup>	N/A
cGAS	Cell Signaling Technology	Cat# 31659, RRID: AB_2799008
cGAS	Cell Signaling Technology	Cat# 15102, RRID: AB_2732795
IRF9	Cell Signaling Technology	Cat# 28845, RRID: AB_2798964
STAT1	Cell Signaling Technology	Cat# 9172, RRID: AB_2198300
p-STAT1 (Tyr701)	Cell Signaling Technology	Cat# 7649, RRID: AB_10950970
p-STAT1 (Ser727)	Cell Signaling Technology	Cat# 9177, RRID: AB_2197983
TBK1	Cell Signaling Technology	Cat# 3504, RRID: AB_2255663
p-TBK1	Cell Signaling Technology	Cat# 5483, RRID: AB_10693472
STAT2	Cell Signaling Technology	Cat# 72604, RRID: AB_2799824
CASP8	Cell Signaling Technology	Cat# 4790, RRID: AB_10545768
RIPK3	Cell Signaling Technology	Cat# 95702, RRID: AB_2721823
MLKL	Cell Signaling Technology	Cat# 37705, RRID: AB_2799118
GAPDH	Proteintech	Cat# 60004-1-Ig, RRID: AB_2107436
Histone H3	Proteintech	Cat# 17168-1-AP, RRID: AB_2716755
LMNB1	Proteintech	Cat# 66095-1-Ig, RRID: AB_11232208
HA	Proteintech	Cat# 51064-2-AP, RRID: AB_11042321
TFAM	Proteintech	Cat# 22586-1-AP, RRID: AB_11182588
IFIT2	Proteintech	Cat# 12604-1-AP, RRID: AB_2864734
IFITM1	Proteintech	Cat# 60074-1-AP, RRID: AB_2940768
CANX	Proteintech	Cat# 10427-2-AP, RRID: AB_2069033
TFAM	Millipore	Cat# ABE483, RRID: AB_2940769
DNA	Millipore	Cat# CBL186, RRID: AB_11213573
TOMM20	Millipore	Cat# MABT166, RRID: AB_2890986
FLAG	Millipore	Cat# F1804, RRID: AB_262044
OXPPOS	Abcam	Cat# ab110413, RRID: AB_2629281
PDH	Abcam	Cat# ab110333, RRID: AB_10862029
RIPK1	BD Biosciences	Cat# 610458, RRID: AB_397831
BrdU	BD Biosciences	Cat# 555627, RRID: AB_395993
ZBP1	Adipogen	Cat# AG-20B-0010, RRID: AB_2490191
HSP60	Santa Cruz Biotechnology	Cat# sc-1052, RRID: AB_631683
Z-DNA	Absolute	Cat# Ab00783-23.0, RRID: AB_2820286
Z-DNA	Capralogics	Cat# P00008, RRID: AB_2940770
MT-CO1	ThermoFisher Scientific	Cat# 459600, RRID: AB_2532240
NDUFA9	ThermoFisher Scientific	Cat# 459100, RRID: AB_2532223
NDUFS3	ThermoFisher Scientific	Cat# 459130, RRID: AB_2532226
CD45	BioLegend	Cat# 103124, RRID: AB_493533
CD11b	BioLegend	Cat# 101226, RRID: AB_830642
CD31	BioLegend	Cat# 102418, RRID: AB_830757
Ter119	BioLegend	Cat# 116210, RRID: AB_313711
CD90.2/ Thy1.2	BioLegend	Cat# 105308, RRID: AB_313179
Ly6C	BioLegend	Cat# 128049, RRID: AB_2800630

(Continued on next page)

**Continued**

REAGENT or RESOURCE	SOURCE	IDENTIFIER
ATP5A1	Fortis Life Sciences	Cat# A304-939A, RRID: AB_2940773
<i>InVivoPlus</i> mouse IgG1 isotype control	Bio X Cell	Cat# BP0083, RRID: AB_2940778
<i>InVivoMAb</i> anti-mouse IFNAR-1	Bio X Cell	Cat# BE0241, RRID: AB_2687723
Anti-DYKDDDDK Tag (L5) Affinity Gel Antibody	Biolegend	Cat# 651502, RRID: AB_10959657
<b>Chemicals, peptides, and recombinant proteins</b>		
Doxorubicin	Selleck Chemicals	S1208
Hydralazine Hydrochloride	Spectrum	H1289
ISD	InvivoGen	tIrl-isdn
2'3'-cGAMP	InvivoGen	tIrl-nacga23-02
BrdU (5-Bromo-2'-Deoxyuridine)	Invitrogen	B23151
UltraPure™ Salmon Sperm DNA Solution	Invitrogen	15632011
ProLong Diamond Antifade Mountant	Invitrogen	P36961
HSC CellMask Green	Invitrogen	H32714
SYTOX® Green	Invitrogen	MP33025
Fetal Bovine Serum (FBS)	VWR	97068-085
Water, HyClone™ HyPure, Cell Culture Grade	VWR	82007-330
Dulbecco's Modified Eagle's Medium - high glucose	Sigma-Aldrich	D5796
Dulbecco's Phosphate Buffered Saline	Sigma-Aldrich	D8537
Polyinosinic-polycytidylic acid sodium salt	Sigma-Aldrich	P1530
ABT-737	Sigma-Aldrich	197333
Q-VD-OPh	Sigma-Aldrich	551476
Tamoxifen	Sigma-Aldrich	T5648
2',3'-Dideoxycytidine	Sigma-Aldrich	D5782
Polybrene Infection / Transfection Reagent	Sigma-Aldrich	TR-1003-G
cComplete™, Mini, EDTA-free Protease Inhibitor Cocktail	Sigma-Aldrich	04693159001
Benzonase® Nuclease	Sigma-Aldrich	71205-3
Human IFN Alpha Hybrid Protein	PBL Assay Science	11200-1
Recombinant Human IFN-beta Protein	R&D Systems	8499-IF-010
Recombinant Mouse IFN-beta Protein	R&D Systems	8234-MB-010
Recombinant Mouse IFN- $\alpha$	Biolegend	752806
Aphidicolin	Hello Bio	HB3690
4-Hydroxytamoxifen	Hello Bio	HB6040
Polyethylenimine (PEI)	Alfa Aesar	43896
Blasticidin S HCl	ThermoFisher Scientific	A1113903
Lipofectamine RNAiMAX reagent	ThermoFisher Scientific	13778150
T4 ligase	ThermoFisher Scientific	EL0011
Novex™ TBE Gels, 10%	ThermoFisher Scientific	EC6275BOX
4',6'-diamidino-2-phenylindole (DAPI)	ThermoFisher Scientific	62247
Exonuclease I	ThermoFisher Scientific	720735KU
SYBR Green I Nucleic Acid Gel Stain	MedChemExpress	HY-K1004
Rabbit TrueBlot® Set	Rockland	88-1688-31
Mouse TrueBlot® Set	Rockland	88-7788-31
Pierce™ Control Agarose Resin	ThermoFisher Scientific	26150
DNase I	Worthington Biochemical	LS002139
RNase A	Worthington Biochemical	LS005650
PerfeCTa SYBR Green FastMix	Quanta	84069
Necrostatin-1	Selleckchem	S8037
GSK'872	Selleckchem	S8465

(Continued on next page)

**Continued**

REAGENT or RESOURCE	SOURCE	IDENTIFIER
Blebbistatin	Selleckchem	S7099
Purified Anti-Mouse CD16 / CD32 (Fc Shield) (2.4G2)	TONBO	70-0161-M001
Ghost Dye™ Red 710	TONBO	13-0871-T100

**Critical commercial assays**

E.Z.N.A.® plasmid DNA minikit	D6942-02	Omega bio-tek
Quick-RNA microprep kit	Zymo Research	R1051
Direct-zol RNA miniprep kit	Zymo Research	R2052
Micro BCA™ Protein Assay Kit	ThermoFisher Scientific	23235
Nuclear Complex Co-IP Kit	Active Motif	54001
2'3'-cGAMP ELISA Kit	Cayman	501700
LDH Cytotoxicity Detection Kit	TaKaRa	MK401
Neonatal Cardiomyocyte Isolation Kit	Miltenyi Biotec	130-098-373

**Deposited data**

Raw and normalized count data from RNA-seq related to <a href="#">Table S1</a>	This paper	GEO: GSE223553
Raw and normalized count data from RNA-seq related to <a href="#">Table S2</a>	This paper	GEO: GSE223698
Mendeley dataset of additional confirmatory data not included in the paper	This paper	<a href="https://doi.org/10.17632/cnw3htbbm9.2">https://doi.org/10.17632/cnw3htbbm9.2</a>

**Experimental models: Cell lines**

iCell Cardiomyocytes	FUJIFILM Cellular Dynamics	01434
293FT	Invitrogen	R70007
COS-7	ATCC	CRL-1651
ARPE-19	ATCC	CRL-2302
Platinum-A cells	Cell Biolabs	RV-102
WT MEF	This paper	N/A
<i>Tfam</i> <sup>+/-</sup> MEF	This paper	N/A
<i>Zbp1</i> <sup>-/-</sup> MEF	This paper	N/A
<i>Tfam</i> <sup>+/-</sup> <i>Zbp1</i> <sup>-/-</sup> MEF	This paper	N/A

**Experimental models: Organisms/strains**

C57BL/6J	The Jackson Laboratory	Strain # 000664
B6.129P2- <i>Lyz2</i> <sup>tm1(cre)flp0</sup> /J	The Jackson Laboratory	Strain # 004781
B6.FVB(129)- <i>A1cfl</i> <sup>flg(Myh6-cre/Esr1<sup>+</sup>)1Jmk</sup> /J	The Jackson Laboratory	Strain # 005657
B6;SJL- <i>Sting1</i> <sup>tm1.1Camb</sup> /J	The Jackson Laboratory	Strain # 031670
B6(Cg)- <i>Ifnar1</i> <sup>tm1.1Ees</sup> /J	The Jackson Laboratory	Strain # 028256
B6.Cg- <i>Mx1</i> <sup>tm1.1Agsa</sup> /J	The Jackson Laboratory	Strain # 033219
C57BL/6J- <i>Sting1</i> <sup>fl</sup> /J	The Jackson Laboratory	Strain # 017537
B6.129S2- <i>Ifnar1</i> <sup>tm1Agt</sup> /Mmjax	The Jackson Laboratory	MMRRC Strain #032045-JAX
B6;129- <i>Mavs</i> <sup>tm1Zjc</sup> /J	The Jackson Laboratory	Strain # 008634
<i>Tfam</i> <sup>+/-</sup>	West et al. <sup>44</sup>	N/A
<i>Zbp1</i> <sup>-/-</sup>	Ishii et al. <sup>50</sup>	N/A
<i>Sting</i> <sup>fl/fl</sup> <i>LysMcre</i>	This paper	N/A
<i>Ifnar</i> <sup>fl/fl</sup> <i>LysMcre</i>	This paper	N/A
<i>Sting</i> <sup>fl/fl</sup> $\alpha$ MHC-MerCreMer	This paper	N/A
<i>Ifnar</i> <sup>fl/fl</sup> $\alpha$ MHC-MerCreMer	This paper	N/A

**Oligonucleotides**

See <a href="#">Table S3</a>	N/A	N/A
------------------------------	-----	-----

(Continued on next page)

**Continued**

REAGENT or RESOURCE	SOURCE	IDENTIFIER
<b>Recombinant DNA</b>		
pUNO1-mSTINGwt-HA3x	InvivoGen	puno1ha-mstingwt
pUNO1-mCGAS-HA3x	InvivoGen	puno1ha-mcgas
pUNO1-hCGAS-HA3x	InvivoGen	puno1ha-hcgas
p3XFLAG-CMV-10-mZBP1 FL	Sridharan et al. <sup>75</sup>	N/A
p3XFLAG-CMV-10-mZBP1 $\Delta Z\alpha 1$	Sridharan et al. <sup>75</sup>	N/A
p3XFLAG-CMV-10-mZBP1 $\Delta Z\alpha 1 Z\alpha 2$	Sridharan et al. <sup>75</sup>	N/A
p3XFLAG-CMV-10-mZBP1 mRHIMA	Sridharan et al. <sup>75</sup>	N/A
p3XFLAG-CMV-10-mZBP1 mRHIMB	Sridharan et al. <sup>75</sup>	N/A
p3XFLAG-CMV-10-mZBP1 $\Delta C$	Sridharan et al. <sup>75</sup>	N/A
p3XFLAG-CMV-10-hZBP1 FL	Jason W. Upton, Auburn University	N/A
pMXs-IRES-Blast-mSTING-HIS	This paper	N/A
p3XFLAG-CMV-14-mZBP1 FL	This paper	N/A
p3XFLAG-CMV-14-mZBP1 $\Delta RHIMA$	This paper	N/A
p3XFLAG-CMV-14-mZBP1 $\Delta RHIMB$	This paper	N/A
p3XFLAG-CMV-14-mZBP1 RHIMA+B	This paper	N/A
pcDNA3.1-mCGAS FL-HA	This paper	N/A
pcDNA3.1-mCGAS N-term-HA	This paper	N/A
pcDNA3.1-mCGAS $\Delta N$ -term -HA	This paper	N/A
pMXs-IRES-Blast-mSTING-HIS	This paper	N/A
<b>Software and algorithms</b>		
ZEN 3.3	Zeiss	N/A
NIS-Elements AR 5.21.02	Nikon	N/A
NIS-Elements D 5.02.01	Nikon	N/A
Huygens Essential 21.4.0	Scientific Volume Imaging	N/A
Vevo Lab 5.6.0	FUJIFILM VisualSonics	N/A
RNAseq Alignment V2.0.0	Illmina	N/A
RNA-seq Differential Expression V1.0.0	Illmina	N/A
Gene Set Enrichment Analysis software (GSEA) v4.2.3	Subramanian et al. <sup>110</sup> and Mootha et al. <sup>111</sup>	N/A
GraphPadPrism 9.5.0	GraphPad Software Inc.	N/A
ImageJ 1.8.0	NIH	N/A
FlowJo 10.8.2	BD Biosciences	N/A

**RESOURCE AVAILABILITY**

**Lead contact**

Further information and requests for resources and reagents should be directed to and will be fulfilled by the lead contact, A. Phillip West ([awest@tamu.edu](mailto:awest@tamu.edu)).

**Materials availability**

All primary cells, plasmids, and mouse strains generated in this study are available from the [lead contact](#) with a completed materials transfer agreement.

**Data and code availability**

All data needed to evaluate the conclusions drawn herein are present in the paper and/or the supplementary figures and tables. Any additional information required to reanalyze the data reported in this paper is available from the [lead contact](#) upon request. RNA-seq datasets have been deposited in the Gene Expression Omnibus under accession numbers GSE223553 and GSE223698. Additional confirmatory data from [Figures 1G, 1H, 2D, 2H, 2I, 3A, 5H, and S3C](#) were deposited on Mendeley at <https://doi.org/10.17632/cnw3htbbm9.2>.

## EXPERIMENTAL MODEL AND SUBJECT DETAILS

### Mouse husbandry and strains

C57BL/6J (strain 000664), *LysMCre* (strain 004781), *αMHC-MerCreMer* (strain 005657), *Sting<sup>fl/fl</sup>* (strain 031670), *Ifnar1<sup>fl/fl</sup>* (strain 028256), *Mx1<sup>gfp</sup>* (strain 033219), *Sting<sup>-/-</sup>* (*Sting1<sup>gt</sup>*; strain 017537) and *Ifnar1<sup>-/-</sup>* (MMRRC Strain #032045-JAX) mice were purchased from The Jackson Laboratory. *Mavs<sup>-/-</sup>* (strain 008634) mice were purchased from The Jackson Laboratory and were backcrossed onto the C57BL/6J background for 10 generations before use. *Tfam<sup>+/-</sup>* mice were previously reported.<sup>38,44</sup> *Zbp1<sup>-/-</sup>* mice<sup>50</sup> were obtained collaboratively from Dr. Ken Ishii and were backcrossed onto the C57BL/6J background for at least 4 generations before use. Breeding colonies of all strains were established and maintained on the C57BL/6J background at Texas A&M University. Mice were group-housed in humidity-controlled environments maintained at 22°C on 12-hour light–dark cycles (600–1800). Food and water were available ad libitum. All animal procedures were approved by the Texas A&M Animal Care and Use Committee (TAMU IACUC). The euthanasia methods employed in the study are consistent with the recommendations of the American Veterinary Medical Association (AVMA).

### Doxorubicin administration

Male and female mice between 8–12 weeks of age were housed in a standard 12-h light/dark cycle with unlimited access to food and water. Doxorubicin stock solution (10 mg/mL) was prepared in cell culture grade water (VWR, 82007–330) and used within 28 days. Further dilutions were made in DPBS (Sigma-Aldrich, D8537) on the day of injection. In Figure 6, *Mx1<sup>gfp</sup>*, *WTLysMcre*, *Sting<sup>fl/fl</sup>LysMcre* and *Ifnar<sup>fl/fl</sup>LysMcre* mice were intraperitoneally (i.p.) injected with one dose of 25 mg/kg of Doxorubicin. In Figure S6, Cre expression was induced by 3 i.p. injections of 30 μg/g of tamoxifen into *WTαMHC-MerCreMer*, *Sting<sup>fl/fl</sup>αMHC-MerCreMer* and *Ifnar<sup>fl/fl</sup>αMHC-MerCreMer* mice, followed by 4-weeks or rest, and of one i.p. injection of 25 mg/kg of Doxorubicin. In Figure 7, i.p. injection of Doxorubicin (5 mg/kg body weight, 100 μL injection volume) was performed weekly for four continuous weeks (cumulative dose 20 mg/kg body weight).

### Mouse melanoma induction, Doxorubicin, and adjuvant IFN $\alpha$ therapy

An autochthonous model of melanoma was utilized in Figures S6G–S6O, and melanomas were induced on equal numbers of 21-day-old male and female mice as described in Dankort et al.<sup>95</sup> First, mice were anesthetized by isoflurane, then a commercial topical depilatory cream was applied to remove hair from roughly 2 cm<sup>2</sup> on the lower dorsal region of mice approximately 1–2 cm from the base of the tail. The next day, mice were anesthetized with isoflurane and 1 μL of a 20 mM solution of 4-hydroxytamoxifen (Hello Bio, HB6040) dissolved in ethanol was applied topically to the exposed skin. Four weeks after melanoma induction, hair was removed from the lower dorsal region of the mice using hair trimmers to allow confirmation of tumor induction and monitoring of tumor growth. Tumors were measured for width, length, and height every 2–4 days using digital calipers in order to calculate tumor volume. Mice received vehicle (PBS) or Doxorubicin (5 mg/kg body weight, 100 μL i.p. injection volume) weekly for four consecutive weeks (cumulative dose 20 mg/kg body weight). Adjuvant IFN $\alpha$  (20,000 units) was co-administered together with Doxorubicin in a total volume of 100 μL or diluted with PBS in a total volume of 50 μL and i.p. injected alone as indicated in Figure S6H.

### Cardiac cell isolation

Cardiac cell isolation was performed as described by Ackers-Johnson et al.<sup>88</sup> with some modifications. Briefly, 8–12-week-old, male and female *Mx1<sup>gfp</sup>* mice i.p. injected with saline or Doxorubicin were anaesthetized using an isoflurane vaporizer, and anesthesia was maintained using a nose cone throughout the surgical procedure. Following anesthesia, thoracic cavities were opened to expose the heart. The descending aorta was severed to allow exsanguination, and 7 mL EDTA buffer was immediately injected into the right ventricle. Next, the ascending aorta was clamped using a hemostat, and the heart was removed then transferred to a 60 mm dish containing fresh EDTA buffer, then again injected with 10 mL EDTA buffer into the left ventricle at 2 to 3 mm above the heart apex. Next, the heart was transferred to a 60 mm dish containing perfusion buffer and injected with 3 mL of perfusion buffer through the same perforation on the left ventricle. Then, the heart was transferred to a 60 mm dish containing collagenase buffer, and digestion was achieved by continuously injecting collagenase buffer through the same perforation at the flow rate approximately 2 mL/min until the heart turned pale and flaccid and the injection perforation was enlarged. The atria and ventricles were gently separated, and then the ventricles (with septum) were transferred to a new 60 mm dish containing 3 mL fresh collagenase buffer. The digested tissues were pulled into 1 mm pieces using fine-tip forceps, single cardiac cells were dissociated by gently trituration, and finally the enzyme activity was neutralized by adding 5 mL stop buffer. Cell suspension was filtered through a 70 μm strainer, and cardiomyocytes were settled by gravity for 20 min in a 50 mL tube. The supernatant containing non-myocyte cardiac cells was subjected to staining for flow cytometry analysis, and the cardiomyocyte pellet was preserved for RNA and protein extraction for further analysis. All buffers were prepared in cell-culture grade water and recipes can be found in Ackers-Johnson et al.,<sup>88</sup> with the exception that 2,3-butanedione monoxime (BDM) was replaced with 5mM blebbistatin (Selleckchem, S7099). EDTA, perfusion, and collagenase buffers were appor- tioned into 10 mL syringes with 27 G needles and 60 mm dishes, then kept warm at 37°C.

### Cell culture

Primary WT, *Tfam*<sup>+/-</sup>, *Zbp1*<sup>-/-</sup>, and *Tfam*<sup>+/-</sup>*Zbp1*<sup>-/-</sup> MEFs were generated from E13.5–14.5 male and female embryos, maintained in DMEM (Sigma-Aldrich, D5796) supplemented with 10% low endotoxin FBS (VWR, 97068-085), and sub-cultured no more than five passages before experiments. Murine neonatal cardiomyocytes were isolated from 2–3-day-old male and female neonates with the Neonatal Cardiomyocyte Isolation Kit (Miltenyi Biotec, 130-098-373). Human iPSC-derived cardiomyocytes were purchased from Fujifilm Cellular Dynamics (01434) and cultured as described in the manual. 293FT cells were purchased from Invitrogen (R70007). COS-7 (CRL-1651) and ARPE-19 (CRL-2302) cells were purchased from ATCC.

### METHOD DETAILS

#### siRNA and DNA transfection

siRNA transfection was performed with 25 nM siRNA duplexes and 3  $\mu$ L of Lipofectamine RNAiMAX reagent (ThermoFisher Scientific, 13778150) according to the manufacturer's protocol. DNA transfection was performed with polyethylenimine, PEI (Alfa Aesar, 43896) at a ratio of 5:1 PEI to nucleic acids.

#### Southwestern blot

mtDNA isolation and southwestern blotting were performed as described previously.<sup>49</sup> In brief, MEFs were treated with 10  $\mu$ M aphidicolin (Hello Bio, HB3690) for 4 h, after which 50  $\mu$ M BrdU (Invitrogen, B23151) was added to the culture medium for an additional 24 h. Following treatment, DNA was isolated using the E.Z.N.A.® plasmid DNA minikit (Omega bio-tek, D6942-02), and 1  $\mu$ g of isolated DNA was loaded and run on a 0.45% agarose gel in TBE (26 V at 4 °C for 18–20 h). After electrophoresis, the agarose gel was washed with water and soaked in denaturing buffer (0.5M NaOH, 1.5M NaCl) for an hour with gentle shaking. Afterwards, the gel was rinsed again with water and soaked in 10X SSC for 30–60 min before capillary transfer to an ImmobilonP membrane (Millipore Sigma), as described previously.<sup>112</sup> Once transferred, the membrane was soaked in 6X SSC before undergoing UV cross-linking (UV Stratalinker 1800). The cross-linked membrane was blocked with 10% milk in TBST for 1 h, followed by immunoblotting with anti-BrdU antibody (BD Biosciences, 555627) for 2 h at room temperature. The membrane was then washed and incubated with HRP-linked anti-mouse IgG (EMD Millipore Etobicoke) for 1 h, after which the blot was developed using Supersignal West Femto enhanced chemiluminescence substrate (ThermoFisher Scientific) and imaged with a chemiluminescence imaging analyzer (Fujifilm, LAS3000mini).

#### Cloning and retroviral transduction

Murine STING-HA (InvivoGen) was subcloned into the pMXs-IRES-Puro vector and replication incompetent retroviruses were packaged using Platinum-A cells (Cell Biolabs, RV-102) according to the manufacturer's instructions. 293FT were exposed to supernatants containing pMXs-IRES-Blast-STING-His retroviruses and 4  $\mu$ g/mL polybrene (Millipore, TR-1003-G). Two days post transduction, 10  $\mu$ g/mL blasticidin was added to select a stable expression population.

#### Topologically constrained Z-DNA synthesis

Circular Z-DNA and B-DNA were synthesized as described by Zhang et al.<sup>55</sup> Briefly, 74-mer oligos containing a 5' phosphate modification (Sigma-Aldrich) were ligated to form circular single-stranded DNA (ssDNA) using a stepwise reaction. The 150  $\mu$ L reaction mixture contained 25  $\mu$ M splint, 75 U T4 ligase (ThermoFisher Scientific, EL0011), and 0.1X T4 ligase buffer. A second mix contained the corresponding 74-mer DNA oligo at 22  $\mu$ M in 150  $\mu$ L 0.1X T4 ligase buffer. 15  $\mu$ L of the DNA mix was added to the reaction mix every 20 min for a total of 10 additions bringing the total reaction volume to 300  $\mu$ L. After the final addition of DNA, the reaction was allowed to continue for another 12 h. The reaction was carried out at 20 °C and terminated by incubation at 65 °C for 10 min. Any remaining linear DNA was degraded by addition of 35  $\mu$ L 10X Exonuclease I buffer and 20  $\mu$ L Exonuclease I (ThermoFisher Scientific, 720735KU) and incubation at 37 °C for 2 h followed by 80 °C for 20 min. Circular ssDNA strands were purified by phenol/ chloroform extraction and ethanol precipitation.

ssDNA strands were annealed to form double-stranded B- or Z-DNA as follows. The annealing reaction contained 10 mM HEPES and 10 mM MgCl<sub>2</sub> at pH 7.5. Topologically constrained Z-DNA was obtained by annealing circular 74F ssDNA to circular 74R ssDNA strands at a 1:1 molar ratio. DNA strands were annealed in a thermocycler using the following steps: 90 °C for 5 min, cool to 60 °C at 0.1 °C/s, hold at 60 °C for 10 min, cool to 20 °C at 0.1 °C/s, and hold at 12 °C. B-DNA was made by annealing linear 74F ssDNA to circular 74R ssDNA or annealing circular 74F ssDNA to linear 74R ssDNA as described above. After annealing, fully double-stranded B-DNA was obtained by incubating the dsDNA with T4 ligase in 1X T4 ligase buffer for 12 h at 25 °C followed by incubation with Exonuclease I for 2 h at 37 °C and exonuclease inactivation at 80 °C for 20 min. Both B-DNA and Z-DNA were then purified by phenol/ chloroform extraction and ethanol precipitation. Purified DNA pellets were redissolved in 10 mM HEPES buffer (10 mM MgCl<sub>2</sub>, pH 7.5).

#### Electrophoretic mobility shift assay (EMSA)

Circular Z- and B-DNA were diluted to 10 ng/ $\mu$ L (0.43  $\mu$ M) in 10 mM HEPES buffer (10 mM MgCl<sub>2</sub>, pH 7.5) and incubated with anti-Z-DNA antibody (Absolute antibody, Ab00783-23.0) at a 1:1 or 1:3 DNA:antibody molar ratio for 4 h at 25 °C. DNA-antibody complexes

were resolved by electrophoresis on native 10 % TBE-polyacrylamide gels (ThermoFisher Scientific, EC6275BOX). DNA was visualized by post-staining with SYBR Green I (MedChemExpress, HY-K1004) and imaging on a Bio-Rad ChemiDoc MP Imaging System.

### Protein expression and purification

Full length mouse ZBP1 and mouse cGAS were cloned into a modified pET28a vector with a N-terminal Avi-His6-Sumo tag. Both ZBP1 and cGAS were expressed in *E. coli* BL21(DE3) with 0.4 mM isopropyl  $\beta$ -D-1-thiogalactopyranoside (IPTG) induction overnight at 15 °C. Proteins were purified using Ni-NTA agarose (QIAGEN), followed by size-exclusion chromatography using HiLoad 16/600 Superdex200 columns (GE Healthcare Life Sciences). The Avi-His6-Sumo tag was cleaved by sumo protease and removed using Superdex200 columns. Mouse ZBP1 was eluted in the buffer containing 20 mM Tris-HCl pH 7.5, 150 mM NaCl. Mouse cGAS was eluted in the buffer containing 20 mM Tris-HCl pH 7.5, 500 mM NaCl.

### cGAS activity assay

The cGAS activity assay was performed in 20 mM HEPES pH 7.5, 150 mM NaCl, 5 mM MgCl<sub>2</sub>, 5 mM DTT, 2.5 mM ATP, 2.5 mM GTP. 2  $\mu$ M mouse cGAS was incubated with 0.1  $\mu$ g/ $\mu$ L B-DNA or Z-DNA with or without 2  $\mu$ M mouse ZBP1 for 1 h at 37 °C. 2  $\mu$ M mouse cGAS was incubated with 0.1  $\mu$ g/ $\mu$ L salmon sperm DNA (Invitrogen, 15632-011) or no DNA for 1 h at 37 °C as the positive and negative control. Reactions were quenched by adding 20 mM EDTA. The products were filtered by 10 kDa-cutoff Amicon Ultra centrifugal filters to remove DNA and proteins and then analyzed by a Mono Q 5/50 GL column (GE Healthcare Life Sciences).

### Co-immunoprecipitation

For Figures 3B and 3C, MEFs were treated with 10 ng/mL of mouse IFN $\beta$  for 6 hrs or in 50 nM of Doxo for 48 hrs, respectively, before co-IP. The cytosolic fraction was obtained by lysing the cells with NP-40 lysis buffer (50 mM Tris pH7.5, 0.15 M NaCl, 1 mM EDTA, 1% NP-40 and 10% Glycerol), and nuclear fraction was acquired using Nuclear Complex co-IP kit (Active Motif, 54001), which allows a gentle release of DNA-bound protein complexes in the nucleus. Rabbit TrueBlot® Set (Rockland, 88-1688-31) was used for both pre-cleaning and co-IP from both fractions. Mouse TrueBlot® Set (Rockland, 88-7788-31) was used for pre-cleaning and co-IP with ZBP1 antibody in Figure 4B. For co-IPs of cGAS and ZBP1 constructs in 293FT (Figures 3E, 3J, S3I, S3J, S3M, and S3O), Pierce™ Control Agarose Resin (ThermoFisher Scientific, 26150) and Anti-DYKDDDDK Tag (L5) Affinity Gel Antibody (Biolegend, 651502) were used for pre-cleaning and IP, respectively. Due to different subcellular localizations of cGAS mutants, the cytosolic fraction and nuclear fraction were obtained as described above, combined and then used for co-IPs of cGAS mutants and ZBP1 in 293FT (Figure S3J). For cell-free co-IP in Figure 3I, protein and DNA are mixed at molar ratio of 1:2. To degrade cytosolic nucleic acids in Figure S3M before co-IP, NP-40 cell lysates were incubated with 10 U/ $\mu$ L of benzonase (Millipore, 71205-3) for 4 h at 4 °C. BSA was added to the samples that were not treated with benzonase to even protein concentration. 20  $\mu$ L of sample was separated and the benzonase was inactivated by adding 0.5  $\mu$ L of 0.5 M EDTA and heating to 95 °C for 15 min. 10 ng/ $\mu$ L DNA was used in qPCR to amplify mtDNA using primers against mt-ND1. To degrade cytosolic DNA or RNA in Figure 3G before co-IP, NP-40 cell lysates were incubated with 100  $\mu$ g/mL of DNase I (Worthington Biochemical, LS002139) or 50  $\mu$ g/mL of RNase A (Worthington Biochemical, LS005650) for 4 h at 4 °C. After incubation, DNA was extracted using Phenol/chloroform and 10 ng/ $\mu$ L DNA was used in qPCR to amplify mtDNA using primers against mt-ND2; RNA was extracted using Quick-RNA microprep kit (Zymo Research, R1051) and subjected to qRT-PCR to amplify 16s RNA.

### Subcellular fractionation, DNA isolation, and slot blotting

3 x 10<sup>6</sup> MEFs were seeded in 15 cm dishes overnight and treated with vehicle or 500 nM of Doxo for 24 hrs. Subcellular fractionation and DNA isolation were performed as previously described.<sup>113</sup> In brief, cells were lysed in digitonin lysis buffer (150 mM NaCl, 50 mM HEPES pH 7.4, and 5  $\mu$ g/mL digitonin), incubated end over end for 10 min at 4 °C, and centrifuged at 950 x g for 5 min at 4 °C. The cytosolic supernatants were transferred into a new tube and saved as cytosolic fraction, and the pellets were lysed in NP-40 lysis buffer (50 mM Tris pH 7.5, 0.15 M NaCl, 1 mM EDTA, 1% NP-40 and 10% Glycerol). After centrifugation of NP-40 lysates at 21130 x g for 10 min at 4 °C, the supernatants were transferred and saved as mitochondrial fraction, and the nuclei pellets were further lysed in and SDS lysis buffer (20 mM Tris pH 8 and 1% SDS). SDS lysates were boiled at 95 °C for 5 min and centrifuged at 21130 x g for 5 min at RT. The supernatants were transferred and saved as nuclear fraction. All fractions were treated with 50  $\mu$ g/mL of RNase A for 1.5 hrs at 37 °C and 200  $\mu$ g/mL of Proteinase K for 1 h at 55 °C before being subjected to Phenol-Chloroform based DNA isolation. After DNA isolation, 200  $\mu$ g of cytosolic DNA, 1 mg of mitochondrial DNA and 50  $\mu$ g of nuclear DNA were blotted onto 0.45  $\mu$ m Nylon membranes (Whatman, 10416230). After air drying, membranes were incubated in primary antibodies at 4 °C overnight in 1X PBS containing 1% casein, HRP-conjugated secondary antibody at room temperature for 1 h, and then developed with Luminata Crescendo Western HRP Substrate (Millipore, WBLUR0500).

### Quantitative PCR

To measure relative gene expression by qRT-PCR in cells and tissues, total cellular RNA was isolated using Quick-RNA microprep kit (Zymo Research, R1051). Approximately 0.5-1  $\mu$ g RNA was isolated, and cDNA was generated using the qScript cDNA Synthesis Kit (Quanta, 95047-100). cDNA was then subjected to qPCR using PerfeCTa SYBR Green FastMix (Quanta, 84069). Technical triplicates were run each biological sample, and average expression values were normalized against *Rp37* cDNA using the 2<sup>- $\Delta\Delta$ CT</sup> method.<sup>113</sup>

For mtDNA abundance assessment, 10 ng/ $\mu$ L of template DNA was used for qPCR, and expression values of each replicate were normalized against nuclear-encoded *Tert* or *RNA18S*.<sup>113</sup>

### Immunoblotting

Cells and tissues were lysed in NP-40 lysis buffer or SDS lysis buffer supplemented with protease inhibitor (Roche, 04693159001) and then centrifuged at 4 °C to obtain cellular lysate. After BCA protein assay (ThermoFisher Scientific, 23235), equal amounts of protein (10–40  $\mu$ g) were loaded into 10–20% SDS–PAGE gradient gels and transferred onto 0.22  $\mu$ M PVDF membranes (Bio-Rad, 1620177). After air drying to return to a hydrophobic state, membranes were incubated in primary antibodies at 4 °C overnight in 1X PBS containing 1% casein, HRP-conjugated secondary antibody at room temperature for 1 h, and then developed with Luminata Crescendo Western HRP Substrate (Millipore, WBLUR0500). For cGAS quantifications in [Figures S3E](#) and [S3F](#), cytosolic cGAS expression was normalized to GAPDH, and nuclear cGAS was normalized to LMNB1. These normalized values were used to calculate the percentage of cGAS in the cytosolic (cytosolic cGAS/ total cGAS) and nuclear (nuclear cGAS/ total cGAS) compartments.

### Immunofluorescence microscopy

Cells were grown on coverslips and treated as described. After washing in PBS, cells were fixed with 4% paraformaldehyde for 20 min, permeabilized with 0.1% Triton X-100 in PBS for 5 min, blocked with PBS containing 5% FBS for 30 min, stained with primary antibodies for 1 h, and stained with secondary antibodies for 1 h. Cells were washed with PBS containing 5% FBS between each step. Coverslips were exposed to 200 ng/mL 4',6-diamidino-2-phenylindole (DAPI) (ThermoFisher Scientific, 62247) for 2 min to label nuclei, then mounted with ProLong Diamond Antifade Mountant (Invitrogen, P36961) and sealed with clear nail polish. For experiments requiring cytosolic signal quantification, HSC CellMask Green (Invitrogen, H32714) was added to coverslips at 2  $\mu$ g/mL for 30 min, then washed several times in PBS, before DAPI staining. For [Figure S2C](#), SYTOX (Invitrogen, MP33025) was added to coverslips at 0.17  $\mu$ M for 15 min, then washed in PBS. For [Figure 1J](#), images were acquired on a LSM 780 confocal microscope (Zeiss) with a 40x oil-immersed objective and ZEN 3.3 software. For [Figures 1F](#), [2C](#), [2E](#), [2G](#), [3A](#), [3K](#), [3M](#), [5F](#), [5G](#), [S2C](#), [S2E](#), [S3C](#), [S3G](#), and [S4H](#) images were acquired on an ECLIPSE Ti2 (Nikon) with a 60x oil-immersed objective and NIS-Elements AR 5.21.02 software. Representative images shown in [Figures 1F](#), [2C](#), [2E](#), [2G](#), [5F](#), [5G](#), [S2E](#), [S3C](#), and [S4H](#) were imported into Huygens Essential software (v21.4.0) and deconvolved using the 'aggressive' profile in the Deconvolution Express application. In [Figures 3L](#), [S3D](#), and [S3H](#), the nuclear cGAS intensity in each cell was quantified within the DAPI positive area, and cytosolic cGAS intensity per cell was quantified in the CellMask positive area minus the DAPI positive area ( $n \geq 30$  fields for each group from at least 3 biological replicates). In [Figures 2D](#), [2F](#), [2H](#), [5H](#), [S2F](#), [S2G](#), [S2H](#), and [S5C](#), the non-nuclear Z-DNA intensity per cell (cytoplasmic space including cytosol, mitochondria, and other organelles) was calculated from the whole cell area minus the DAPI positive area ( $n \geq 20$  or 30 fields for each group from at least 3 biological replicates). Z-DNA signals colocalizing with TOMM20 signals were quantified as mitochondrial Z-DNA, while the remaining non-nuclear Z-DNA staining was quantified as cytosolic Z-DNA. cGAS and Cellular Z-DNA intensity were quantified from Nikon.nd2 files using NIS-Elements AR 5.21.02.

### Flow cytometry

The supernatants from cardiac isolations were centrifuged at 300 x g, 4C for 5 min with the centrifuge brake off to pellet the non-myocyte cells. The cell pellet was washed with 1 x PBS containing 5% FBS, resuspended in 1 x PBS with Fc Shield (TONBO, 70-0161-M001) and Ghost Dye Red 710 (TONBO, 13-0871-T100), and then loaded at 50  $\mu$ L/well onto Laminar Wash Plates (Curiox, 96-DC-CL-05). The cells were left on ice for 25 min in dark to settle and then washed using Curiox Laminar Wash HT2000 system at the flow rate of 5  $\mu$ L/s for 7 times. After wash, the cells were left in the wells with 25  $\mu$ L of wash buffer. Antibodies were diluted in 1 x PBS containing 5% FBS as 2 x working solution, and 25  $\mu$ L of the 2 x antibodies were loaded into each well. The cells were incubated with antibodies on ice for 30 min in dark, and then wash as previously described for 12 times. After wash, the cells were collected in polystyrene round-bottom 12 x 75 mm tubes for flow cytometry analysis on Cytex® Aurora 5-Laser Spectral Cytometer.

### Echocardiography

Mice were depilated at the chest area the day before echocardiography measurements. Anesthesia was induced by placing mice in a box with inhaled isoflurane at 2–3%. Afterwards, light anesthesia was maintained using a nose cone with inhaled isoflurane at 0.5–1%. Mice were immobilized on a heated stage, and continuous electric cardiogram (ECG), respiration, and temperature (via rectal probe) were monitored. Light anesthesia and core temperature were maintained to ensure near physiological status with heart rate at range of 470–520 beats per minute. Transthoracic echocardiography was performed using a VisualSonics Vevo 3100 system with a MX550D imaging transducer (center frequency of 40MHz). Parasternal long-axis (B-mode) and parasternal short-axis (M-mode) views of each animal were taken. Vevo LAB cardiac analysis package was used to analyze the data.

### Histology

Mice were euthanized and tissues were washed in PBS and incubated for 24 h in 10% formalin and then transferred to 70% ethanol. Tissue embedding, sectioning, and staining were performed at AML Laboratories in St. Augustine, FL. Images of the H&E staining and Picosirius red (P. Red) slides were acquired on ECLIPSE Ts2 (Nikon) with a 20x or 40x objective and NIS-Elements D 5.02.01 (Nikon)

software. Blinded scoring of 9 independent fields of view from 6 hearts per genotype and treatment was performed to determine percent of cardiomyocytes exhibiting vacuolization post-Doxo. Collagen area was quantified using ImageJ.

### Immunofluorescence staining in cardiac sections

Formalin-Fixed Paraffin-Embedded (FFPE) tissue sections were baked for 30 min, deparaffinized in xylene, and rehydrated by serial passage through graded concentrations of ethanol. Endogenous peroxidase in tissues was blocked with 0.9% H<sub>2</sub>O<sub>2</sub>/methanol for 40 min. Multiple (5) sequential heat-induced epitope retrieval (HIER) treatments were performed for 20 min each at 92–96°C in Citrate pH 6.0 buffer. After each HIER cycle in Citrate pH 6.0 buffer, sections were rinsed with diH<sub>2</sub>O and cooled at RT for 20 min. Tissue sections were circled with hydrophobic barrier pens and blocked with 20% normal goat serum for 20 min before incubation with primary antibody for 20 min. Then, sections were rinsed with TBST for 10 min and incubated with HRP-conjugated secondary (A120-501P) for 20 min, followed by another 10 min rinse in TBST. Incubation with Opal fluorophore Opal690 was then done for 10 min, followed by a 10 min rinse in diH<sub>2</sub>O. Bound primary and secondary antibodies were then subject to the next HIER treatment (as aforementioned) for 20 min. After staining with the Opal fluorophore, tissue specimens were stained with DAPI for 10 min and mounted in VECTASHIELD Vibrance Antifade Mounting Medium (ThermoFisher Scientific). Vectra Polaris Automated Quantitative Pathology Imaging System (Akoya Biosciences) was used for multispectral imaging at 40× magnification. Qupath<sup>114</sup> and ImageJ were used to export the images and to quantify the ATP5A1 fluorescence intensity.

### RNA sequencing and bioinformatic analyses

Total cellular RNA from WT, *Tfam*<sup>+/-</sup>, *Zbp1*<sup>-/-</sup> and *Tfam*<sup>+/-</sup>*Zbp1*<sup>-/-</sup> MEFs was prepared using Quick-RNA microprep kit (Zymo Research, R1051) and total cellular RNA from cardiomyocytes isolated from vehicle- and Doxo-treated mice was prepared using Direct-zol RNA miniprep kit (Zymo Research, R2052). Next-generation RNA sequencing procedure for both sets of samples were performed at Texas A&M University Bioinformatics Core. RNA sequencing data were analyzed using BaseSpace Sequence Hub (Illumina). In brief, STAR algorithm of RNAseq Alignment V2.0.0 software was utilized to align the results to reference genome *Mus musculus/mm10* (RefSeq), then RNA-seq Differential Expression V1.0.0 software was used to obtain raw gene expression files and determine statistically significant changes in gene expression in *Tfam*<sup>+/-</sup>, *Zbp1*<sup>-/-</sup> and *Tfam*<sup>+/-</sup>*Zbp1*<sup>-/-</sup> MEFs relative to WT, or cardiomyocytes from Doxo-treated mice related to vehicle-treated mice. Heat maps were generated using GraphPad Prism. For Figures 5A and S5B, GSE40289 and GSE79413 datasets from the Gene Expression Omnibus (GEO) were analyzed using Gene Set Enrichment Analysis software (GSEA, Broad Institute)<sup>110,111</sup> to identify differentially regulated pathways, Set Comparison Appyter<sup>115</sup> and Enrichr<sup>116–118</sup> to identify the interactions between datasets and overlapping genes. For Figures 6B and 6D, RNA-seq data from cardiomyocytes isolated from adult mouse hearts post Doxo challenge compared to vehicle controls were analyzed using ShinyGo<sup>119</sup> to generate the dot plots and GSEA to generate the enrichment plots.

### QUANTIFICATION AND STATISTICAL ANALYSIS

Error bars displayed throughout the manuscript represent standard error of the mean (s.e.m.) and were calculated from triplicates unless otherwise indicated. For in vivo experiments, error bars were calculated from the average of triplicate technical replicates of at least 5 animals per point. For microscopy quantification, images were taken throughout the slide of each sample using the DAPI channel to avoid bias of selection. To reduce potential experimental bias, samples for cardiac function (EF, FS, IVS;s, LVID;s, LVPW;s, LVPW;d and LV mass) and histological analyses were blinded to researchers when performing analysis. The identities were only revealed at the final data analysis stage. No randomization or blinding was used for all other animal studies. No statistical method was used to predetermine sample size. Data shown are representative of at least 3 independent experiments, including microscopy images, western blots, gene expression analyses and all other cellular assays. All calculations of significance were determined using GraphPad Prism 9.5.0 software. The significance was determined by a p value of < 0.05, and annotated as \*P < 0.05, \*\*P < 0.01, and \*\*\*P < 0.001.

# Supplemental figures

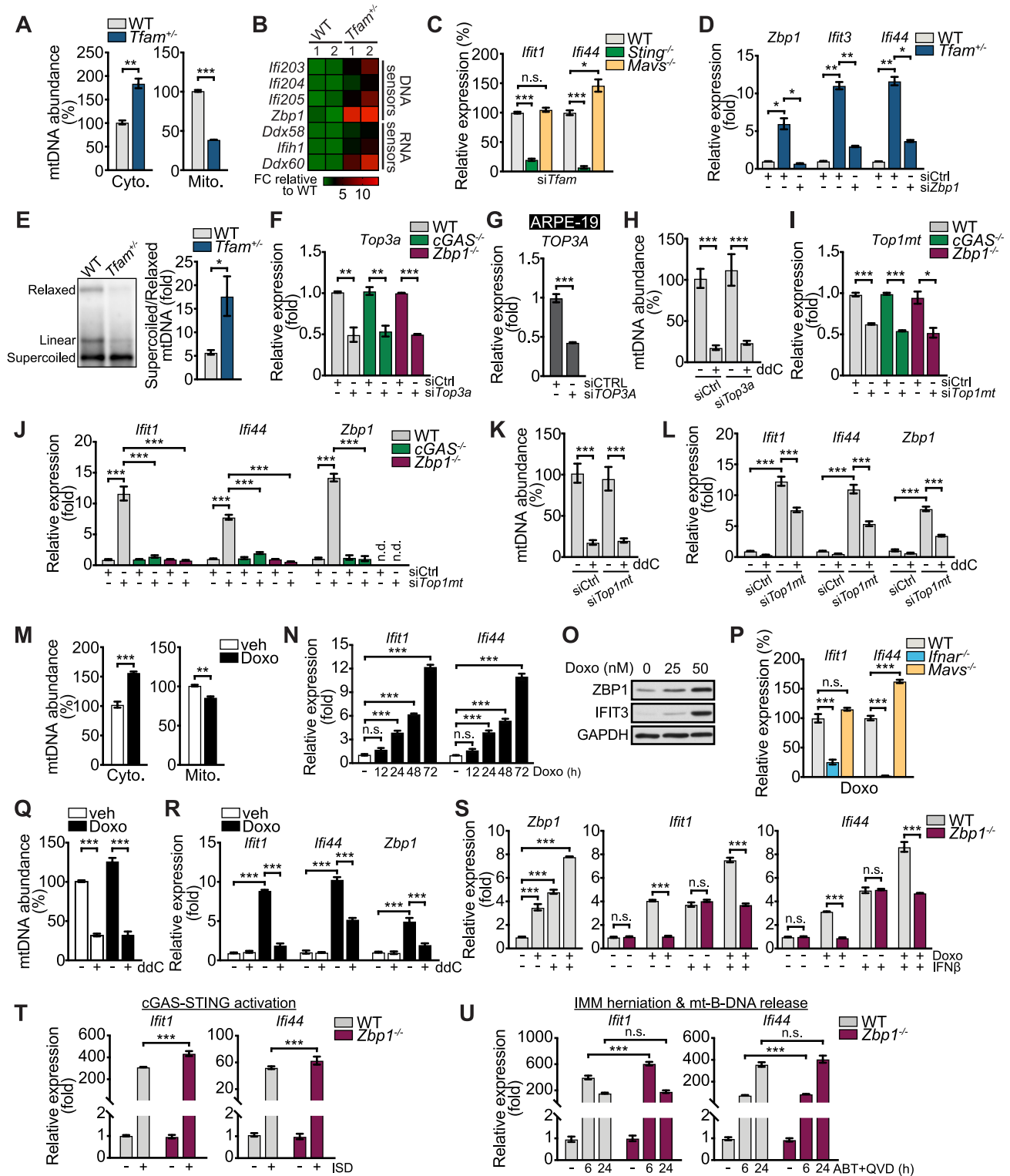


**Figure S1. ZBP1 is required for robust IFN-I responses downstream of mtDNA stress, related to Figure 1**

- (A) qPCR analysis of mtDNA abundance in the cytosol (Cyto.) and mitochondrial (Mito.) fraction from WT and *Tfam*<sup>+/-</sup> MEFs.
- (B) Heatmaps of RNA-seq data displaying upregulated DNA and RNA sensors in WT and *Tfam*<sup>+/-</sup> MEFs. Fold changes (FCs) are normalized to the average of WT MEFs.
- (C) qRT-PCR analysis of ISGs in WT, *Sting*<sup>-/-</sup>, and *Mavs*<sup>-/-</sup> MEFs transfected with si*Tfam* for 72 h.
- (D) qRT-PCR analysis of ISGs in WT and *Tfam*<sup>+/-</sup> MEFs transfected with siCtrl or si*Zbp1* for 96 h.
- (E) Southwestern blots of mtDNA isolated from WT and *Tfam*<sup>+/-</sup> MEFs (left). Quantification of supercoiled to relaxed mtDNA ratio (right).
- (F) qRT-PCR analysis of *Top3a* in WT, *cGAS*<sup>-/-</sup>, and *Zbp1*<sup>-/-</sup> MEFs transfected with siCtrl or si*Top3a* for 96 h.
- (G) qRT-PCR analysis of *TOP3A* in ARPE-19 transfected with siCTRL or si*TOP3A* for 72 h.
- (H) qPCR analysis of mtDNA abundance in WT MEFs transfected with siCtrl or si*Top3a* with or without 2',3'-dideoxycytidine (ddC, 100 μM) for 72 h.
- (I and J) qRT-PCR analysis of *Top1mt* (I) and ISGs (J) in WT, *cGAS*<sup>-/-</sup> and *Zbp1*<sup>-/-</sup> MEFs transfected with siCtrl or si*Top1mt* for 96 h.
- (K) qPCR analysis of mtDNA abundance in WT MEFs transfected with siCtrl or si*Top1mt* with or without ddC (100 μM) for 72 h.
- (L) qRT-PCR analysis of ISGs in WT MEFs transfected with siCtrl or si*Top1mt* with or without ddC (100 μM) for 72 h.
- (M) qPCR analysis of mtDNA abundance in Cyto. and Mito. fraction from vehicle (veh) or Doxorubicin (Doxo) treated WT MEFs.
- (N) qRT-PCR analysis of ISGs in Doxo (125 nM) treated MEFs.
- (O) Western blots of ISGs in Doxo (48 h) treated MEFs.
- (P) qRT-PCR analysis of ISGs in WT, *Ifnar*<sup>-/-</sup>, and *Mavs*<sup>-/-</sup> MEFs treated with or without Doxo (500 nM, 24 h).
- (Q and R) qPCR analysis of mtDNA abundance (Q) and qRT-PCR analysis of ISGs (R) in WT MEFs treated with veh or Doxo (250 nM, 24 h) with or without ddC (100 μM) for 72 h.
- (S) qRT-PCR analysis of ISGs in Doxo (50 nM, 48 h) treated WT and *Zbp1*<sup>-/-</sup> MEFs with or without IFNβ priming (10 pg/mL, 18 h).
- (T and U) qRT-PCR analysis of ISGs in WT and *Zbp1*<sup>-/-</sup> MEFs transfected with ISD (2 μg/mL) for 6 h (T) or treated with ABT-737 (ABT, 10 μM) + Q-VD-OPH (QVD, 10 μM) for 6 and 24 h (U). Statistical significance was determined using unpaired t test (A, C, E, F, G, I, M, and P), or analysis of variance (ANOVA) and Tukey (D, H, J-L, N, Q, and R) or Šídák (S-U) post hoc test. \*p < 0.05, \*\*p < 0.01, and \*\*\*p < 0.001. Error bars represent SEM.



**Figure S2. Mitochondrial genome instability promotes the accumulation and cytosolic release of mitochondrial Z-form DNA that potentiates IFN-I responses, related to Figure 2**

- (A) Quantification of unshifted DNA band from 3 independent electrophoretic mobility shift assay (EMSA) experiments in Figure 2B.
- (B) Slot blots of B-DNA and Z-DNA.
- (C) Representative images of WT MEFs transfected with polyethylenimine (PEI) complexed B-DNA or Z-DNA and stained with anti-Z-DNA antibody and SYTOX.
- (D) Schematic illustration of DNA extraction and transfection from different subcellular pools (left). Slot blots of cytosolic, mitochondrial, and nuclear DNA isolated from WT MEFs treated with veh or Doxo.
- (E) Representative images of WT MEFs transfected with si*Top3a* or si*Top1mt* or treated with Doxo with or without ddC (100  $\mu$ M). Anti-pan-DNA and -HSP60 (Mito.) antibodies were used for staining. Inset panels are magnified 4 $\times$ .
- (F) Mean fluorescent intensity (MFI) quantification of Cyto. and Mito. Z-DNA fluorescent intensities in WT MEFs transfected with si*Top3a* or si*Top1mt* or treated with Doxo with or without ddC (100  $\mu$ M). MFI percentiles are normalized to groups without ddc treatment.
- (G) Quantification of Cyto. and Mito. Z-DNA MFI in WT MEFs treated with ABT-737 (ABT, 1  $\mu$ M) + Q-VD-OPH (QVD, 1  $\mu$ M) for 6 and 24 h. MFI percentiles are normalized to DMSO control-treated (0 h) WT MEFs.
- (H) Quantification of Cyto. and Mito. Z-DNA fluorescent intensities in WT MEFs transfected with siCtrl or si*Tfam* for 72 h and treated with hydralazine (Hyd, 100  $\mu$ M) for 24 h. MFI percentiles are normalized to WT MEFs transfected with siCtrl.
- (I) qRT-PCR analysis of ISGs in WT and *Zbp1*<sup>-/-</sup> MEFs transfected with siCtrl or si*Tfam* for 72 h and treated with or without Hydralazine (100  $\mu$ M) for 24 h.
- (J) qRT-PCR analysis of ISGs in ARPE-19 transfected with B-DNA or Z-DNA (1  $\mu$ g/mL) for 16 h with or without IFN-I priming (10 pg/mL, 8 h).
- (K) Enzyme activity assay of cGAS in the presence of B-DNA, Z-DNA, salmon sperm DNA, or no DNA. Statistical significance was determined using ANOVA and Tukey (A and H), Dunnett (G) or Šídák (I and J) post hoc test, or unpaired t test (F). \*p < 0.05, \*\*p < 0.01, and \*\*\*p < 0.001. Error bars represent SEM.

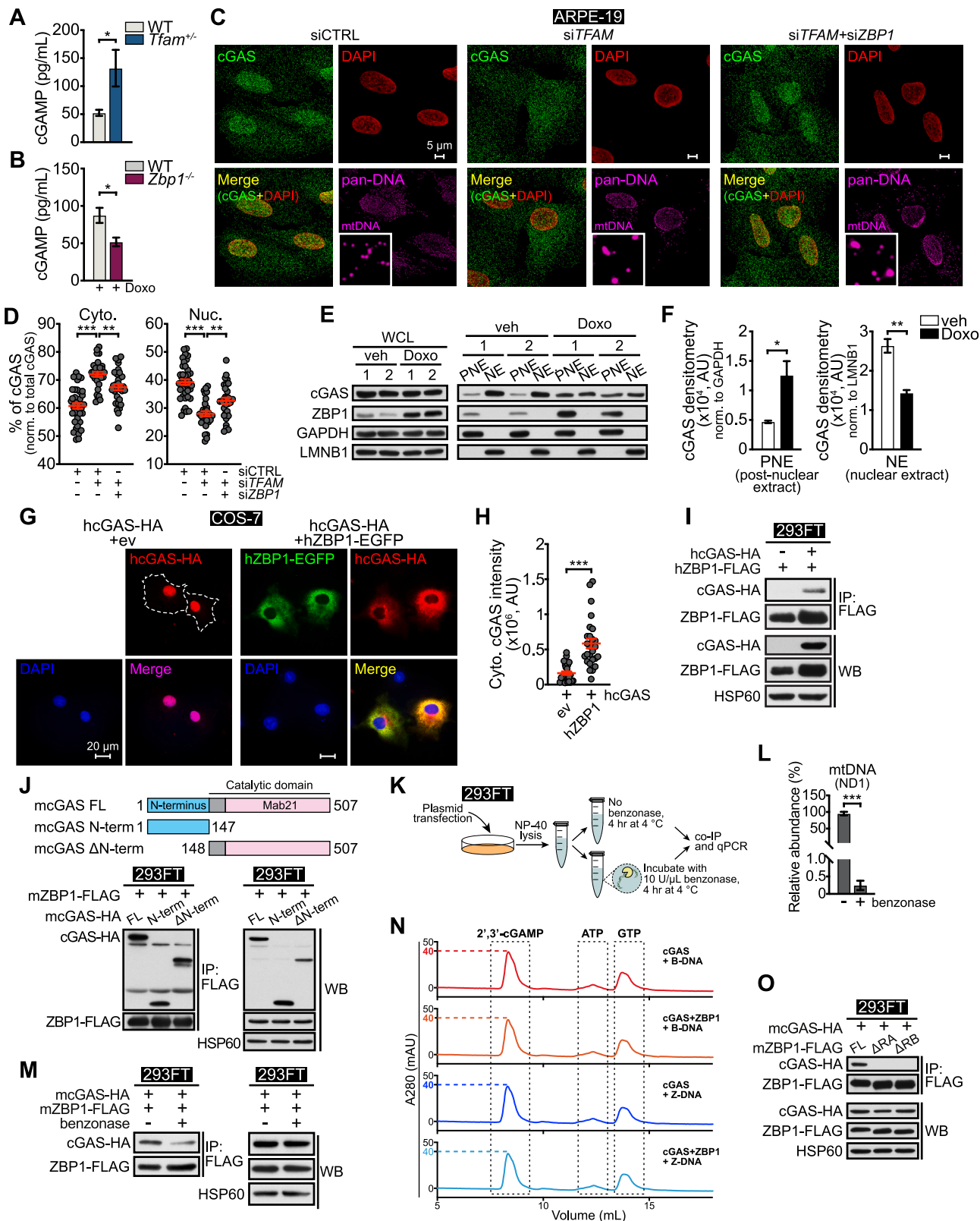
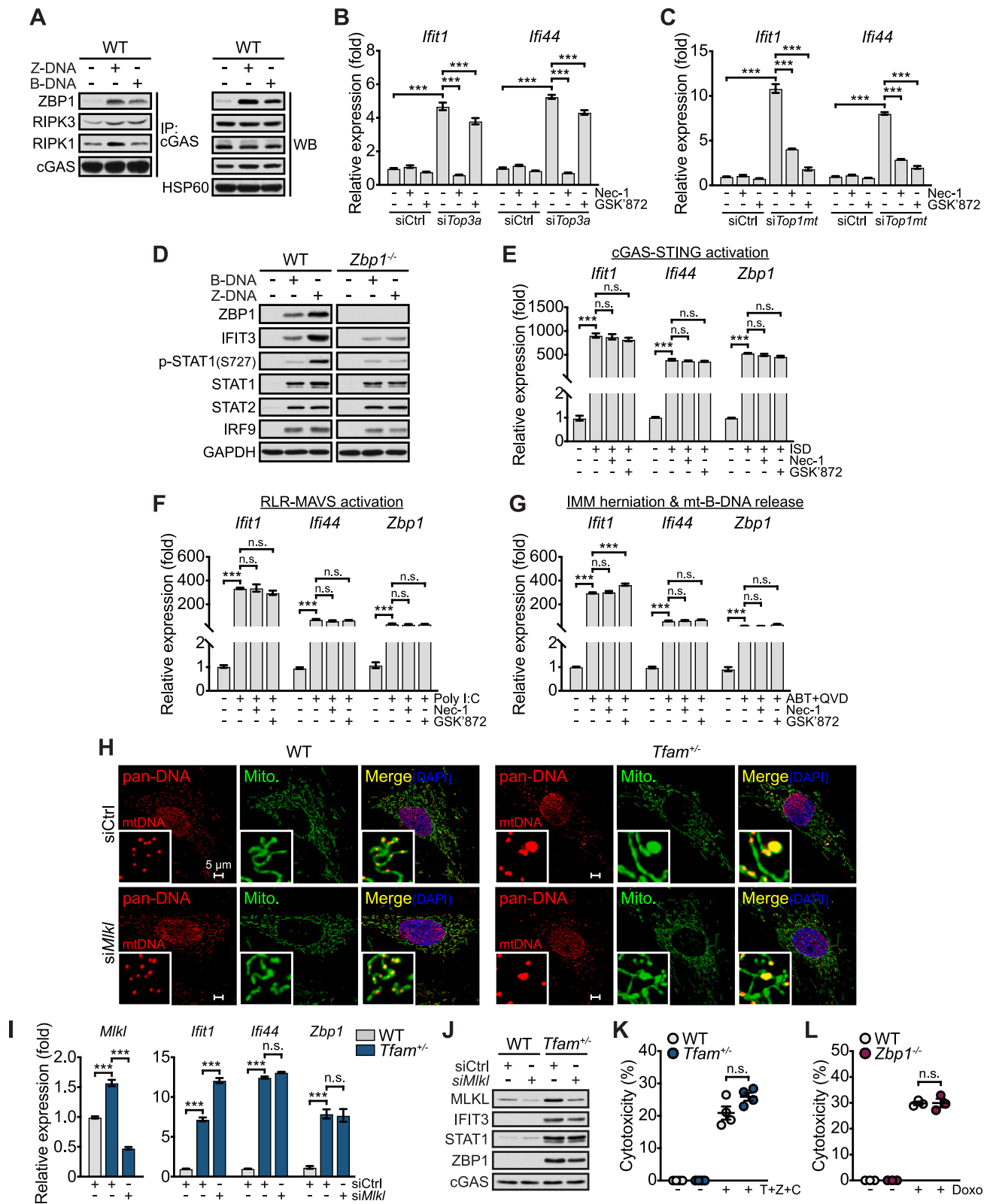


**Figure S3. ZBP1 interacts with cGAS in the cytoplasm, related to Figure 3**

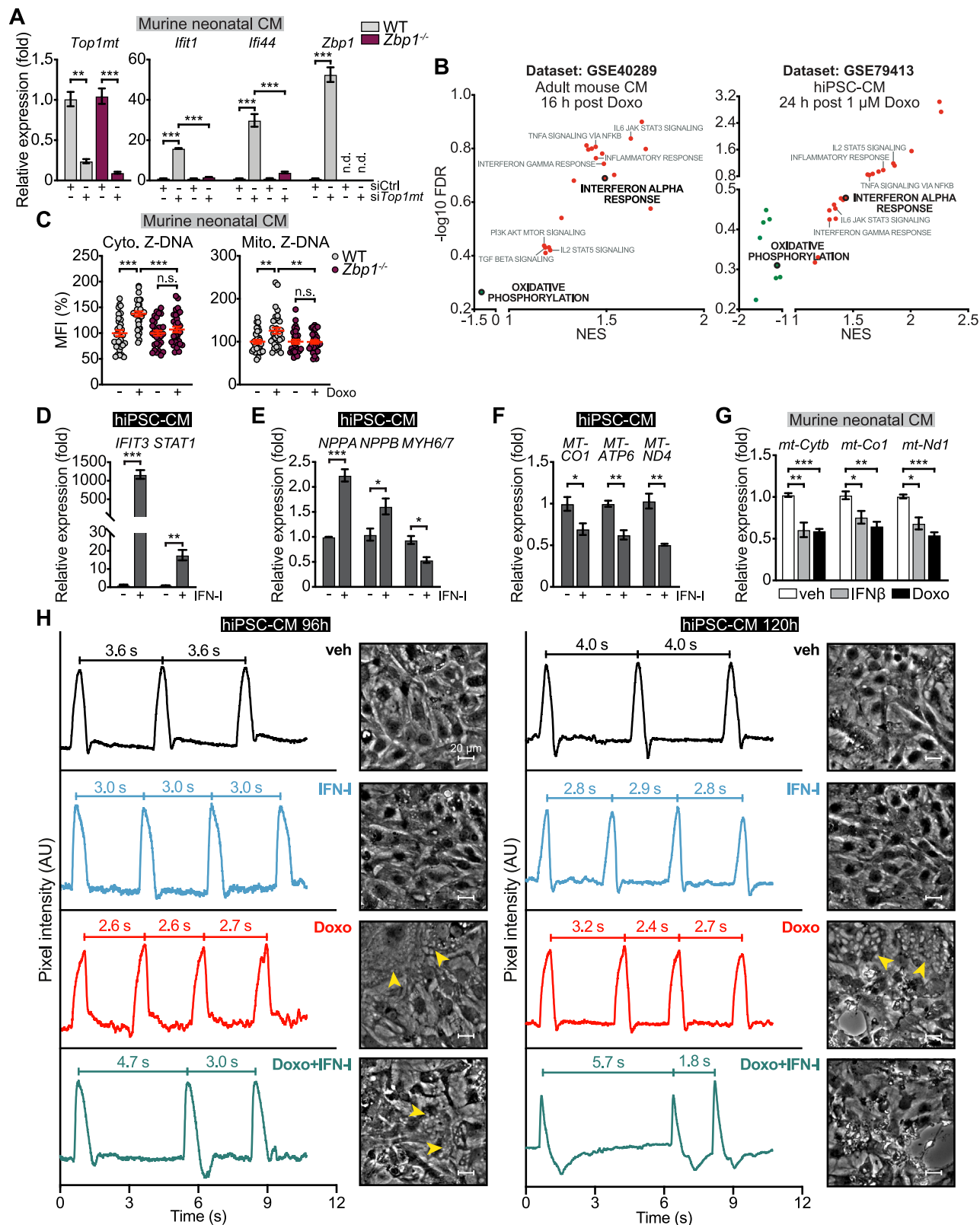
- (A) cGAMP production in WT and *Tfam*<sup>+/-</sup> MEFs (n ≥ 4) measured by ELISA.
- (B) cGAMP production in Doxo-treated WT and *Zbp1*<sup>-/-</sup> MEFs (n = 8) measured by ELISA.
- (C and D) Representative images of ARPE-19 transfected with indicated siRNAs for 72 h and stained with anti-cGAS and -pan-DNA antibodies and DAPI (C). Inset panels are magnified 4×. Cyto. and nuclear (Nuc.) fractions of cGAS are quantified in (D).
- (E and F) Western blots of cytosolic and nuclear proteins in veh or Doxo (50 nM) treated WT MEFs (E). cGAS intensities from post-nuclear extract (PNE) and nuclear extract (NE) in veh or Doxo-treated WT MEFs are quantified in (F). 2 different MEF lines are shown in the western blots, and 3 different MEF lines were used for quantification. a.u., arbitrary unit.
- (G and H) Representative images of COS-7 expressing indicated proteins and stained with anti-HA and -EGFP antibodies and DAPI (G). Cytosolic cGAS-HA intensity is quantified in (H).
- (I) CoIP showing interactions between human ZBP1 and human cGAS in 293FT.
- (J) Schematic representation of the mcGAS full-length (FL) and truncations (top). CoIP showing interactions between mZBP1 and mcGAS FL and truncations in 293FT (bottom).
- (K) Schematic illustration of coIP method used in (M).
- (L) qPCR analysis of mt-ND1 abundance in cell lysates from (M).
- (M) CoIP between mcGAS and mZBP1 in 293FT with or without benzonase treatment.
- (N) Enzyme activity assay of cGAS in the presence of B-DNA or Z-DNA, with or without ZBP1.
- (O) CoIP showing interactions between mcGAS and mZBP1 FL and deletions in 293FT. Statistical significance was determined using unpaired t test (A, B, F, H, and L), or ANOVA and Tukey post hoc test (D). \*p < 0.05, \*\*p < 0.01, and \*\*\*p < 0.001. Error bars represent SEM.



(legend on next page)

**Figure S4. RIPK1 and RIPK3 mediate mtDNA stress-induced IFN-I signaling independently of MLKL and cell death, related to Figure 4**

(A) CoIP from WT MEFs transfected with Z-DNA or B-DNA (100 ng/mL, 24 h).  
 (B and C) qRT-PCR analysis of ISGs in WT MEFs transfected with siCtrl, si*Top3a* (B) or si*Top1mt* (C) for 48 h and then treated with Nec-1 (10  $\mu$ M) or GSK'872 (2.5  $\mu$ M) for an additional 48 h.  
 (D) Western blots of WT and *Zbp1*<sup>-/-</sup> MEFs transfected with B-DNA or Z-DNA (125 ng/mL) for 24 h.  
 (E–G) qRT-PCR analysis of ISGs in WT MEFs transfected with ISG (2  $\mu$ g/mL) for 12 h (E), poly(I:C) (1  $\mu$ g/mL) for 6 h (F), or treated with ABT-737 (ABT, 10  $\mu$ M) + Q-VD-OPH (QVD, 10  $\mu$ M) for 6 h (G).  
 (H) Representative fluorescence images of WT and *Tfam*<sup>+/-</sup> MEFs transfected with siCtrl and si*Mkl1* for 96 h and stained with anti-pan-DNA and -HSP60 antibodies and DAPI. Inset panels are magnified 4 $\times$ .  
 (I and J) qRT-PCR analysis (I) and western blots (J) of MLKL and ISGs in WT and *Tfam*<sup>+/-</sup> MEFs transfected with siCtrl or si*Mkl1* for 96 h.  
 (K) LDH assay (n = 4) showing cytotoxicity in WT and *Tfam*<sup>+/-</sup> MEFs after 8 h of TNF- $\alpha$  (25 ng/mL) + z-VAD-FMK (zVAD) (50  $\mu$ M) + cycloheximide (CHX) (5  $\mu$ g/mL) treatment.  
 (L) LDH assay (n = 3) showing cytotoxicity in WT and *Zbp1*<sup>-/-</sup> MEFs after 48 h of 500 nM Doxo treatment. Statistical significance was determined using ANOVA and Tukey (I) or Šídák (B, C, and E–G) post hoc test, or unpaired t test (K and L). \*p < 0.05, \*\*p < 0.01, and \*\*\*p < 0.001. Error bars represent SEM.



(legend on next page)

**Figure S5. IFN-I and Doxorubicin synergize to imbalance cardiomyocyte mitochondrial gene expression and disrupt contractility, related to Figure 5**

(A) qRT-PCR analysis of *Top1mt* and ISGs in WT and *Zbp1*<sup>-/-</sup> murine neonatal cardiomyocytes (CMs) transfected with siCtrl or si*Top1mt* for 96 h.

(B) Volcano plots of the gene set enrichment analysis (GSEA) showing the differentially regulated pathways in GSE40289 and GSE79413 datasets: CMs isolated from adult mouse hearts challenged with 25 mg/kg Doxo for 16 h vs. saline controls, and human-induced pluripotent stem cell-derived cardiomyocytes (hiPSC-CMs) treated with 1  $\mu$ M Doxo for 24 h vs. controls (NES, normalized enrichment score; FDR, false discovery rate).

(C) MFI quantification of Cyto. and Mito. Z-DNA in WT and *Zbp1*<sup>-/-</sup> murine neonatal CMs treated with or without Doxo (125 nM, 24 h). MFI percentiles are normalized to untreated WT or *Zbp1*<sup>-/-</sup> murine neonatal CMs.

(D–F) qRT-PCR analysis of ISGs (D), cardiac damage markers (E) and mitochondrial DNA- or nuclear DNA-encoded mitochondrial transcripts (F) in hiPSC-CMs treated with or without human recombinant IFN $\alpha$  (10 ng/mL) and IFN $\beta$  (10 ng/mL) for 96 h.

(G) qRT-PCR analysis of mitochondrial DNA-encoded mitochondrial transcripts in murine neonatal CMs treated with mouse IFN $\beta$  (1 ng/mL) or Doxo (500 nM) for 24 h.

(H) Camera-capture assay showing beat periodicity and images of hiPSC-CMs after indicated treatments (100 nM Doxo and/or 10 ng/mL of both human recombinant IFN $\alpha$  and IFN $\beta$ ) for 96 and 120 h. Yellow arrows indicate cardiomyocyte vacuolization. Statistical significance was determined using ANOVA and Tukey post hoc test (A and C), or unpaired t test (D–G). \*p < 0.05, \*\*p < 0.01, and \*\*\*p < 0.001. Error bars represent SEM.

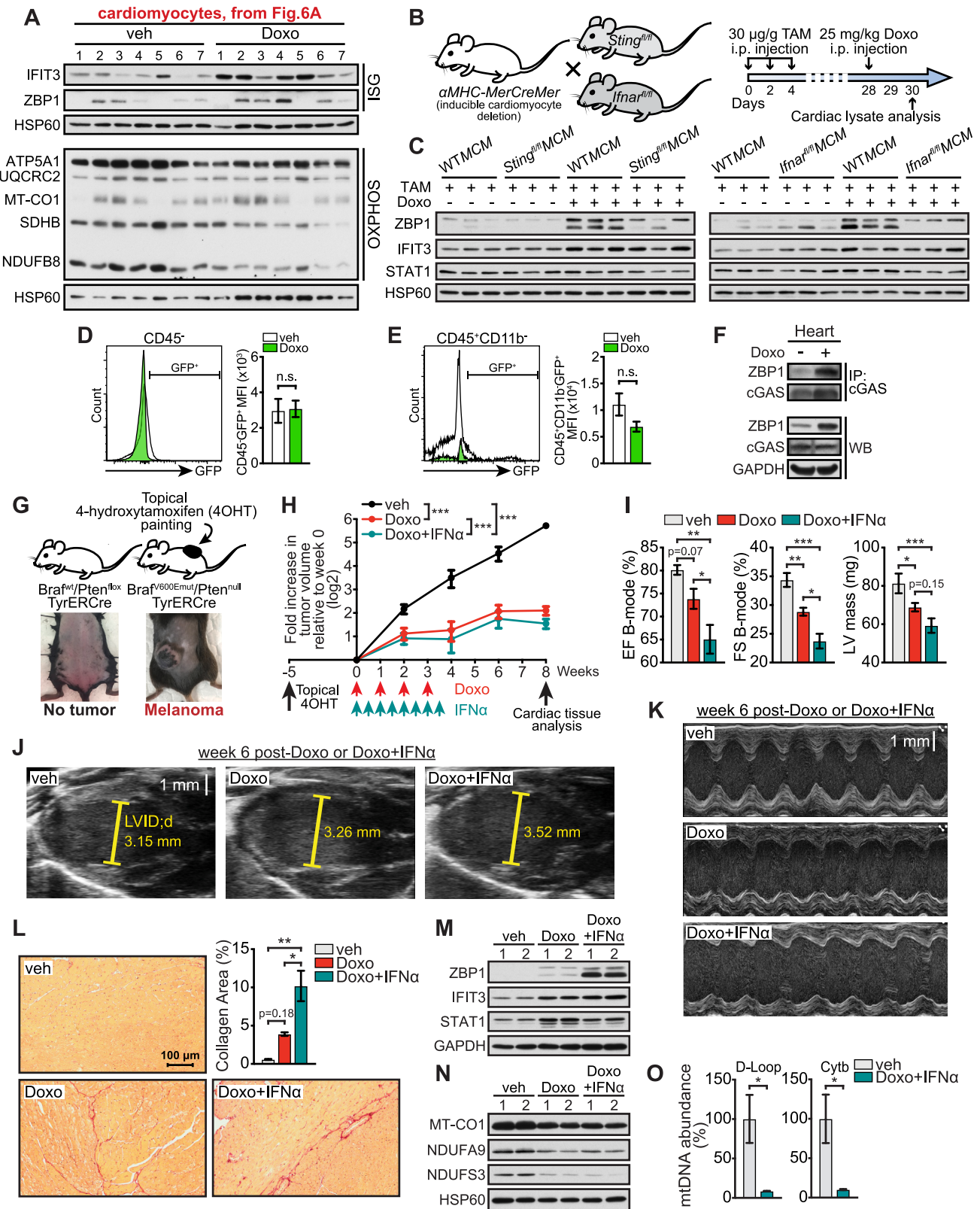


**Figure S6. Doxorubicin induces cardiomyocyte IFN-I signaling that potentiates cardiomyopathy in tumor-bearing mice, related to Figure 6**

- (A) Western blots of ISGs and OXPHOS components in CMs isolated from veh and Doxo-challenged hearts (n = 7 per challenge).
- (B) Generation of tamoxifen (TAM)-inducible cardiomyocyte-specific STING and IFNAR knockout mouse strains (left) and Doxo administration regimen (right).
- (C) Western blots in cardiac lysates from WT $MCM$ ,  $Sting^{fl/fl}MCM$ , and  $Ifnar^{fl/fl}MCM$  mice induced with TAM and then challenged with veh or Doxo (n = 3 per genotype per challenge).
- (D and E) Flow cytometric analysis of GFP<sup>+</sup> population in CD45<sup>-</sup> (D) or CD45<sup>+</sup>CD11b<sup>-</sup> (E) cells isolated from veh and Doxo-challenged mouse hearts. Histograms are representative of 4 independent experiments. MFI quantifications are shown on the right.
- (F) CoIP showing interactions between ZBP1 and cGAS in cardiac extracts from veh and Doxo-challenged mice. Mice were i.p. injected with 25 mg/kg Doxo for 24 h.
- (G) Schematic illustration of melanoma induction.
- (H) Primary melanoma volume of each treated group measured every other week starting from 5 weeks post 4-hydroxytamoxifen (4OHT) induction.
- (I) Left ventricular ejection fraction (EF), fractional shortening (FS) and mass at week 4 were calculated from parasternal long axis B-mode (n = 5 per group).
- (J and K) Representative parasternal long axis (J) and short axis (K) images from each treatment at week 6 post veh, Doxo, or Doxo + IFN $\alpha$  challenge.
- (L) Representative picrosirius red staining images of heart sections from veh-, Doxo-, and Doxo + IFN $\alpha$  treat melanoma mice. Collagen area of each group are quantified and shown at up-right corner.
- (M) Western blots in cardiac extracts from veh, Doxo, and Doxo + IFN $\alpha$  challenged tumor-bearing mice at week 8.
- (N and O) Western blots (n = 2) (N) and qPCR analysis (n = 3) (O) in cardiac extracts from veh, Doxo, and Doxo + IFN $\alpha$  challenged tumor-bearing mice at week 8. Statistical significance was determined using unpaired t test (D, E, and O), or ANOVA and Tukey post hoc test (H, I, and L). \*p < 0.05, \*\*p < 0.01, and \*\*\*p < 0.001. Error bars represent SEM.

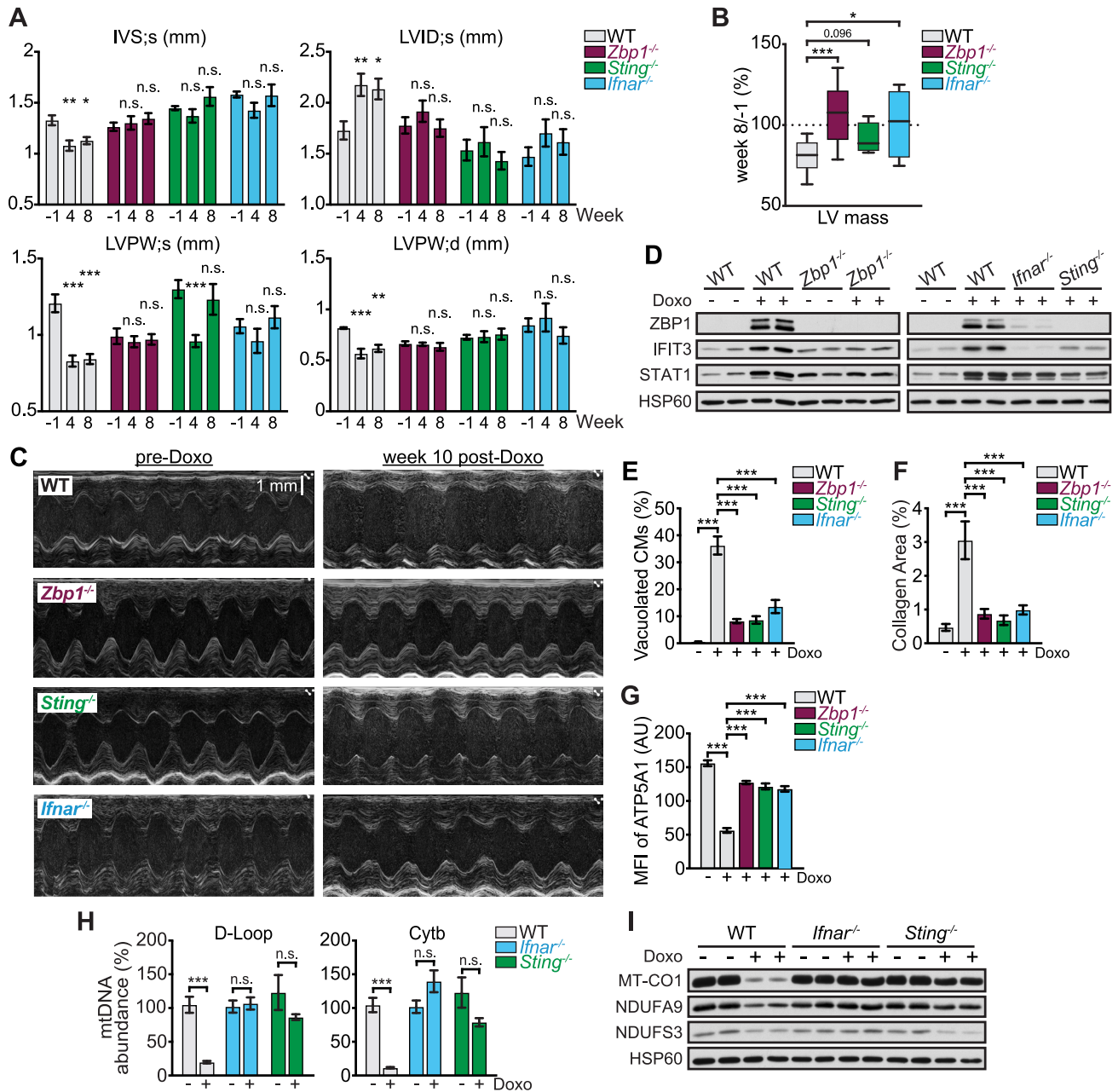


**Figure S7. Doxorubicin-induced ISG expression and cardiac dysfunction are lessened in the absence of ZBP1-STING-IFNAR signaling, related to Figure 7**

- (A) Left ventricle wall thickness and internal diameter measurements were made pre-Doxo (week -1) and at weeks 4 and 8 weeks post challenge in short axis M-mode ( $n = 12$  of WT and *Zbp1*<sup>-/-</sup> groups,  $n = 6$  of *Ifnar*<sup>-/-</sup> and *Sting*<sup>-/-</sup> groups).
- (B) Heart weight changes in WT, *Zbp1*<sup>-/-</sup>, *Sting*<sup>-/-</sup>, and *Ifnar*<sup>-/-</sup> mice at week 8 compared to pre-Doxo treatment (week -1) ( $n = 12$  of WT and *Zbp1*<sup>-/-</sup> groups,  $n = 6$  of *Ifnar*<sup>-/-</sup> and *Sting*<sup>-/-</sup> groups).
- (C) Representative short axis images from each genotype pre- and 10 weeks post-Doxo treatment.
- (D) Western blots ( $n = 2$  per genotype per treatment) in cardiac lysates 10 weeks post Doxo challenge.
- (E) Percentages of CMs exhibiting vacuolization in WT, *Zbp1*<sup>-/-</sup>, *Sting*<sup>-/-</sup>, and *Ifnar*<sup>-/-</sup> heart sections with or without Doxo challenge ( $n = 12$  fields per group).
- (F) Percentages of picrosirius red positive area (collagen area) in WT, *Zbp1*<sup>-/-</sup>, *Sting*<sup>-/-</sup>, and *Ifnar*<sup>-/-</sup> heart sections from mice with or without Doxo challenge ( $n = 9$  fields per group).
- (G) Quantification of ATP5A1 fluorescent intensity in WT, *Zbp1*<sup>-/-</sup>, *Sting*<sup>-/-</sup>, and *Ifnar*<sup>-/-</sup> heart sections with or without Doxo challenge ( $n = 10$  fields per group).
- (H) qPCR analysis ( $n = 3$  per genotype per treatment) in cardiac lysates from veh- and Doxo-treated WT, *Ifnar*<sup>-/-</sup>, and *Sting*<sup>-/-</sup> mice.
- (I) Western blots ( $n = 2$  per genotype per treatment) in cardiac lysates from veh- and Doxo-treated WT, *Ifnar*<sup>-/-</sup>, and *Sting*<sup>-/-</sup> mice. Statistical significance was determined using ANOVA and Tukey post hoc test (A and E-H), or unpaired t test (B). \* $p < 0.05$ , \*\* $p < 0.01$ , and \*\*\* $p < 0.001$ . Error bars represent SEM.